Dissertation zur Erlangung des Doktorgrades
der Fakultät für Chemie und Pharmazie
der Ludwig-Maximilians-Universität München

Early locus coeruleus system degeneration drives olfactory dysfunction in Alzheimer's disease

Carolin Meyer (geb. Klaus)
aus
Dortmund, Deutschland

2024

Erklärung

Diese Dissertation wurde im Sinne von § 7 der Promotionsordnung vom 28. November 2011 von Prof. Dr. Jochen Herms betreut und von Herrn Prof. Dr. Martin Biel von der Fakultät für Chemie und Pharmazie vertreten.

Eidesstattliche Versicherung

Diese Dissertation wurde eigenständig und ohne unerlaubte Hilfe erarbeitet. Teile der enthaltenen Abbildungen in dieser Dissertation wurden in dem folgenden Manuskript veröffentlicht.

Meyer, C., Niedermeier, T., Feyen, P., et al. Noradrenergic axon loss drives olfactory dysfunction in Alzheimer's disease, 02 October 2024, Preprint (Version 1) available at Research Square [https://doi.org/10.21203/rs.3.rs-4887136/v1]

München, 09.12.2024

Carolin Meyer (geb. Klaus)

Dissertation eingereicht am 09.12.2024
Erstgutachter: Prof. Dr. Martin Biel
Zweitgutachter: Prof. Dr. Jochen Herms
Mündlich Prüfung am 17.02.2025

Early locus coeruleus system degeneration drives olfactory dysfunction in Alzheimer's disease

Abstract

The locus coeruleus (LC), a small but vital brain region, has gained great attention for its early involvement and vulnerability in Alzheimer's disease (AD). The LC is the primary source of noradrenaline in the forebrain and plays a crucial role in a variety of biological processes. AD is characterized by cognitive decline, memory loss, and behavioral changes, affecting millions of individuals worldwide. Pathological hallmarks of the disease are beta-amyloid plaques and neurofibrillary tangles. In AD, the LC is among the brain regions earliest affected and this vulnerability at this disease stage suggests a potential role in the disease pathogenesis. Moreover, AD is often accompanied by olfactory dysfunction, with patients experiencing difficulties with their sense of smell. Olfaction plays a critical role in everyday life, influencing food preferences, social interactions, and detecting hazards. Olfactory dysfunction observed in AD patients often predates the onset of cognitive symptoms by several years, providing an intriguing avenue for early detection and intervention. So far, changes in olfactory function are thought to be linked to the accumulation of beta-amyloid and/or hyperphosphorylated Tau in the olfactory bulb. Understanding the mechanisms underlying olfactory dysfunction in AD could provide valuable insights into the disease progression and potentially serve as a diagnostic tool.

In this study, we aimed to elucidate the role of the LC in the context of olfaction in AD. By utilizing a combination of animal models, post-mortem brain tissue analysis, and advanced imaging techniques, we seeked to explore the cellular mechanisms underlying the LC vulnerability and its impact on the olfactory system.

Our data revealed an age-dependent loss of LC-noradrenergic axons in the olfactory bulb (OB) of $APP^{NL\text{-}G\text{-}F}$ mice, already starting at 2 months of age. Notably, at 3 months of age, the axon loss was exclusively observed in the OB and independent of extracellular Aβ plaques. The loss of LC axons coincides with olfactory dysfunction, as demonstrated by an impaired performance in a buried food test and a sensitivity test. We pinpointed a reduction in noradrenaline release to be responsible for the olfactory impairment. In order

to verify that our findings are LC specific, we designed a LC expressing virus and were able to recapitulate our results in healthy animals. Furthermore, electrophysiological recordings of LC neurons in 6-month-old $APP^{NL\text{-}G\text{-}F}$ mice revealed LC neurons to be hyperactive. Notably, the integrity of mitral cells, the first odor projection neurons of the OB remained intact. Asking for the underlying mechanism of LC axon loss we identified intraneuronal Aβ in LC somata, upregulated microglia activity and engulfment of compromised LC axons by microglia. Hyperactive LC neurons trigger the externalization of the 'eat-me' signal phosphatidylserin which is recognized by MFG-E8. Together they initiate microglia clearance of these tagged LC axons. Modulating microglia function by a TSPO knockout abolished the LC axon loss in the OB and prevented olfactory dysfunction.

Importantly, we could also translate our findings to humans. We demonstrated strong LC axon degeneration in post-mortem OB tissue from prodromal AD patients. TSPO-PET scans revealed an early OB specific increase in microglia activity/number and AD patients experienced a reduction in their sense of smell.

In summary, our study highlights the early-onset loss of LC-noradrenergic axons in the OB to underlie olfactory dysfunction in an Aβ-pathology mouse model and in AD patients. This data sheds light on the early pathological changes in the LC and offers insights into the mechanisms underlying olfactory deficits in AD. A diagnosis years before first cognitive symptoms appear might provide a potential for therapeutic strategies aiming at slowing or halting the disease progression.

Zusammenfassung

Der Locus coeruleus (LC) ist eine kleine, aber lebenswichtige Hirnregion, die wegen seiner frühen Beteiligung und Verletzlichkeit bei der Alzheimer-Krankheit in den letzten Jahrzehnten große Aufmerksamkeit erlangt hat. Der LC ist die Hauptquelle für den Botenstoff Noradrenalin im Vorderhirn und spielt eine entscheidende Rolle bei einer Vielzahl biologischer Prozesse. Die Alzheimer-Krankheit zeichnet sich durch kognitiven Verfall, Gedächtnisverlust und Verhaltensänderungen aus und betrifft weltweit Millionen von Menschen. Pathologische Merkmale der Krankheit sind Beta-Amyloid-Ablagerungen und neurofibrilläre Bündel. Der LC ist eine der am frühesten betroffenen Hirnregionen und diese Anfälligkeit im frühen Krankheitsstadium deutet auf eine mögliche Rolle beim Fortschreiten der Krankheit hin. Darüber hinaus geht die Alzheimer-Krankheit häufig mit einer Störung des Geruchssinns einher. Der Geruchssinn spielt im täglichen Leben eine entscheidende Rolle, da er den Geschmacksinn beeinflusst, soziale Interaktionen steuert und dabei hilt Gefahren zu erkennen. Riechstörungen bei Alzheimer-Patienten treten oft mehrere Jahre vor anderen kognitiven Symptomen auf und können daher einen wichtigen Anhaltspunkt zur Früherkennung und Intervention bieten. Bisher ging man davon aus, dass Veränderungen der Riechfunktion mit der Ablagerung von Beta-Amyloid und/oder Tau im Riechkolben (Bulbus olfactorius) zusammenhängen, jedoch wurde noch keine direkte Verbindung gefunden. Die weitere Erforschung der Ursache von Riechstörungen bei der Alzheimer-Krankheit könnte daher wertvolle Einblicke in den Krankheitsverlauf liefern und möglicherweise zur diagnostisches Früherkennung beitragen.

In der vorliegenden Studie wurde die Rolle des LCs im Zusammenhang mit dem Geruchssinn bei der Alzheimer-Krankheit untersucht. Mit einer Kombination von Tiermodellen, postmortalen Hirngewebeanalysen und bildgebenden Verfahren haben wir versucht, die zellulären Mechanismen zu verstehen, die der Verletzlichkeit des LC und seinen Auswirkungen auf das olfaktorische System zugrunde liegen.

Unsere Daten zeigen einen altersabhängigen Verlust von LC-noradrenergen Axonen im Bulbus olfactorius von $APP^{NL\text{-}G\text{-}F}$ Mäusen, der bereits im Alter von zwei Monaten einsetzt. Bemerkenswert ist, dass der Axonverlust im Alter von drei Monaten ausschließlich im Bulbus olfactorius und unabhängig von extrazellulären Aβ-Plaques beobachtet wurde.

Der Verfall der LC Axone geht mit einer olfaktorischen Dysfunktion einher, die sich in einer verminderten Leistung beim Futtersuchtest und Sensitivitätstest zeigt. Als Ursache für das Geruchsdefizit konnten wir eine verminderte Noradrenalinausschüttung im Bulbus olfactorius identifizieren. Um zu überprüfen, ob unsere Ergebnisse LC spezifisch sind, wurde ein spezieller Virus entwickelt, der bei gesunden Tieren zu einer Degeneration der LC Axone führt und Geruchsprobelme hervorruft. Wir konnten unsere Ergebnisse also tätsächlich reproduzieren und den LC als die Startregion identifizieren. Elektrophysiologische Messungen von LC-Neuronen in sechs Monate alten $APP^{NL\text{-}G\text{-}F}$ Mäusen zeigten, dass die LC Neurone hyperaktiv sind. Interessanterweise ist die Aktivität der Mitralzellen, der ersten Projektionsneuronen im Bulbus olfactorius, unverändert. Auf der Suche nach der Funktionsweise des Verfalls von LC Axonen konnten wir intraneuronales Aβ in den LC Somata, eine erhöhte Mikroglia Aktivität und folglich die Phagozytose der LC-Axone identifizieren. Hyperaktive LC Neurone lösen die Externalisierung des 'Ess-mich' Signals Phosphatidylserin aus, an welches sich das Mikroglia Adaptorprotein MFG-E8 heftet und zusammen leiten sie die Mikroglia Phagozytose der LC Axone ein. Die Modulation der Mikrogliafunktion durch einen TSPO-Knockout konnte den Verlust der LC Axone im Bulbus olfactorius aufheben und den Rückgang der Riechleistung aufhalten.

Ein wichtiger Schritt ist, dass wir unsere Ergebnisse auch auf den Menschen übertragen konnten. In postmortalem Riechkolben-Gewebe von Patienten im Frühstadium der Alzheimer-Krankheit konnten wir einen starken Rückgang der LC Axone nachweisen. Zudem zeigten TSPO-PET-Scans eine frühe Zunahme der Mikroglia Aktivität im Bulbus olfactorius und bei Alzheimer Patienten wurde eine Verminderung der Riechleistung gefunden.

Zusammenfassend zeigt unsere Arbeit, dass ein wichtiger Zusammenhang zwischen dem frühen Verlust von LC-noradrenergen Axonen im Riechkolben und Geruchsstörungen bei Mäusen und Alzheimer Patienten besteht. Es wurde die Funktionsweise für den Zerfall der LC Axone gefunden, der schlussendlich zu Geruchsbeeinträchtigungen führt. Der Geruchsinn und die Reduktion des Noradrenaline Levels kann als Biomarker zur Früherkennung der neurodegenerativen Krankheit Alzheimer dienen. Eine Diagnose Jahre bevor erste kognitive Symptome auftreten kann neue therapeutische Möglichkeiten eröffnen, um das Fortschreiten der Krankheit zu verlangsamen oder sogar zu stoppen.

Contents

1 Introduction

Olfaction, or the sense of smell, is one of the five human senses. It has many functions including influencing our taste, creating memories, searching for a partner and also importantly it helps detecting hazards. Many factors can interfere with normal olfaction causing hyposmia, a reduction in smell or even anosmia, the loss of smell. In several neurodegenerative diseases, predominantly in Alzheimer's and Parkinson's disease, olfactory dysfunction was found to be the first preclinical symptom, occurring already several years before other cognitive impairments. Intensive research was invested in studying the underlying mechanism of its dysfunction, however, only hypothesis have emerged so far. The most commonly respected view in Alzheimer's disease is that the olfactory bulb, which is in direct contact to the outside environment, displays early accumulation of toxic protein aggregates that spread in a prion-like manner. Moreover, the olfactory bulb and connected brain regions such as the enthorinal cortex and piriform cortex suffer from neuron and volume decline. However, whether the toxic proteins find their way through the nose or get transmitted from the locus coeruleus, another brain region effected early on in the disease, remains a conundrum.
Collectively, olfactory dysfunction serves as an early biomarker for Alzheimer's disease, but its molecular drivers remain to be further elucidated.

1.1 Alzheimer's disease

Alzheimer's disease (AD) is a progressive neurodegenerative disorder and the most common form of dementia. It predominantly affects the elderly population, with the number of people suffering from it increasing every year because of population growth and aging. AD is characterized by a gradual decline in memory function, cognition, and changes in behavior, ultimately resulting in severe disability. The underlying mechanism involves the accumulation of abnormal protein deposits, amyloid-beta and Tau, leading to neuronal damage and cell death [2]. To date, no cure exists, however, early detection and various therapeutic approaches aim to slow down the disease progression and ease symptoms.

1.1.1 Disease discovery, symptoms, underlying mechanisms and therapies

Alzheimer's disease was first identified by Dr. Alois Alzheimer in 1906. The Bavarian pathologist examined the brain tissue of Auguste D., a 56-year-old woman who had experienced memory loss, disorientation, sleep disturbances and aggression. Postmortem histology revealed a shrinkage of the cerebral cortex and abnormal protein deposits, known as amyloid plaques and neurofibrillary tangles. Today, these hallmarks have become integral to AD diagnosis [3]. Early signs of the disease typically include olfactory deficits and word finding problems. Disorientation and memory deficits follow only several years later, with individuals getting lost in familiar environments or losing track of time. Poor judgment, impaired decision-making, and problem-solving difficulties come on top. Behavioral changes, mood swings and increased anxiety become evident, affecting an individual's personality. At the late disease stage, motor function is impaired, including problems with basic tasks, like eating and swallowing, communicating, dressing and walking can occur.
The underlying mechanisms of AD involve several complex pathological processes and so far no distinct mechanism could be pinpointed. One prominent theory for the development of AD is the amyloid cascade hypothesis, proposed in the early 1990s [2, 4, 5]. The process begins with the amyloid precursor protein (APP), a membrane protein found in the brain. In healthy individuals, APP undergoes enzymatic cleavage, resulting in harmless byproducts. However, in AD, post-translational processing of APP leads to the formation of Aβ peptides. The Aβ peptides, particularly Aβ 42, have a tendency to aggregate and clump together, forming insoluble plaques in the extracellular space. These amyloid plaques disrupt cellular function and communication between neurons, leading to impaired synaptic connections and neuronal damage. The accumulation of Aβ peptides triggers a series of events that lead to neurotoxicity and the hyperphosphorylation of Tau proteins inside neurons. Hyperphosphorylated Tau proteins then form neurofibrillary tangles, which further disrupt the neuron's structural integrity and contribute to cell death. As amyloid plaques and neurofibrillary tangles spread throughout the brain, the damage to neurons becomes detrimental. While the amyloid cascade hypothesis has been influential in guiding Alzheimer's disease research and drug development for many years, it has to be noted that other factors, such as inflammation, environmental factors and genetics,

play significant roles in the disease's pathogenesis, too [6].

Despite extensive research, there is currently no cure for Alzheimer's disease. All available therapies can only help to manage symptoms and slow the disease's progression. The review article by Zhang and colleagues in 2023 summarises the anti-Aβ therapies approved for AD to date [7]. There are three drugs (Donepezil, Rivastigmine, and Galantamine) that belong to the family of cholinesterase inhibitors and work by decreasing the breakdown of the neurotransmitter acetylcholine. In 2021 and 2023 the first antibody-based drugs have been approved that are developed to reduce Aβ. In patients with early AD, the drugs Aducanumab and Lecanemab reduce the Aβ-plaque load and thereby slow cognitive decline [8]. Lecanemab is Food and Drug Administration approved in the Unites States, China, Japan, South Korea, Hong Kong and Israel. In Europe it was first declined due to two side effects: oedema and haemorrhage [9], but was re-examined in a restricted patient group (ApoE4 non-carrier or heterozygous carrier) in November 2024 with the conclusion that the benefits outweight the risks. Therefore, lecanemab will also be available in Europe under strict regulations and regular screenings of patients receiving the compound [10].

1.1.2 APP processing into extracellular and intracellular Aβ

Amyloid-beta is the main building brick of Aβ-plaques. It is derived from the amyloid precursor protein APP and can exist in two forms, extracellular and intracellular Aβ. APP is a type 1 transmembrane spanning protein that consists of 695-770 amino acids and protrudes its amino terminus into the extracellular space and the carboxyl terminus into the cells cytosol. APP itself is not harmful and present in every cell. Upon cleavage however it can get pathogenic [11]. The majority of APP is processed through the non-amyloidogenic pathway in which the α-secretase (ADAM family) cleaves it into a large ectodomain, called sAPPα that will be released extracellularly and a small carboxy-terminal fragment (C83) that resides in the membrane before being further cleaved by the γ-secretase into the APP-intracellular domain (AICD). Since the α-secretase cleaves APP within the Aβ domain it prevents the generation and release of the Aβ peptide.

On the other hand, the amyloidogenic pathway promotes toxic Aβ production. Here, APP gets cleaved by the β-secretase (BACE1) which releases the extracellular ectodomain sAPPβ. Left in the membrane is the C-terminal fragment of APP (C99 or CTFβ). This

CTFβ gets further cleaved by the γ-secretase (presenilin 1 or 2, nicastrin, anterior pharynx defective and presenilin enhancer 2) resulting in the detachment of the AICD and also in the extracellular released Aβ protein (Fig. 1) [12, 13].
The APP$^{\text{NL-G-F}}$ mouse line used in this study promotes the processing of APP through the amyloidogenic pathway as the Swedish mutation changes the amino acids around the β-secretase, promoting BACE1 to bind to and cleave APP, while the Iberian mutation changes an amino acid after the γ-secretase and thereby increases its cleavage [14].
Extracellular Aβ consists of two variants, Aβ40 and Aβ42. Aβ40 makes up the majority of Aβ and is harmless, even stated to be neuroprotective. Aβ42 contrarily is harmful and can accumulate into Aβ plaques. It exists as fibrillar Aβ as well as oligomeric Aβ and depending on its accumulation forms either cored-plaques or diffuse plaques [15].
Next to extracellular Aβ playing an important role in the AD pathenogenesis, the existence and impact of intraneuronal Aβ is rather new and somewhat controversal [16]. Some studies postulate that intraneuronal Aβ might even accumulate earlier than extracellular Aβ, suggesting it as the earliest event or even the underlying cause of several neurodegenerative diseases [17–20].

1.1.3 Phatological role of intracellular Aβ

Intraneuronal Aβ can either be produced intracellularly through the amyloidogenic pathway or it can be internalized from the extracellular space [22]. In AD post-mortem tissue, intracellular Aβ was found in LC neurons, one of the first cell types in AD to degenerate [23]. Moreover, in several AD mouse lines intracellular Aβ accumulates in neurons before extracellular Aβ builds up [17–20, 24–26]. It was shown to bind to the α7 nicotinic acetylcholine receptor (α7nAChR) which transports it into the cell cytosol [27]. Notably, this α7nAChR receptor is mainly expressed in the locus coeruleus and dorsal raphe nucleus, two regions early affected in AD.
Looking at the localisation and function of intraneuronal Aβ, several studies have shown that it is mainly expressed in two cell organelles. Firstly, it was found in multivesicular bodies (MVBs), late endosomal organelles. Accumulation of intracellular Aβ disrupted MVBs by the inhibition of the ubiquitin-proteasome system which finally results in the

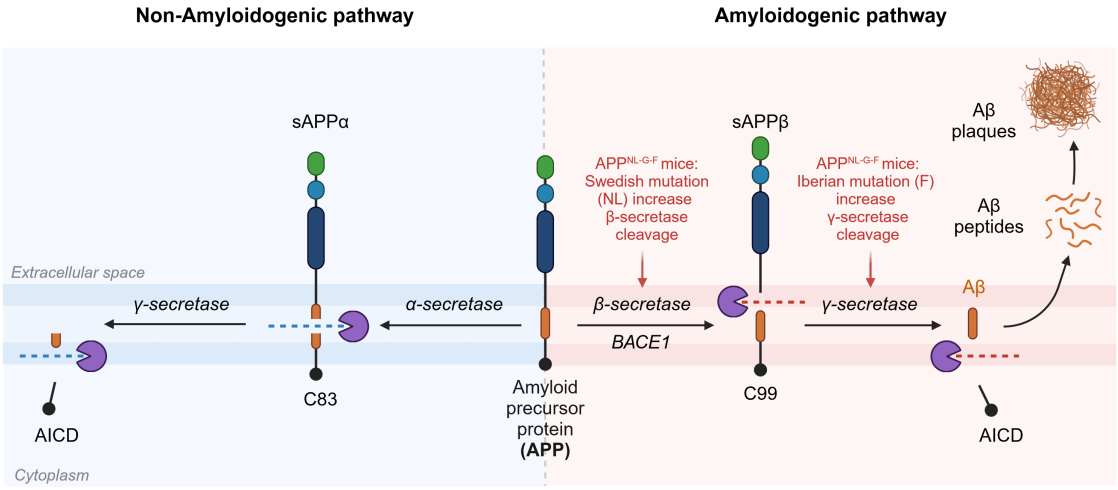

Figure 1: APP processing pathways

The amyloid-precursor-protein (APP) can undergo two processing pathways. In the non-amyloidogenic pathway, APP is cleaved twice resulting in a harmless, even protective extra- and intracellular product. In the amyloidogenic pathway on the other hand, APP gets cleaved by other enzymes at different amino acids, generating a toxic extracellular Aβ peptide and a toxic intracellular APP product called C99/AICD. In the APP$^{\text{NL-G-F}}$ mouse line, the Swedish and Iberian mutation increase the cleavage via the β-secretase and γ-secretase, respectively, promoting the amyloidogenic processing of APP (Graphic was created using a BioRender template and modified after Zhao et al., 2020 [21]).

buildup of the Tau protein [28–30]. Secondly, it was found in mitochondria, the cells powerhouse. Here, it causes mitochondrial deficits by decreasing the enzymatic activity of respiratory chain complexes III and IV and the rate of oxygen consumption, leading to the production of reactive oxygen species (ROS) [31–33].

The accumulation of intracellular Aβ in neurons was shown to cause neuron loss [34, 35], correlate to spatial learning dysfunction and cognitive impairment, enhances fear behavior [36–38] and disrupts fast axonal transport [39]. Despite the numerous publications, the existence of intraneuronal Aβ is controversially discussed [40]. This evolves mainly from technical difficulties to visualize intracellular Aβ as several antibodies against the C-terminus of the APP protein exist but their possible crossreactivity to the full-length APP protein renders their specificity.

1.1.4 Role of Tau

Next to Aβ plaques, neurofibrillary tangles (NFT) represent a hallmark of AD. Neurofibrillarly tangles are composed of hyperphosphorylated aggregates of the microtubule associated protein Tau. Under physiological conditions, Tau is present in neurons in its soluble form. It interacts with tubulin to promote its assembly into microtubules and thereby stabilizes them [41]. Under pathogenic conditions, Tau gets modified post-translational. Phosphorylation in general is a normal modification, but excessive phosphorylation can lead to hyperphosphorlated Tau, which can further aggregate into oligomeres and in the end stage to neurofibrillary tangles, resulting in the damage of the microtubule skeleton and finally in the collapse of the axonal transport [42, 43]. In AD, toxic Tau or NFT first build up in the brain stem and olfactory bulb and then get transported towards the transentorhinal regions, the limbic system and at later stages to the hippocampus and neocortex [44–47].

1.1.5 Microglia and their function

About 10 % of the mouse brain cells are microglia, varying between the different brain region and having the unique ability of self proliferation [48]. Microglia are the brains immune cells and therefore responsible for the surveillance of the environment. During physiological conditions, microglia maintain neuronal plasticity by synaptic pruning, phagocytosing debris and applying trophic support to neurons. In this so-called resting state, they have a ramified morphology with a small soma and long processes. During pathological insults, microglia become activated, or reactive, retracting their processes and having a round (amoeboid) cell body [49]. They migrate to the side of injury scavenging damaged neurons and toxic protein aggregates, such as Aβ. During the early stage of AD, when the first Aβ plaques form, microglia readily remove soluble Aβ oligomers and party fibrillar Aβ, highlighting the beneficial role of those cells. At later stages, however, microglia phagocytosis was shown to be impaired and thus clearance of Aβ was compromised, attributing those microglia a detrimental role [50, 51]. Immunohistochemically microglia can be visualized with the marker Iba1. For the detection of microglia inflammation, the 18kD translacator protein (TSPO) is frequently used [52]. TSPO is a protein

located in the outer membrane of mitochondria mainly inside microglia. It carries out different functions including cholesterol transport and fueling phagocytosis [53].

1.1.6 Microglial phagocytosis: How microglia sense dying neurons, injury and inflammation ('find-me' and 'eat-me' signals)

Microglia are the first responder cells to injury, inflammation and pathogenic threats. Through a complex signaling cascade of 'find-me' and 'eat-me' signals they get attracted towards the side of injury to execute their job as immune cells in order to keep their microenvironment clean and healthy. To do so, they undergo morphological and genomic transformations. Compromised neurons send out 'find-me' signals as for example the chemoattractant chemokine fractaline, high-mobility-group-protein B1 or adenosine triphosphate (ATP). Once microglia have sensed these signals and migrated towards it, the compromised neurons express 'eat-me' signals to stimulate microglial phagocytosis. The main 'eat-me' signals are phosphatidylserine (PS), and desialylated proteins/lipids including complement component 1q and 3b (C1q, C3b) and calreticulin (CALR). Microglia express the respective receptors (PS, Toll-like, scavenger and TREM2) to bind to these ligands. The binding can either be direct or coupled to an extracellular adaptor protein, such as milk fat globule-epidermal growth factor 8 (MFG-E8), growth-arrest-specific gene-6 (Gas 6), apolipoprotein E (ApoE) or galactin 3 (Gal3) [54–56]. Figure 2 shows the most common signaling pathways between a compromised neuron and an attracted microglia.

In the olfactory bulb, synaptic pruning of adult-born neurons by microglia is mediated via PS [57]. In healthy neurons, PS is localized to the inner cellular membrane. Upon different stimulants, mainly an excessive calcium influx into the neuron it gets flipped to the outer cellular membrane. Caspase- and calcium-induced inactivation of flippase and the activation of scramblases initiate this externalization. Once PS is exposed it can get recognized directly by different microglia receptors or indirectly via MFG-E8 which in turn binds to microglial vitronectin receptors, the $\alpha v\beta 3/5$ integrins [58].

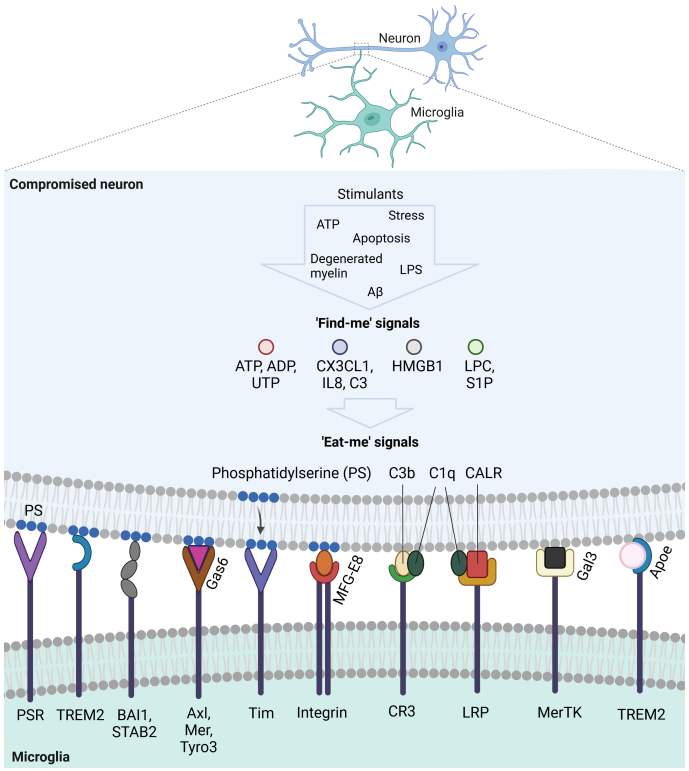

Figure 2: Signaling pathways for the initiation of microglial phagocytosis of compromised neurons

Scheme visualizing 'find-me' and 'eat-me' signals expressed by compromised neurons and the respective receptors on microglia. Different stimulants can damage neurons, inducing them to release signals to attract microglia and initiate phagocytosis. Microglia express various receptors that can connect to specific ligands on the extracellular membrane of the neuron (Graphic was created on BioRender and modified after Brown and Neher, 2014 [59]).

1.2 Locus coeruleus

The locus coeruleus (LC) is the main nucleus of the noradrenergic system, providing the primary source of noradrenaline (NA) in the forebrain. Its name derives from the latin term "blue spot", which refers to its blue appearance resulting from the presence of neuromalanin in these neurons. It was first discovered at the beginning of the 19th century from several researchers seeing a dark stripe of cells in the brains of autopsy cases [60–62]. The LC's neuronal projections are extensive, innervating almost the entire CNS. This wide network associates the LC with the control of a variety of different functions,

including arousal, sleep/wake states, memory, learning and olfaction [63]. On the other hand, it is this broad range of functions and extensive projections that makes the LC particular vulnerable to neurodegenerative diseases.

1.2.1 Anatomy and Connectivity

Anatomically, the LC is located in the rostral pons, adjacent to the fourth ventricle. In humans, it contains 20.000–50.000 pigmented neurons, while the rodent LC is comprised of about 3.000 neurons [64–67]. Despite differences in the number of neurons, the LC's functional significance remains highly conserved across species. The LC is composed of medium-size neurons with at least two different cell morphologies that are heterogeneously distributed. Fusiform cells are predominantly localized along the rostral-caudal axis, whereas multipolar cells are mainly found within the ventral LC [68–70].

The LC's most prominent feature lies in its extensive projections [71]. LC axons are, unlike other long-range axons, unmyelinated and therefore have a relatively slow conduction speed and high energy demand [72]. Despite this, the wide connectivity and release of noradrenaline allows for the widespread modulation of numerous cells in the entire brain. Retrograde tracer experiments and multiplexed analysis of projections by sequencing showed that the efferent projections follow a rough topographic organization, innervating anatomically and functionally distinct areas from a discrete set of LC neurons [66, 73]. The main efferent projection destinations are the olfactory bulb, frontal cortex, midbrain, cerebellum and spinal cord (Fig. 3a) [60]. Kebschull (2016, p.7) discovered that: "Projections to the olfactory bulb appeared independent of projections to cortex, with some neurons projecting exclusively to the olfactory bulb (e.g. BC302), some projecting exclusively to cortex (e.g. BC79) and others projecting to both (e.g. BC108)" (Fig. 3c,d) [73]. On the other hand, the LC also receives input from various brain regions. Most afferent axons come from the midbrain and hypothalamus and to a lesser extend from the medulla, cerebellum, amygdala and pallidum, as illustrated in figure 3b [71, 74].

1.2.2 Function

Due to the LC's extensive axonal projections that release noradrenaline throughout the brain, it is implicated in a variety of different functions. Noradrenaline can modulate the

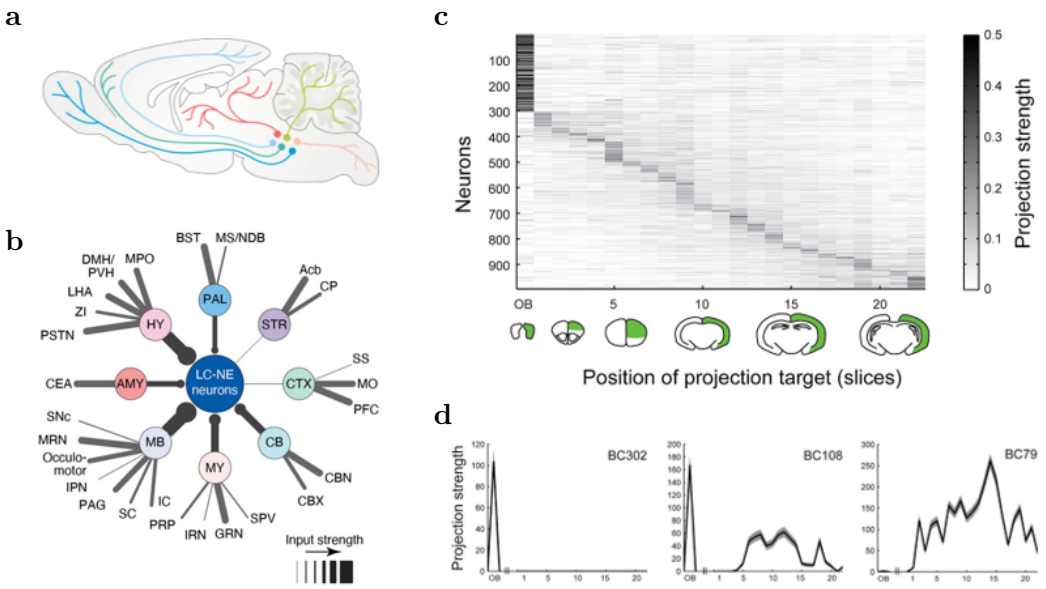

Figure 3: (a) Projection targets of the LC in a rodent brain [60]. **(b)** Input with respective strength from other brain regions to the LC [74]. (HY: Hypothalamus, AMY: Amygdala, MB: Midbrain, MY: Medulla, CB: Cerebellum, CTX: Cortex, SRT: Striatum, PAL: Pallidum) **(c)** Number of LC neurons that project to different brain regions. The olfactory bulb is most heavily innervated. **(d)** Diverse projection patterns showing one LC cell population (BC302) that exclusively projects to the olfactory bulb [73].

responses of single cells up to neuronal networks.

During sensory processing, noradrenaline modulates odor detection and discrimination thresholds in the olfactory bulb [75], enhances auditory perception [76, 77] and visual detection [78]. Studies investigating the function of the LC in the hippocampus reported that it mediates synaptic plasticity, spatial learning and fear [79–82]. Remarkably, axons innervating the dorsal hippocampus not only release noradrenaline but also the neurotransmitter dopamine [79, 83]. LC projections to the prefrontal cortex modulate attention and anxiety [84–86], while projections to the amygdala play a role in forming and retrieving emotional memories [84, 87]. In general, the level of arousal highly correlates to the LC's activity [74, 88–90]. High firing rates are associates with high levels of arousal and attention, while low firing rates are observed during sleep [91, 92].

1.2.3 Electrophysiological properties

Since the mid 20th century studies about the electrophysiological properties of LC neurons were conducted. In vivo, the LC has been shown to fire tonic or phasic, dependent on the state. During sleep the LC fires with <1 Hz and becomes silent during REM sleep. When waking up it fires tonic with <2 Hz and in active awake state it even fires with more than 2 Hz. During focused attention the LC spikes tonic with modest frequencies, while during task-related decision making it fires phasic [93–95]. In vitro, LC neurons are only tonically active. They display spontaneous firing, without external stimuli, making these neurons autonomous pacemaker cells. Typically, LC neurons fire with a frequency ranging from 1 Hz to 5 Hz. Autonomous pacemaking in neurons refers to the ability of neurons to generate rhythmic electrical activity in the absence of synaptic input or external stimuli. The precise mechanism underlying it in LC neurons is still not fully resolved. Several studies have shown that in vitro the spontaneous firing is intrinsically generated by Ca^{2+} conductances. Matschke et al., 2015 showed for example L-type calcium channels to play an important role in spontaneous action potential firing [96, 97].

Next to the spontaneous firing, LC neurons have two other characteristic properties, a delayed excitation (DE) and a slow afterhyperpolarization (AHP) [98]. Delayed excitation refers to a phenomenon where the firing of neurons occurs after a certain delay following the presentation of a hyperpolarizing stimulus. Transient potassium currents are though to mediate the delayed excitation [99], however, the precise mechanism remains unknown. Slow afterhyperpolarization describes the period after a burst of action potentials in which the membrane potential drops below the resting membrane potential of the cell. It is most likely mediated by the activation of calcium-activated potassium channels [98, 100].

Since morphological analysis have revealed a heterogenous LC population, it is not surprising that also electrophysiological differences between the cells have been observed. Based on the action potential shape of LC neurons, several studies identified at least two different subtypes that differ in amplitude, threshold and AHP. Type 1 neurons have wide APs, whereas type 2 neurons have narrow APs [70, 101, 102].

1.2.4 The neurotransmitter noradrenaline and its receptors

Noradrenaline is released by noradrenergic neurons, primarily originating from the LC in the brainstem. Compared to other neurotransmitters it is released via axon varicosities which are enlarged presynaptic boutons (Fig. 4) [103, 104]. NA is a catecholamine neurotransmitter and synthesized from the amino acid tyrosine. Tyrosine gets converted to L-Dopa by tyrosine-hydroxylase and is further processed by the DAPO-decarboxylase to dopamine. Dopamine is a direct precursor of noradrenaline, being converted by dopamine-β-hydroxylase [105]. Released noradrenaline binds to adrenergic-receptors that belong to the class of G-protein-coupled receptors. There are two main classes of noradrenergic receptors: α-adrenergic receptors (α1 and α2 subtypes) and β-adrenergic receptors (β1-β4 subtypes). Each subtype exhibits distinct functional properties and is responsible for specific cellular responses upon activation. Generally, α1 and β-receptors mediate an excitatory effect whereas α2 receptors mediate inhibition [63]. α1 receptors are preferentially found at postsynaptic sites while α2 and β receptors are present at post- and presynaptic sites [93]. Excessive NA in the synaptic cleft can be recycled back into the presynaptic neurons via the norepinephrine transporter, short NET (Fig. 4) [106].

1.2.5 Modulation of microglia by noradrenaline

Microglia can be modulated by various neurotransmitters and neuromodulators, including noradrenaline. They express α- and β-adrenergic receptors, making them accessible to noradrenaline. Several studies have shown that varying levels of NA have different modulatory effects on the microglia morphology and function [107–110]. In the awake state of mice, the LC is highly active, releasing a lot of noradrenaline. This noradrenaline mostly binds to β2-adrenergic receptors on microglia and reduces their aborization and decreases surveillance and response to injuries, by reducing contact points. In anesthetized mice or when NA release was inhibited one could observe an increase of microglia ramification and surveillance [109, 110]. Contrasting to this observation, Heneka et al., 2010 showed in an AD mouse model that reducing NA levels decreases microglial phagocytosis and recruitment to Aβ-plaques, even though their surveillance is increased [111].

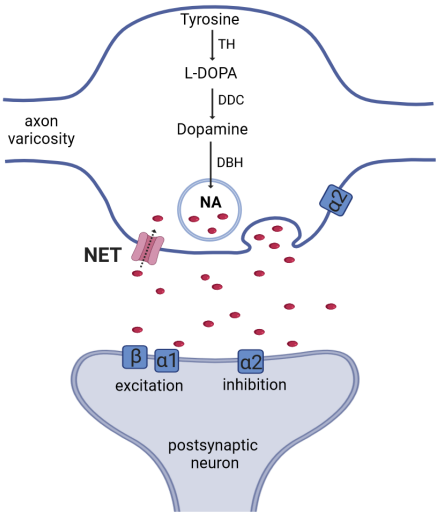

Figure 4: The synthesis of noradrenaline and its receptors

Scheme visualizing the synthesis and synaptic release of the neurotransmitter noradrenaline (NA). In the LC, tyrosine gets converted to L-Dopa by tyrosine-hydroxylase (TH) and is further processed by the DAPO-decarboxylase (DDC) to dopamine. Dopamine is a direct precursor of noradrenaline, being converted by dopamine-β-hydroxylase (DBH). In LC axons, noradrenaline is released via bulb transmission from axon varicosities. In the extracellular cleft, noradrenaline can either bind to other cells that express noradrenergic receptors or it can be recycled back into the axon via the norepinephrine transporter (NET) (Graphic was created on BioRender).

1.2.6 Dysfunction of LC in Alzheimer's disease

The LC has been postulated as one of the brain regions affected earliest in several neurodegenerative diseases, including Alzheimer's disease. Numerous studies have shown that the LC undergoes significant neuronal loss and shows toxic protein accumulation in the early stage of AD. This vulnerability to degeneration suggests a potential involvement in the pathogenesis of AD. The LC's primary role in the modulation of noradrenaline release is crucial for maintaining neuronal homeostasis and supporting synaptic plasticity. However, in AD, the LC experiences altered noradrenergic function, which may contribute to the disease progression.

In humans

Several studies have investigated the LC neuron demise in AD, either with the help of MRI on living patients or post-mortem via histological analysis. For both methods the data regarding LC neuron numbers and volume differs considerably, probably due to different scanners, the selection of patients, the amount of brain slices used and analysis methods. Nevertheless, all studies reported LC neuron loss and volume reduction in early and late stage AD patients compared to healthy controls [112–115]. Post-mortem, the LC neuron number was decreased varying between 46 % and 68 %, with one study showing a reduction of 30 % already for mild cognitive impaired patients (MCI) (Fig. 5a,b,e,f) [113]. Theofilas et al., 2017 correlated the LC volume reduction to the Braak stages. With an increasing Braak stage by 1, the LC shrinks by 8.4 % [116]. MRT scans in alive patients showed the intensity/contrast of the LC region to be significantly lower in AD patients than in healthy patients. The decline was more prominent in the rostral part of the LC than in the caudal part [114]. In addition to the prominent and early degeneration, the LC is also one of the regions that display early toxic protein aggregates. Histological stains and cerebral spinal fluid (CSF) samples revealed AD patients to exhibit hyperphosphorylated Tau and amyloid beta deposition in LC neurons and in the extracellular space (Fig. 5c,d,g,h) [23, 114, 117].
Collectively, the degree of LC system degeneration mostly matches the stage of dementia, highlighting its role in the disease pathogenesis.

In rodents

Rodent models investigating the role of LC dysfunction in AD found comparable results to the human studies as address in the previous paragraph. Both in Tau models, such as TauP301L mice [47], and Aβ models, like the APPPS1 mice [119], and TgF344-AD rats [120] a decline in LC neuron number, axonal density and a lower NA level was observed which was suggested to be mediated by Tau and/or Aβ accumulation. The reduction in axon density and NA release was further associated with different behavioral phenotypes, as for example object-memory impairment [121], spatial learning [122] or olfactory deficits [123].

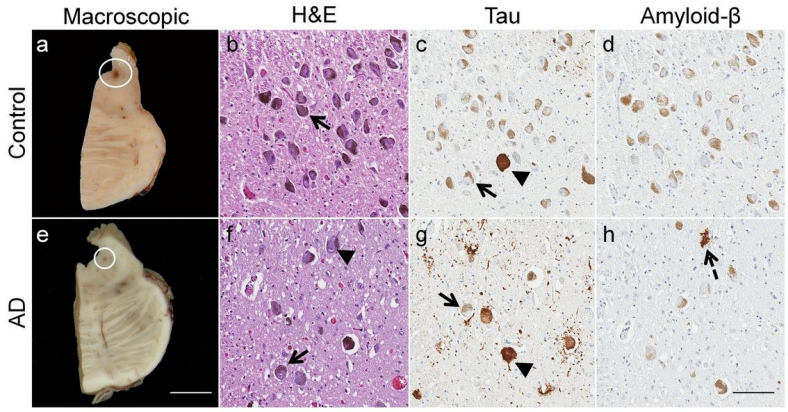

Figure 5: Degeneration and toxic protein aggregation in the locus coeruleus of an Alzheimer's disease patient

(a-b,e-f) Coronal section through the hindbrain of a healthy human brain and an AD brain that visualizes LC neuron decline. (c-d) Stains against Tau and Aβ show one Tau positive LC neuron but no Aβ in the healthy brain. (g-h) Remaining LC neurons in the AD brain are Tau positive and Aβ deposits can be found extracellularly (scale bar macroscopic: 8mm, microscopic: 100 µm), (Picture taken over from Matchett et al., 2021 [118]).

1.3 Olfactory system

Olfaction is a remarkable sensory system found across the animal kingdom which allows to perceive and interpret odors in the environment. It is often considered one of the oldest and most fundamental senses, as it plays a crucial role in survival, and social communication of all species [124].

The olfactory system is composed of the primary olfactory areas (olfactory epithelium and olfactory bulb) and the secondary olfactory area (olfactory cortex). Chemical odorant molecules enter the nose and reach the olfactory epithelium, an epithelial tissue at the roof of the nasal cavity. Each olfactory sensory neuron (OSN) located here expresses a single odorant receptor. OSNs that express the same receptors send the odor information to a specific glomeruli in the olfactory bulb (Fig. 6). At this step the chemical odorant will be converted into an electrical signal [125, 126]. A sophisticated network of neurons and neuronal circuits in the OB then shapes the signal before transmitting it to higher brain regions, where they are processed and integrated with other sensory inputs to form a comprehensive perception of the inhaled odorant [126].

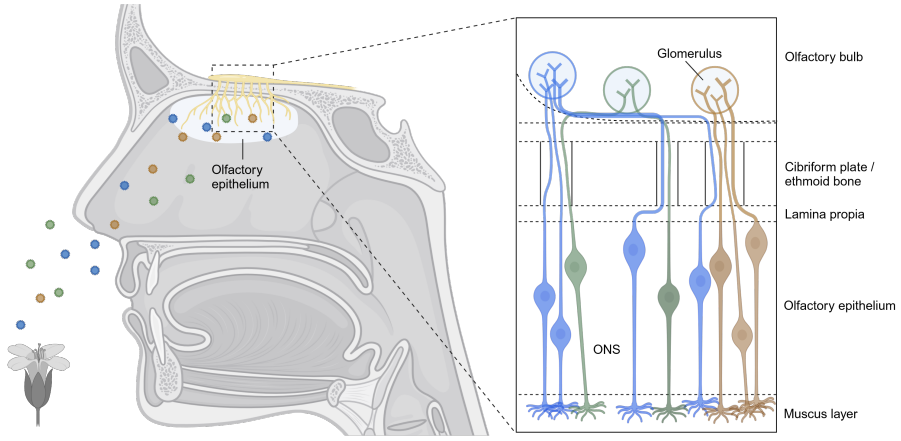

Figure 6: Human olfactory system

Scheme illustrating the structure of the human olfactory system. An inhaled odorant gets detected by the receptors of olfactory sensory neurons (OSN) in the olfactory epithelium. These OSNs transmit the signal to gomeruli in the olfactory bulb for higher-brain processing (Graphic was created on BioRender).

1.3.1 Olfactory bulb anatomy and neurons

The olfactory bulb is a crucial structure in the olfactory system where the initial processing of olfactory information takes place. It is composed of five layers and contains several cell types that play distinct roles in odor processing (Fig. 7) [127].

1. Olfactory nerve layer (ONL): The olfactory nerve layer is the most superficial layer of the olfactory bulb. It consists of bundles of axons from olfactory sensory neurons (OSNs) located in the olfactory epithelium of the nasal cavity. These axon bundles project directly into the olfactory bulb glomeruli where they synapse with neurons in the deeper layers.

2. Glomerular layer (GL): The glomerular layer is the first internal layer of the olfactory bulb and is named for its distinctive glomerular structures. Each glomerulus represents a functional unit where OSN axons form synapses with two main types of cells: mitral cells (MC) and tufted cells (T). These connections allow the olfactory bulb to encode and process information related to specific odorants. Additionally, the glomerular layer contains various dopaminergic interneurons, including periglomerular cells (PG), short axon cells and external tufted cells, which modulate the synaptic interactions within glomeruli.

3. External plexiform layer (EPL): The external plexiform layer is located beneath the glomerular layer and is characterized by its complex network of synaptic connections. Mitral and tufted cells, which receive input from OSNs in the glomeruli, project their dendrites into the EPL. In this layer, mitral and tufted cells receive excitatory input from OSNs via the lateral dendrites and send their axons to higher brain regions, such as the olfactory cortex. The EPL also contains dendrites of granule cells, which are inhibitory interneurons that play a crucial role in shaping the output of mitral and tufted cells.

4. Mitral cell layer (MCL): The mitral cell layer is named after the mitral cell bodies found within it. Mitral cells are the principal output neurons of the olfactory bulb. They receive input from OSNs via synapses in the glomeruli and dendritic branches in the external plexiform layer and process them to higher brain areas. Mitral cells can be further subdivided into two subpopulations based on their lateral dendrites terminating either in the outer or inner external plexiform layer.

5. Internal plexiform layer (IPL): The internal plexiform layer lies below the mitral cell layer and contains synaptic connections from granule cells, mitral cell lateral dendrites, and centrifugal fibers. Centrifugal fibers are axons from neurons in the olfactory cortex that project back to the olfactory bulb, providing a form of top-down modulation of olfactory processing.

6. Granule cell layer (GCL): The granule cell layer is the deepest layer of the olfactory bulb. It primarily contains granule cells (G), which are inhibitory interneurons that receive input from mitral and tufted cells in the external plexiform layer and provide feedback inhibition to the mitral and tufted cells in the glomerular layer.

1.3.2 Neuromodulatory role of noradrenaline, acetycholine, dopamine and serotonin in the olfactory bulb

There are four key neurotransmitter systems being involved in olfactory perception and processing. All of them carry out distinct functions on the different neurons present in the olfactory bulb and thereby shape the output to higher brain regions.

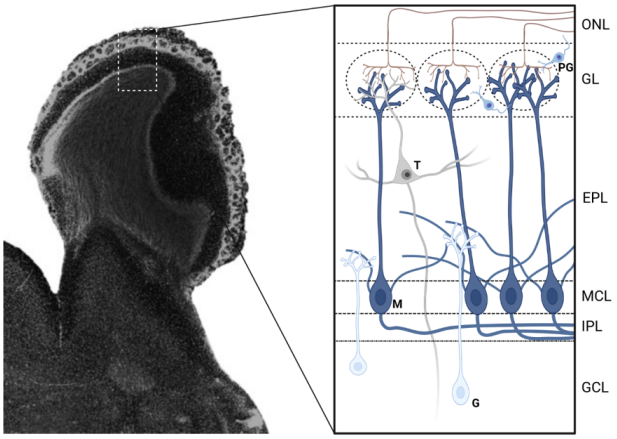

Figure 7: Rodent olfactory bulb anatomy

Scheme illustrating the rodent olfactory bulb anatomy with its different layers and cell types. Sagittal mouse brain slice stained against DAPI which shows the different olfactory bulb layers. Through the outer most layer, the olfactory nerve layer (ONL), olfactory sensory neurons (OSN) take in signals to the olfactory bulb. In the glomerular layer (GL), mitral cell axons take in those information and process them by fine tuning of neighboring cells (tufted cell (T), periglomerular cells (PG), granular cells (G)). Mitral cells, are the main output neurons, with their soma located in the mitral cell layer (MCL) and send all incoming signals through the internal plexiform layer (IPL) to higher brain regions for further processing (Graphic was created on BioRender).

Noradrenergic system:

In rodents, about 40 % of LC neurons project to the OB, innervating all five layers the OB is composed off with different innervation strength [128]. All OB neurons express at least one of the noradrenergic receptors $\alpha 1$, $\alpha 2$ or β. Mitral cells the main output neurons of the OB even express all three receptors, thereby beeing highly modulated by noradrenaline [129]. The main function of NA in the OB is to modulate the sensitivity and responsiveness of those mitral cells. It has been shown that NA can enhance the detection and discrimination of odorants by increasing the signal-to-noise ratio through regulating the strength of granular cell GABAergic inhibition onto mitral cells [130]. Moreover, NA has a potentiating effect on weak sensory inputs, meaning it modulates discrimination thresholds of low concentration stimuli. Infusion of NA into the OB was shown to improve odor detection and discrimination as a function of NA and odor concentration [75, 131]. Blockage of the two noradrenergic receptors α and β impairs the ability to discriminate

similar odors [132–134].

Cholinergic system:

The OB receives cholinergic input via the neurotransmitter acetylcholine coming from the basal forebrain nucleus basalis of Meynert [135, 136]. Cholinergic axons mainly innervate the glomerular layer and act on cells expressing nicotinic and muscarinic receptors, here mainly the GABAergic interneurons, periglomerular cells and granule cells [137–139]. Acetylcholine modulates the interaction between different olfactory neurons by bilateral inhibition, making them less sensitive to weak odorants, which sharpens the specificity and temporal precision of olfactory response. Several studies have demonstrated that acetylcholine shapes olfactory short-term memory and blocking it causes olfactory learning impairments [138, 140].

Dopaminergic system:

While the highest number of dopaminergic neurons can be found in the substatia nigra, ventral tegmental area and hypothalamus, another group of dopaminergic neurons is present in the olfactory bulb. Three dopaminergic interneuron types (periglomerular cells, short-axon cells and external tufted cells) line the glomeruli of the gomerular layer, thereby receiving direct olfactory input, which assigns them an important role in odor processing. Additionally, tracer experiments revealed the substantia nigra to innervate the olfactory bulb. Mainly neurons from the substantia nigra pars compact send their axons to the external plexiform layer and granular cell layer, where they release dopamine and thereby modulate local neurons [141]. Partial depletion of substantia nigra neurons by the neurotoxin 6-OHDA was shown to cause a reduction in the ability to discriminate odors and it impaired olfactory spatial memory in these animals [141, 142].

Serotonergic system:

Serotonergic signaling plays an important role in the filtering of olfactory input and formation of short-term memory in olfaction [143, 144]. Serotonergic axons originate from the raphe nuclei and terminate in the gomerular layer in the OB, while sending out axon collaterals to the mitral cell and granular cell layer [145]. Serotonin can directly excite mitral cells and tufted cells by binding to their 5HT2A receptors [146, 147]. Moreover, serotonin can increase the inhibition of periglomerular interneuons resulting in an enhanced spon-

taneous firing frequency of mitral cells, enhancing their sensitivity to olfactory inputs [51, 143]. The application of serotonin antagonists have been shown to impair learning of an olfactory task, while application of serotonin agonists enhances learning and short-term memory of the same task [148, 149]. Deaden serotonergic axons with the help of a neurotoxin produces glomerular atrophy and anosmia in rats [150].

In Alzheimer's disease, there is a significant reduction in all four neuronal cell populations and their neurotransmitters [151–153]. Already MCI patients have a measurable decline of noradrenergic and dopaminergic neurons, while cholinergic and serotonergic neuron loss is rather low. Transitioning to AD all four systems are heavily impaired with the serotonergic neurons beeing most resistant. The dysfunction of either of the systems was shown to result in decreased olfactory sensitivity and impaired odor discrimination, which potentially suggests a dominant role for all neurotransmitter systems being involved in neurodegenerative diseases [151, 153].

1.3.3 Olfactory system in Alzheimer's disease

In Alzheimer's disease, the olfactory system is particularly vulnerable early on. Olfactory function declines with age and people older than 60 years are prone to show olfactory deficits ranging from low impairments such as trouble in odor identification to anosmia. Notably, men are earlier and more severely affected than women [154, 155]. In a study from Hummel et al., 2007, smell identification tests on healthy people showed that odor thresholds decline first and most dramatically compared to odor discrimination or odor identification (Fig. 8a) [155].
Interestingly, healthy people with low olfactory test scores could be associated with future cognitive deficits and an increased risk of developing AD within the next 2-5 years [156]. Looking at mild cognitive impaired patients, approximately 60 % suffer from an impaired sense of smell and the degree of hyposmia often correlates with the degree of cognitive dysfunction. A two year-follow-up study on these patients showed 47 % to transition from MCI to AD (Fig. 8b) [157]. Various other studies carried out odor identification tests with similar results, which are summarized in the publication from Murphy et al., 2019 [158].
Next to these clinical assessments, AD post-mortem brain analysis revealed an overall

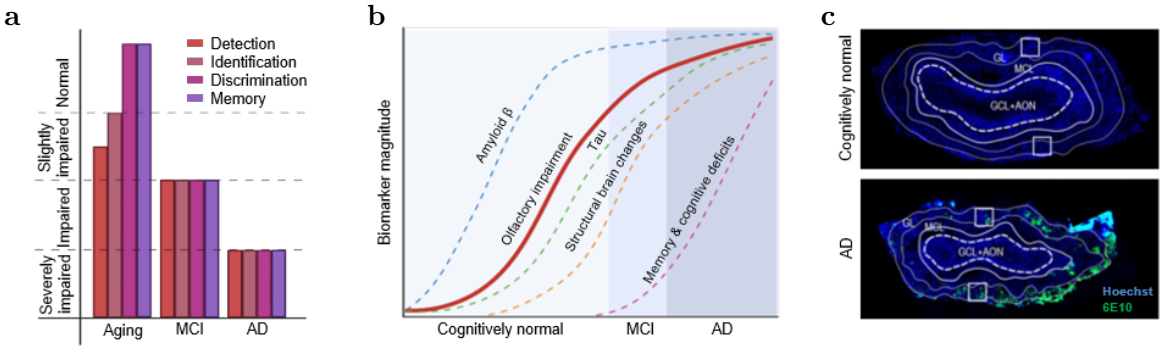

Figure 8: Olfactory impairment as biomarker for prodromal AD

(a) Bar graph visualizing the degree of olfactory impairment in aged, mild cognitive impaired (MCI) and AD patients. Already aged patients have slight difficulties in the detection and identification of odors. At the stage of MCI, patients show odor impairment in all four categories: detection, identification, discrimination and memory. When diagnosed with AD, all odor abilities worsen to a severe impairment (Modified after Slabik and Garaschuk, 2023 [151]). **(b)** Olfactory impairment is an early indicator for developing AD, occurring several years before memory and cognitive decline (Redrawn after Murphy et al., 2019 [158]). **(c)** Coronal olfactory bulb section of a cognitively normal human patient and an AD patient, stained against Hoechst and 6E10, an Aβ marker. The volume of the AD olfactory bulb is decreased and the glomerular cell layer contains a high Aβ plaque load (Modified after Son et al., 2022 [164]).

shrunken olfactory bulb with significant reduction in the volume and number of glomeruli and a decline of dopaminergic neurons surrounding the gomeruli, that ultimately impairs the processing of olfactory information (Fig. 8c) [159]. Aβ pathology is most prominent in the glomerular cell layer and anterior olfactory nucleus whereas Tau is mainly located in the anterior olfactory nucleus [159, 160]. The main risk factor for olfactory impairment, next to aging and gender [151, 154], is the genetic carriage of an apolipoprotein E4 (ApoE4) allele [161, 162]. Josefsson and colleagues showed odor identification to decline twice as fast in homozygous carrier of the ApoE4 allele compared to non-carriers [162]. Moreover, atrial fibrillation, cerebrovascular disease, and smoking were found to be risk factors for olfactory dysfunction [163].

2 Aim of study

This PhD project aimed to investigate how degeneration of the LC-noradrenergic system shapes olfaction as an early neurological impairment in Alzheimer's disease.

The LC, a crucial and well connected nucleus in the brain, displays toxic protein aggregates and cell loss early on in the course of Alzheimer's disease. Its degeneration was shown to have far-reaching effects on various cognitive processes and is associated with the emergence of several characteristic symptoms of the disease, one of which is hyposmia, a reduction in the sense of smell. About 60 % of patients with prodromal AD exhibit olfactory deficits, often several years before the onset of other cognitive symptoms. To date, no causal therapies to treat the disease are available. However, recent Aβ targeting antibody-therapies moderately improve cognitive decline in patients at early AD stages. This highlights that therapeutic success is critically dependent on early disease diagnosis. Therefore, a detailed understanding of the mechanisms prior to the onset of first cognitive symptoms is necessary. The early vulnerability of the LC system has gathered great attention from researchers worldwide, however no-one has yet fully studied the connection between LC degeneration and olfactory deficits. Asking for the causal link between LC-noradrenergic system and olfaction, we employed a variety of molecular and behavioral experiments using an Aβ-pathology AD mouse model and translated our data to human AD patients. In detail, the goal of this study was to identify at what age LC system degeneration and accompanied olfactory deficits start, what causes the LC axon damage, its loss and eventually hyposmia, and whether it is possible to decelerate or even prevent it.

Taken together, this project aimed to shed light on the underlying mechanism of LC system degeneration driving olfactory impairment in Alzheimer's disease.

3 Results

The present dissertation is based on my first author publication entitled *"Noradrenergic axon loss drives olfactory dysfunction in Alzheimer's disease"*. The manuscript is under revision at Nature Communications and available as a preprint at Research Square.

Carolin Meyer et al. Noradrenergic axon loss drives olfactory dysfunction in Alzheimer's disease, 02 October 2024, Preprint (Version 1) available at Research Square [https://doi.org/10.21203/rs.3.rs-4887136/v1] [1]

3.1 Immunohistological characterization of the LC-noradrenergic system in the APP$^{\text{NL-G-F}}$ mouse model

The LC is a small nucleus with relatively little cells but it has an extensive connectivity and broad impact compared to other brain regions. Its axons innervate almost the entire CNS and distribute the neurotransmitter noradrenaline, thereby contributing to a variety of physiological processes. Degeneration of these axons can therefore have severe effects on the normal functioning of the brain. The APP$^{\text{NL-G-F}}$ mouse line is a commonly used mouse model for studying AD with the advantage that APP is not overexpressed. Instead, pathogenic Aβ levels are elevated. Intensive research has been made on the LC's function and LC axon degeneration has been reported in the hippocampus and cortex of those mice. However, the study was conducted at the late disease stage, between 12 and 24 months of age, at which time point the Aβ pathology peaks [165]. In our study, we therefore aimed to use young animals in order to tackle the disease starting point and investigate if LC axon loss might already be detected earlier in other brain regions.

3.1.1 LC axon projections to the olfactory bulb

In rodents about 40 % of LC neurons project to the olfactory bulb [128, 166]. To visualize LC axons we used the NET antibody. NET is highly expressed on LC somata and axons as

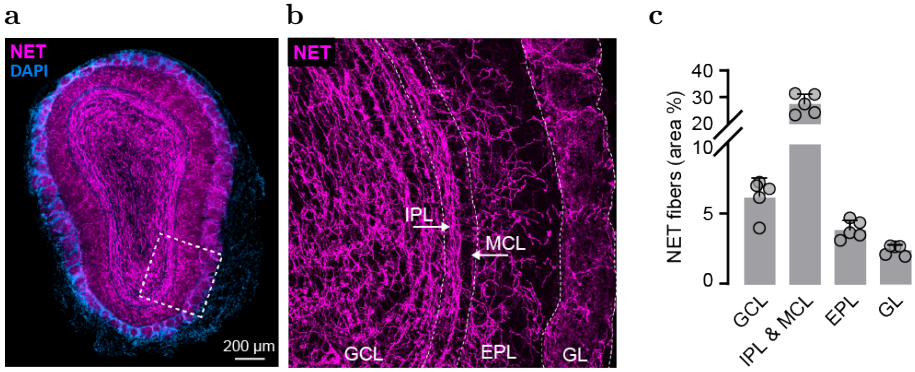

Figure 9: LC axon innervation in the olfactory bulb

(a) Coronal slice of the olfactory bulb from a C57BL/6J mouse showing axonal projections of LC neurons, stained against NET (magenta) and the different layers visualized with DAPI (blue). The dashed box highlights the imaging region. **(b)** Zoomed-in view using a 10x magnification onto the ventral side of the OB, taking a closer look at the distribution of NET fibers. **(c)** Quantification of the LC axon density per layer from n = 5 C57BL/6J animals. The internal plexiform layer (IPL) contains the highest amount of NET fibers, followed by the granular cell layer (GCL). The glomerular layer (GL) and mitral cell layer (MCL) have the least NET fibers; Data are expressed as mean ± SEM.

it is necessary for the re-uptake of noradrenaline from the synaptic cleft and can therefore specifically be used to stain LC axons. Quantification of the LC axon density in the OB of WT animals showed LC projections to target all layers. The internal plexiform layer is most heavily innervated with about 30 % axon density. The mitral cell layer on the other hand is almost devoid of LC axons. In the outer most layer, the glomerular layer, LC axons branch and surround the glomeruli. (Fig. 9a-c).

3.1.2 Early-onset LC axon degeneration in the olfactory bulb

By systematic comparison of multiple brain regions, we found early LC axon degeneration exclusively in the olfactory bulb of $APP^{NL\text{-}G\text{-}F}$ mice, starting between 1 and 2 months of age. At 1 month of age, the LC axon density was unaltered compared to WT animals, excluding the possibility of innate LC axon loss in this region. At 2 months of age, we detected a fiber reduction of 14 % and with increasing age the axon loss progressed to 27 % at 3 months, 33 % at 6 months and peaked at 12 months with 41 % loss (Fig. 10a,b). No difference in LC axon density was seen when comparing male and female mice. Next,

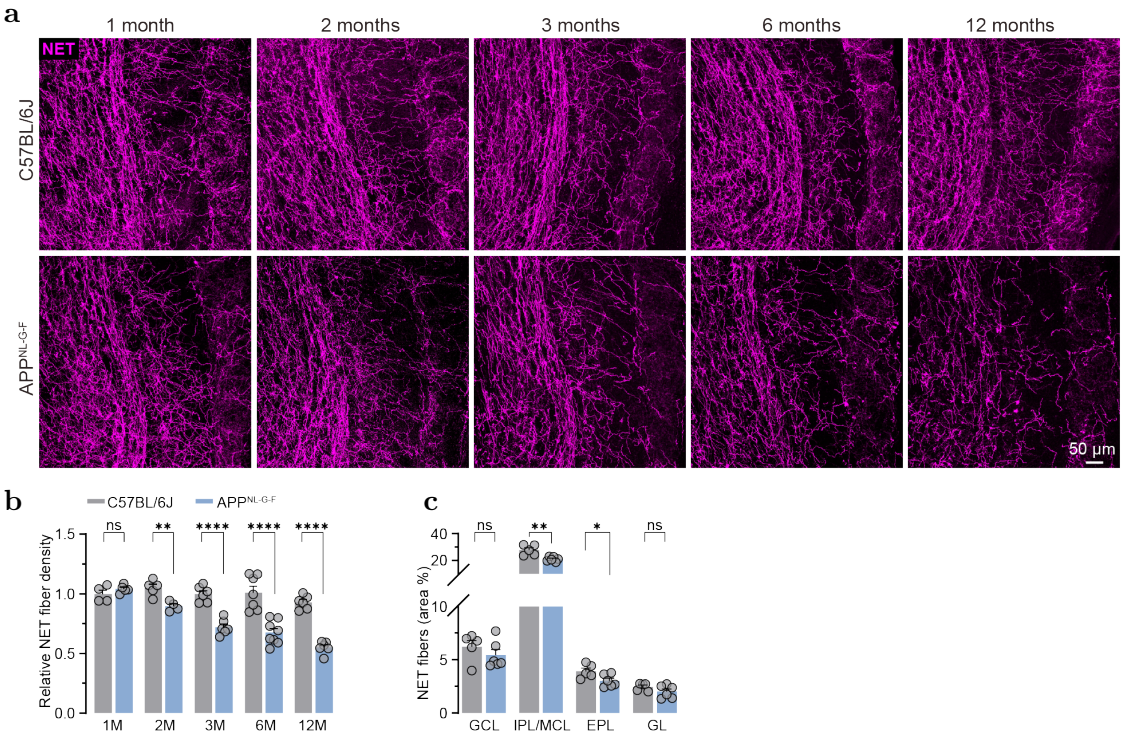

Figure 10: Early-onset LC axon degeneration in the olfactory bulb

(a) Representative pictures of an immunofluorescent stain against NET (magenta), comparing the LC axon density in the OB of C57BL/6J and $APP^{NL\text{-}G\text{-}F}$ mice. **(b)** Quantification of LC axon density (n = 4-8 mice per genotype/age, 4 pictures per animal). Axons degenerate in an age dependent manner, starting as early as 2 months of age. **(c)** At 3 months of age, the LC axon density per layer is most heavily reduced in the internal and external plexiform layer (n = 5-6 mice per genotype); Data are expressed as mean ± SEM; ns, not significant; *p<0.05, **p<0.01, ****p<0.0001.

we analyzed the different layers the olfactory bulb is composed of independently. We identified the heaviest innervated layer, the internal plexiform layer to show the strongest fiber loss, followed by the external plexiform layer (Fig. 10a,c).

3.1.3 LC axon loss in other brain regions

Asking if the olfactory bulb is a unique region that displays LC axon loss especially early, we analyzed several other brain regions that are affected in Alzheimer's disease. The piriform cortex (Pir), medial prefrontal cortex (mPFC) and dentate gyrus (DG) of the

hippocampus of 6-month-old $APP^{NL\text{-}G\text{-}F}$ mice have an equal NET fiber density compared to WT mice. The somatosensory cortex (S1) suffers from LC axon degeneration of about 10 % at 6 months of age (Fig. 11a,b,c). In comparison, NET fibers in the OB are reduced by 33 % at 6 months of age. Looking at the microglia density and Aβ plaque load, all regions displayed prominent, large Aβ-plaques accompanied by an increase in microglia which accumulate around the plaques (Fig. 11b).
In summary, we conclude that the olfactory bulb is, to our best knowledge, and out of the regions analyzed, the only brain region effected by very early LC axon loss, starting at 2 months of age and declines progressively, while in other brain regions LC axon degeneration does not start before 6 months of age.

3.1.4 Microgliosis and Aβ plaques in the olfactory bulb

The $APP^{NL\text{-}G\text{-}F}$ mouse line is an Aβ pathology model. According to Saito et al., 2014, Aβ plaque deposition starts at 2 months of age and increases steadily up until 12 months of age before it saturates. Mainly in the cortex and hippocampus Aβ was shown to accumulate early on. Microglia, the immune cells of the brain are constantly surveying the environment, extending their processes to look out for dying neurons, injury or toxic protein aggregates like Aβ. Heavy microgliosis was detected around Aβ-plaques.
To check for Aβ and microglia in the olfactory bulb, we immunohistochemically labeled them and quantified their densities. First Aβ-plaques form at 2 months of age, mainly located in the internal plexiform layer (Fig. 12a,c). An increased microglia density (+15 %) was observed also at 2 months of age comparing $APP^{NL\text{-}G\text{-}F}$ to WT mice (Fig. 12a,b). With increasing age more Aβ-plaques were detected, as well as a higher microglia density. Correlating the area covered by microglia and Aβ at the age of 3 and 6 months showed a positive correlation, with both variables increasing together (Fig. 12d).

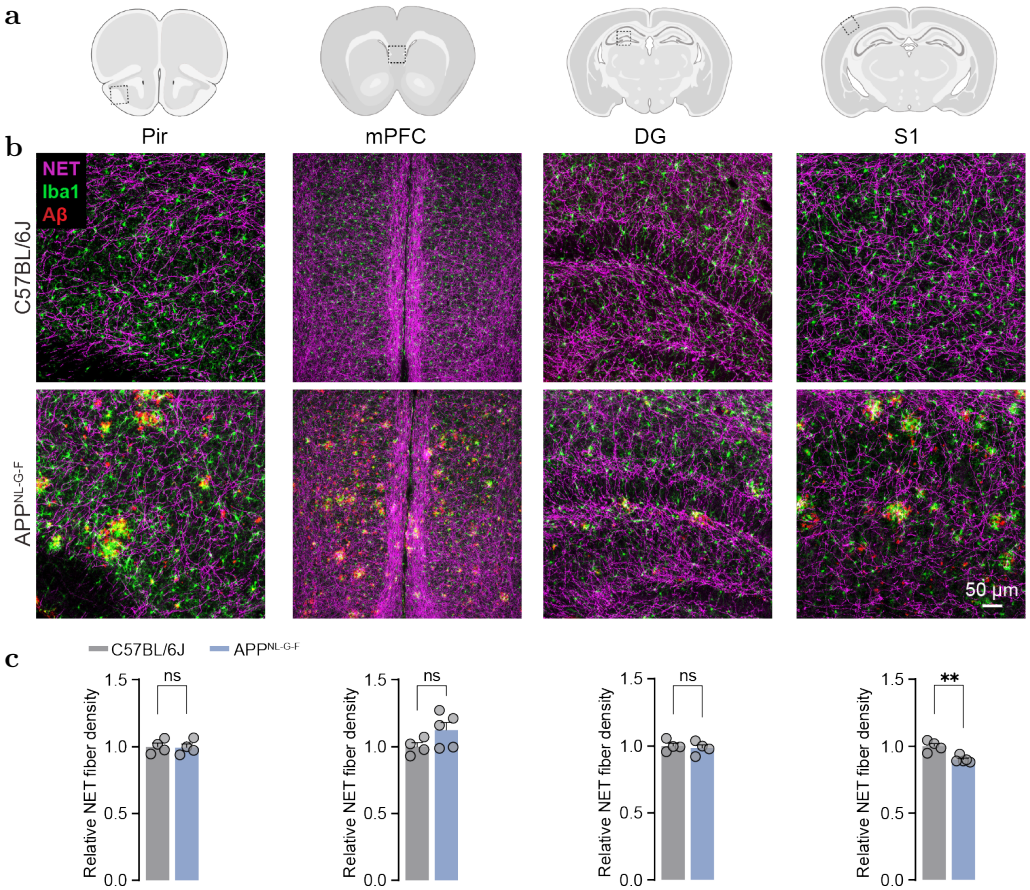

Figure 11: LC axon density in other brain regions

(a) Scheme illustrating the imaging region in different brain areas. **(b)** Representative pictures of an immunofluorescent stain against NET (magenta), Iba1 (green) and Aβ-plaques (red) in the respective regions, comparing C57BL/6J and APP$^{\text{NL-G-F}}$ mice at 6 months of age. **(c)** Quantification of relative NET fiber density in the piriform cortex (Pir), medial prefrontal cortex (mPFC) and dentate gyrus (DG) shows no difference between the groups. In the somatosensory cortex (S1) NET fibers are reduced (n = 4-6 mice per genotype, 3 slices per animal); Data are expressed as mean ± SEM; ns, not significant; **p<0.01.

3.2 LC axon loss and reduced noradrenaline release in the olfactory bulb drive olfactory dysfunction

3.2.1 APP$^{\text{NL-G-F}}$ mice experience olfactory impairment

Early sensory impairments such as hyposmia, a reduced ability to detect odors, have been well described in prodromal AD. Hence, we aimed to analyze whether LC axon loss in the

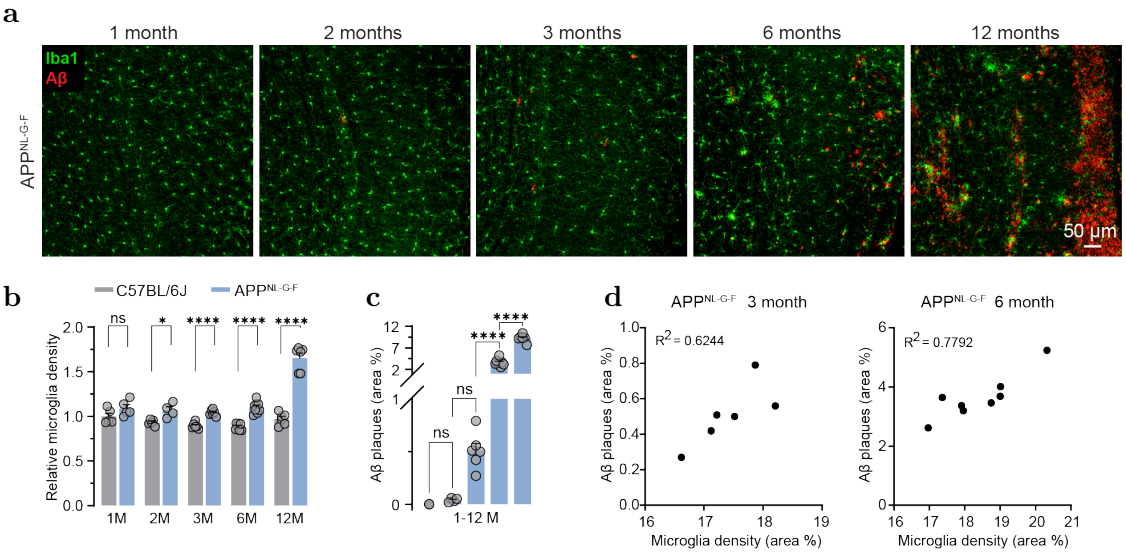

Figure 12: Microgliosis and Aβ-plaque deposition in the olfactory bulb

(a) Representative pictures of an immunofluorescent stain against microglia (Iba1, green) and Aβ-plaques (NAB228, red) in the OB of APP$^{\text{NL-G-F}}$ mice at different age points. **(b)** Quantification of microglia density in APP$^{\text{NL-G-F}}$ mice in comparison to C57BL/6J mice (n = 4-8 mice per genotype/age, 4 pictures per animal). The microglia density starts to increase at 2 months of age and progressively elevates with increasing age. **(c)** Aβ-plaques start to form at 2 months of age and grow in size and number with increasing age. **(d)** Correlation analysis between Aβ-plaque load and microglia density (n = 4-8 mice per genotype/age, 4 pictures per animal); Data are expressed as mean ± SEM; ns, not significant; *p<0.05, ****p<0.0001.

OB results in olfactory impairment in APP$^{\text{NL-G-F}}$ animals. We employed the buried food test, a simple olfactory task to measure the ability of animals to detect volatile odors. Animals were food deprived for 18 h and subsequently placed in a fresh bedding cage with a buried single junk of regular rodent food (Fig. 13a). When testing animals at one month age, we did not observe any differences in the time needed to find the buried food pellet comparing the groups, which is consistent with the lack of LC axon degeneration at that age (Fig. 13a and 10a,b). At 3 months of age, WT animals usually revealed the food within 40 s. In contrast, 3-month-old APP$^{\text{NL-G-F}}$ mice needed 60 % more time to find the buried food pellet (WT: 39.86 s ± 8.26 s, APP$^{\text{NL-G-F}}$: 64.39 s ± 24.53 s). This behavioral phenotype was consistent in 6-month-old animals, where some animals were not able to locate the food in the maximum allowed time of 10 minutes (WT: 97.86 s

± 50.95 s, $APP^{NL\text{-}G\text{-}F}$: 253.40 s ± 155.60 s; Fig. 13a,b). Interestingly, looking at WT animals only, over the life span from 1 to 3 and 6 months of age, the time to find the food pellet increased steadily, from 35 s to 40 s and 98 s, highlighting the normal decay of the olfactory sense.

Additional to the buried food test, we recapitulated our findings in another olfactory task. 3-month-old WT and $APP^{NL\text{-}G\text{-}F}$ mice underwent an olfactory sensitivity test (Fig. 13c) using a vanilla odor which was identified as a well-received odor by the animals. We exposed the animals to ascending concentrations of vanilla and measured the time the animals spend in close vicinity (<2 cm) to the odor delivery stick and the amount of times they visited the odor stick. WT animals were readily attracted by a low vanilla dilution of 1:1000 and repeatedly interacted with the odor stick, while $APP^{NL\text{-}G\text{-}F}$ mice visited the interaction zone for shorter times and less often (Fig. 13d-f). Importantly, both variables significantly increased in WT animals when dilutions were increased to 1:1, while $APP^{NL\text{-}G\text{-}F}$ mice did not change their behavior compared to the lower dilution (Fig. 13d-f). Collectively, these data clearly support the results of our buried food task and revealed a consistent olfaction phenotype in $APP^{NL\text{-}G\text{-}F}$ mice, already at the age of 3 months, which is to date the earliest behavioral phenotype described in this mouse model.

3.2.2 In vivo noradrenaline release coupled to olfactory stimulation is reduced in $APP^{NL\text{-}G\text{-}F}$ mice

We set out to understand whether LC axon loss results in reduced NA release in the OB and whether this is the underlying reason for the observed olfactory deficits. First, we measured the baseline NA level using a NA ELISA. Interestingly, we did not observe a different concentration of baseline NA in the OB of $APP^{NL\text{-}G\text{-}F}$ animals compared to WT mice (Fig. 14a). We thus hypothesized that a change in NA levels would be more pronounced in a stimulus-related event. Therefore, we transduced the olfactory bulb of 2-month-old $APP^{NL\text{-}G\text{-}F}$ animals with the noradrenaline sensitive biosensor $GRAB_{NE}$ and implanted a chronic cranial window over the olfactory bulb (Fig. 14b). 1 month later, we performed acousto-optical 2-photon imaging in these animals paired with olfactory stimulation by 10 s long vanilla puffs. WT animals reliably and repeatedly responded to odor delivery

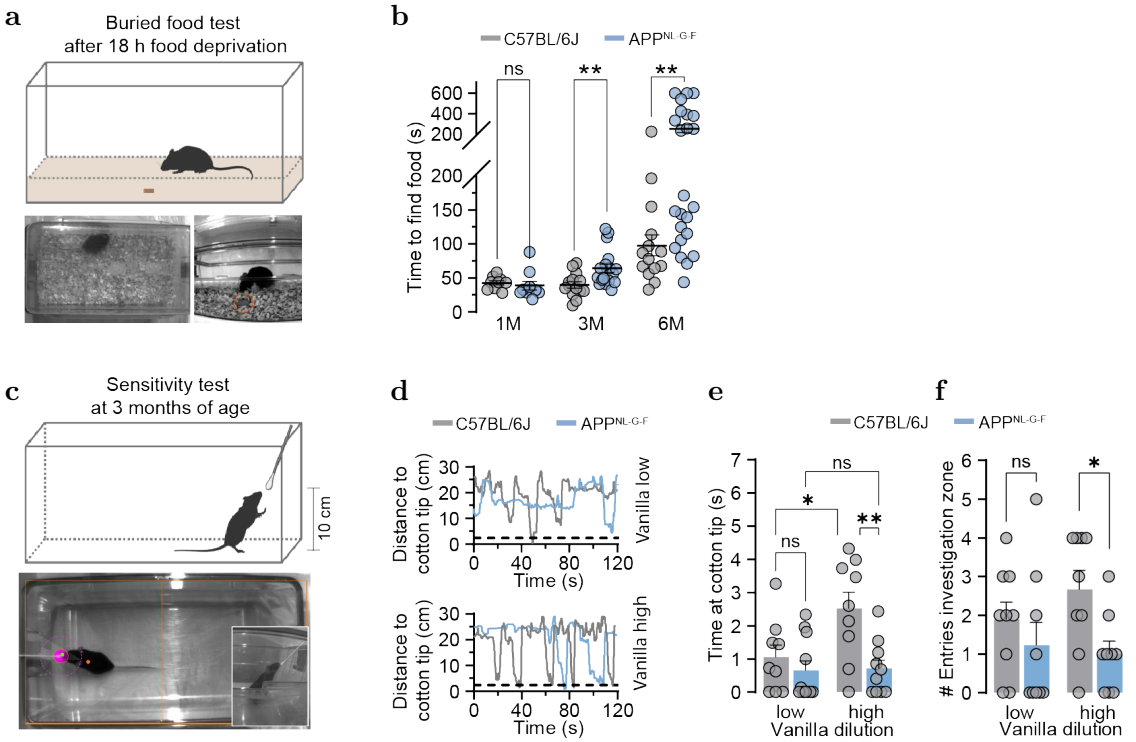

Figure 13: APP^{NL-G-F} mice show olfactory deficits

(a) Experimental setup of the buried food test and pictures taken during a recording from the top and side angle. **(b)** In the buried food test, APP^{NL-G-F} mice need more time to find a hidden food pellet at 3 and 6 months of age, compared to C57BL/6J mice (n = 10-24 mice per genotype/age). **(c)** Experimental setup of the sensitivity test with pictures taken during the recording from a top and side angle. **(d)** Exemplary traces of the distance versus time C57BL/6J and APP^{NL-G-F} mice spend at a low (1:1000) and high (1:1) vanilla concentration. **(e)** Time spend sniffing at the different vanilla dilutions. APP^{NL-G-F} mice spend little time sniffing at both concentrations. **(f)** Number of entries to the investigation zone (<2 cm from odor delivery stick). APP^{NL-G-F} mice visit the odor delivery stick less often than C57BL/6J mice (n = 9-11 mice per genotype); Data are expressed as mean ± SEM; ns, not significant; *p<0.05, **p<0.01.

with a strong and long lasting increase of fluorescence across the whole frame (Fig. 14c). In contrast, delivering odor to APP^{NL-G-F} exhibited a drastically decreased responsiveness to the vanilla odor (Fig. 14c-e). As a control, we applied an air puff without odor to the animals and could see that both groups showed a small, but not significant response from to baseline and importantly no difference between the genotypes (Fig. 14h). Hidden under the prominent response to the odor applications, we also observed spontaneous NA release with low amplitudes in both genotypes. NA is known to be released in response to

other sensory stimuli and during locomotion. Testing the $GRAB_{NE}$ sensor in the cortex, a region involved in locomotion, showed no response to odor delivery (Fig. 14i,j). These control experiments prove our strategy to be sufficient to specifically monitor odor induced NA release in the olfactory bulb. Subsequent immunofluorescent analysis revealed a solid virus transduction in the olfactory bulb and a 20 % decline of LC axons in $APP^{NL\text{-}G\text{-}F}$ animals compared to WT animals (Fig. 14f,g).

3.2.3 Optogenetic inhibition of noradrenaline release in the olfactory bulb cannot recapitulate impaired olfaction

To functionally couple the olfactory deficit to a decreased NA release, we planned to mimic the olfactory phenotype observed in $APP^{NL\text{-}G\text{-}F}$ mice by inhibiting the NA release in the OB of WT animals by optogenetics. To this end, we bilaterally transduced LC neurons of 2-month-old Dbh-Cre animals either with the inhibitory opsin eNpHR3.0 or with EYFP as controls. Subsequently, an optical fiber was placed in the olfactory bulb midline of the same animals (Fig. 15a). Since eNpHR3.0 may suffer from inactivation upon prolonged stimulation we performed electrophysiological recordings from LC neurons of Dbh-eNpHR3.0 animals and confirmed that photostimulation by 520 nm is sufficient to induce prolonged neuronal inhibition of LC activity without persistent inactivation (Fig. 15b,c). In the OB, photoinhibition of NA axons reduced the mitral cell activity, which renders our strategy as ideal to analyze the impact of decreased NA during an olfactory behavior test (Fig. 15b,c). 1 month post injection, we exposed the animals to the buried food task with continuous photoinhibition of NA release in the olfactory bulb, starting 2 minutes before the test. Surprisingly, both groups needed a long time to find the buried food pellet. Dbh-eNpHR3.0 animals, contrary to our assumption, needed the same amount of time to find the food pellet than control injected Dbh-EYFP animals (Fig. 15d,e). Thus, mimicking olfactory deficits in WT animals by the inhibition of NA release did not work with the chosen experimental setup.

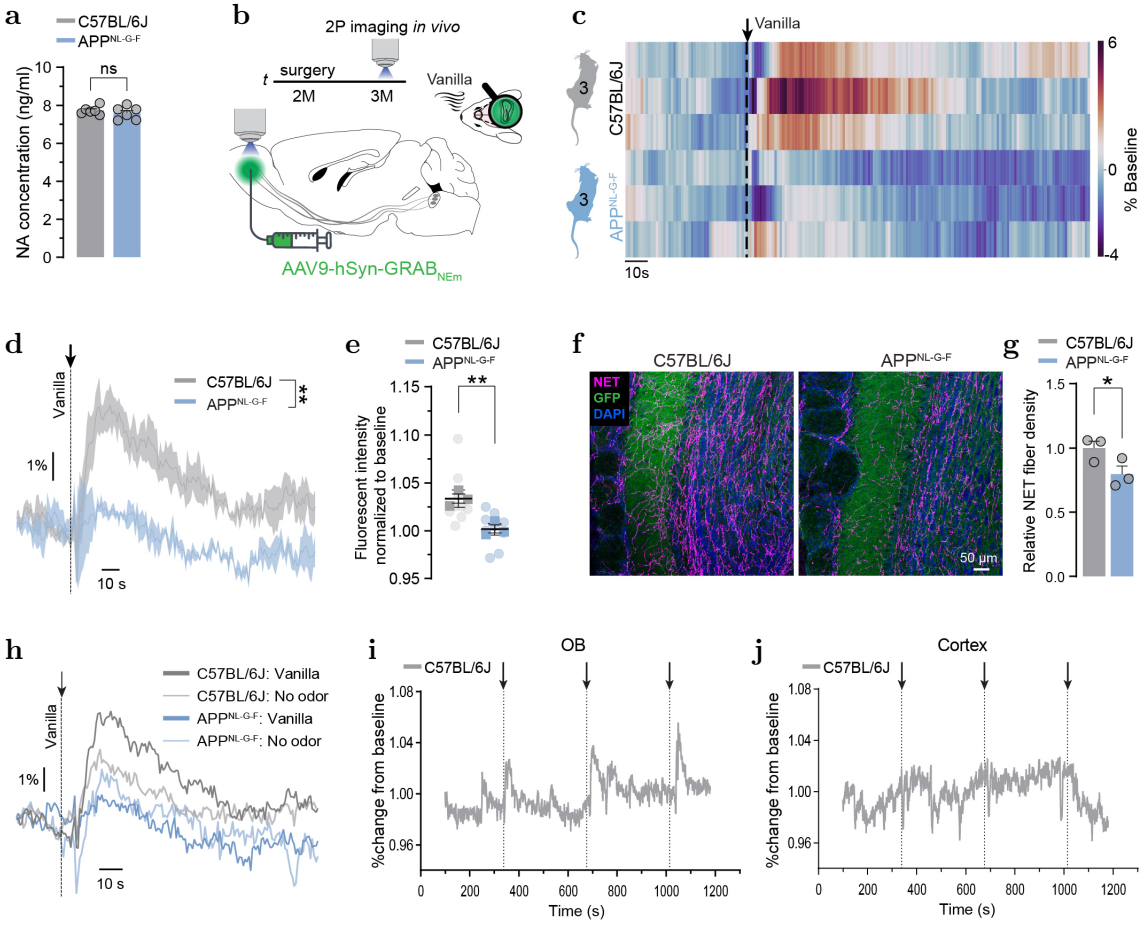

Figure 14: In vivo measurement of noradrenaline release in the olfactory bulb

(a) Noradrenaline (NA) concentration in the olfactory bulb assessed by NA ELISA shows no difference between the groups in 3-month-old animals (n = 5 mice per genotype) **(b)** Experimental setup of NA release measurement in vivo. A NA sensor got injection into the OB of 2-month-old mice (n = 3 mice per genotype). 1 month later, mice got imaged under the 2-photon microscope, stimulating NA release by vanilla air-puffs. **(c)** Heat map shows NA release of single animals when exposed to a vanilla air puff. **(d)** Percental NA release in response to a vanilla air-puff is significantly lower in $APP^{NL\text{-}G\text{-}F}$ mice than in C57BL/6J mice. **(e)** Fluorescent intensity per animal. **(f)** Immunofluorescent pictures visualizing an equal expression of the virus in the OB and a degeneration of NET fibers in $APP^{NL\text{-}G\text{-}F}$ mice. **(g)** Quantification of NET fiber density. **(h)** NA response to a vanilla air-puff or a control air-puff compared between C57BL/6J and $APP^{NL\text{-}G\text{-}F}$ mice. **(i)** NA response to three consecutive vanilla air puffs imaged in the OB and **(j)** in the cortex of a C57BL/6J animal; Data are expressed as mean ± SEM; *p<0.05, **p<0.01.

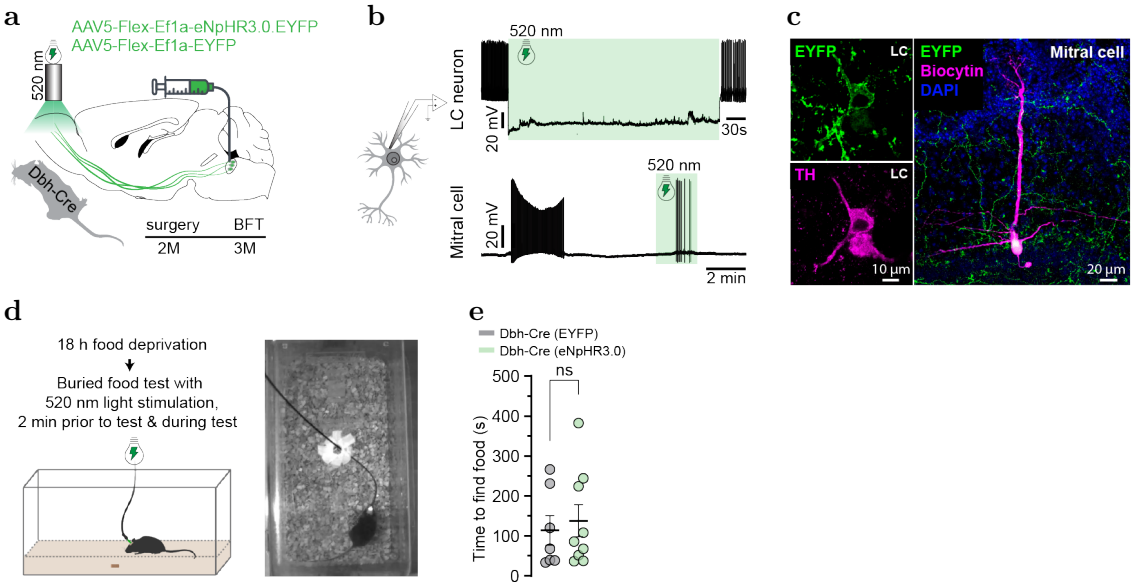

Figure 15: Inhibition of noradrenaline release in the olfactory bulb cannot recapitulate olfactory impairment

(a) Experimental setup of inhibitory opsin injection into the LC and fiber implantation into the OB of Dbh-Cre mice at 2 months of age (n = 7 vs. 9 mice). **(b)** Patch-clamp recording of a LC neuron under 520 nm light stimulation. The cell hyperpolarizes and stops firing. Mitral cells in the OB reduce their firing activity under the inhibition of noradrenaline release. **(c)** Immunofluorescent pictures showing the expression of the virus (EYFP, green) inside LC neurons (TH, magenta) and inside NET fibers in the OB. **(d)** Experimental setup of buried food test with optogenetic stimulation. **(e)** Quantification of time to find the hidden food pellet. No difference between the groups was found; Data are expressed as mean ± SEM; ns, not significant.

3.2.4 Chemogenetic activation of LC neurons cannot rescue olfactory deficits in APP$^{NL\text{-}G\text{-}F}$ mice

The relationship between the decline of LC axons, NA release and impaired olfactory phenotype points towards a structure-loss to loss of function. Consequently, we asked if chemogenetic activation of remaining LC axons would be sufficient to reinstate olfaction. We bilaterally injected an AAV transducing LC neurons of 5-month-old APP$^{NL\text{-}G\text{-}F}$ × Dbh-Cre animals with an excitatory ligand-gated G-protein-coupled receptor (hM3DGq, designer-receptor exclusively activated by designed drugs, DREADD), that by the application of CNO excites LC neurons (Fig. 16a). In patch-clamp recordings, we confirmed that 3 µM CNO activates LC neurons, visualized by an increased spontaneous firing fre-

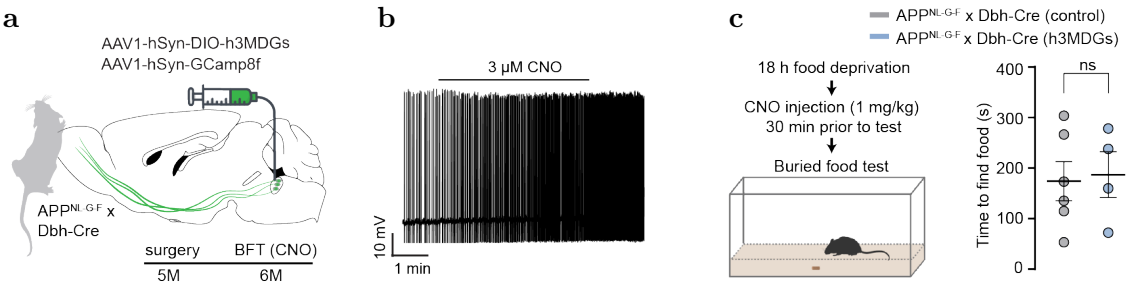

Figure 16: Chemogenetic activation of LC neurons has no effect on olfaction

(a) Experimental setup of DREADD (hM3DGq, designer-receptor exclusively activated by designed drugs) virus injection into the LC of 5-month-old APP$^{NL\text{-}G\text{-}F}$ × Dbh-Cre mice (n = 5 vs. 4 mice). **(b)** Patch-clamp recording of a LC neuron. The application 3 µM CNO increases the spontaneous firing of the cell for several minutes. **(c)** Experimental setup of the buried food test with CNO application. APP$^{NL\text{-}G\text{-}F}$ × Dbh-Cre control injected and hM3DGq injected mice need the same time to find the hidden food pellet; Data are expressed as mean ± SEM; ns, not significant.

quency (Fig. 16b). At 6 months of age, DREADD injected mice and control mice were challenged with the buried food test 30 min after one dosage of CNO. However, here in vivo, CNO-injection to activate excitatory DREADDs could not accelerate the time to find the food pellet. WT mice needed on average 174 s ± 61.57 s to find the food pellet and APP$^{NL\text{-}G\text{-}F}$ × Dbh-Cre animals needed 187 s ± 13.0 s (Fig. 16c). Collectively, LC over-activation did not rescue the impaired olfactory phenotype of APP$^{NL\text{-}G\text{-}F}$ × Dbh-Cre animals. This finding strongly suggests a structure-to-function-relationship of LC axons in the OB.

3.3 Electrophysiological characterization of LC neurons and mitral cells

3.3.1 APP$^{NL\text{-}G\text{-}F}$ LC neurons are hyperactive, but less excitable

Asking for the underlying mechanism of reduced NA release in the OB, we performed electrophysiological recordings from LC neurons in acute slices and compared whether LC neuron properties are altered.

First, by perforated patch-clamp recordings in current-clamp mode, we examined the spontaneous activity of LC neurons from 6-month-old mice. We found $APP^{NL\text{-}G\text{-}F}$ LC neurons to have a significantly increased firing frequency. WT neurons spike on average with 1.76 Hz ± 2.19 Hz, while $APP^{NL\text{-}G\text{-}F}$ neurons are hyperactive, firing at 3.95 Hz ± 0.69 Hz (Fig. 17b,c). However, it has to be noted that we observed a large variability in the spontaneous firing frequency in both genotypes.

To examine the electrophysiological properties of LC neurons in more detail, we applied a spectrum of stimulation protocols. We created a current-frequency curve to observe the cells firing frequency at specific excitatory current inputs (0 pA to 50 pA, 10 pA increments, 1 s). LC neurons of both genotypes spiked with a linearly increasing frequency, but in $APP^{NL\text{-}G\text{-}F}$ neurons less action potentials were generated than in WT LC neurons, meaning the neurons are less excitable (Fig. 17d,e). Injection of a current ramp (0 pA to 300 pA) was used to see how the cells reacted to strong stimuli and to calculate the rheobase current, the current needed to elicit the first action potential. A trend points towards an increased rheobase current in $APP^{NL\text{-}G\text{-}F}$ which fits to the less excitable phenotype (Table 1). Next, we looked at two other typical LC neuron characteristic, the delayed excitation and the slow afterhyperpolarization. Measuring the time it takes the neuron after a stimulated hyperpolarization during spontaneous activity to start firing again, we found the delayed latency to be increased the more the membrane potential hyperpolarizes. Comparing the latency between WT and $APP^{NL\text{-}G\text{-}F}$ mice there was no difference detected, though (Fig. 17f), and thus delayed excitation is not responsible for the increased firing frequency. Looking at the sAHP that follows a current-induced firing of action potentials, we found a positive correlation between the number of action potentials generated and the amplitude of the sAHP (at 50 pA current injection). WT neurons, which are more excitable to current stimulation have a strong sAHP, while $APP^{NL\text{-}G\text{-}F}$ neurons that spike less, also have a smaller sAHP amplitude (Fig. 17g, Table 1). In the next experiment, we extracted the cells intrinsic properties. Neither the input resistance, cell capacitance or time constant tau differed between the two genotypes (Table 1).

All in all, we found $APP^{NL\text{-}G\text{-}F}$ LC neurons to be hyperactive which was shown by an increased spontaneous firing frequency.

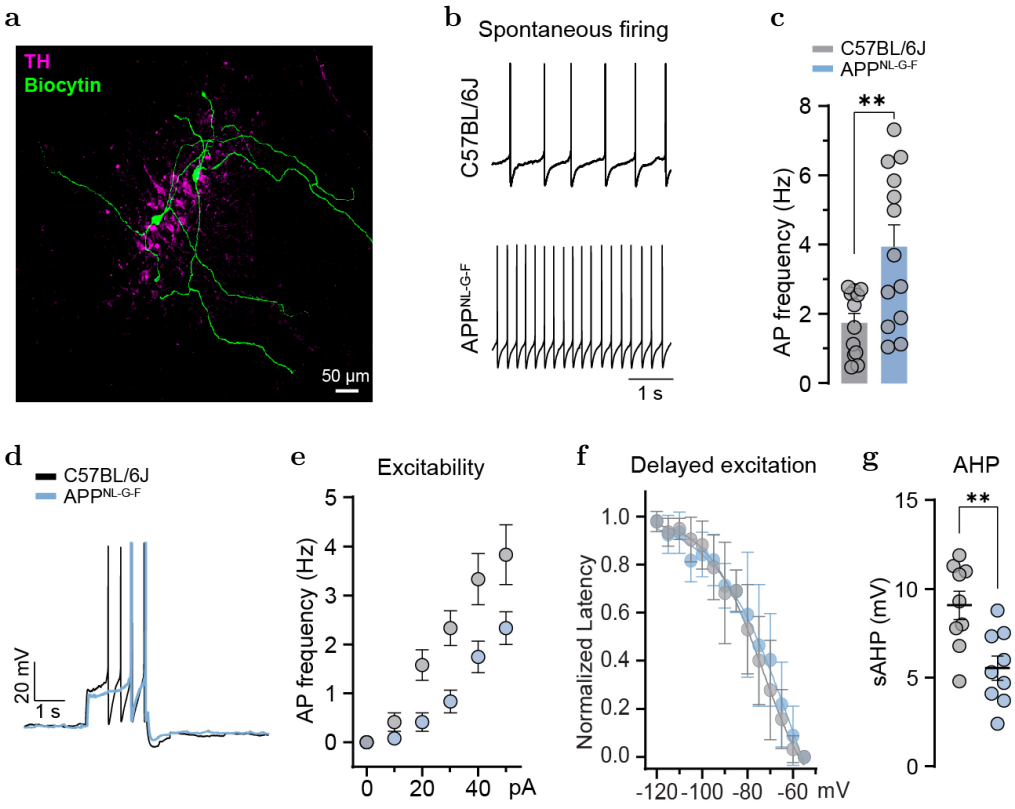

Figure 17: Electrophysiological properties of LC neurons

(a) Perforated patch-clamp recordings with subsequent biocytin-filling and post-hoc staining (Biocytin, green) visualizes two LC neurons in the LC region (TH, magenta). **(b)** Representative traces of the spontaneous action potential firing from a C57BL/6J and APP^{NL-G-F} LC neuron. **(c)** Quantification of action potential firing reveals LC neurons from APP^{NL-G-F} mice to be hyperactive (WT: n = 12, APP^{NL-G-F}: n = 13). **(d)** Representative traces of evoked action potentials (at 50 pA current injection). **(e)** Current-frequency curve shows LC neurons from APP^{NL-G-F} mice to be less excitable. **(f)** Quantification of delayed excitation (latency to fire next action potential) is similar in both genotypes. **(g)** Slow afterhyperpolarization (sAHP) is reduced in APP^{NL-G-F} mice (at 50 pA current injection); Data are expressed as mean ± SEM; **p<0.01.

3.3.2 Mitral cell integrity is not impaired in APP^{NL-G-F} mice

Mitral cells are the first order projection neurons in the olfactory bulb. Understanding their electrophysiological properties is crucial to unravel the mechanism underlying olfactory processing. In particular, we asked if a dysfunction of mitral cells, next to the reduced NA release in APP^{NL-G-F} mice could account for the olfactory impairment. To test this, we performed patch-clamp recordings of mitral cells from WT and APP^{NL-G-F} mice at

Table 1: Electrophysiological properties of LC neurons

Parameter	# WT	APP^{NL-G-F}	C57BL/6J	APP^{NL-G-F}	p-value
Spontaneous firing (Hz)	12	13	1.76 ± 0.69	3.95 ± 2.19	0.0045
Input resistance (Ω)	11	10	763.40 ± 75.86	634.60 ± 128.90	0.108
Capacitance (pF)	11	10	115.80 ± 21.31	123.60 ± 7.84	0.717
Time constant tau (ms)	11	10	86.52 ± 9.33	78.61 ± 7.90	0.461
Rheobase (pA)	11	10	17.92 ± 2.80	21.50 ± 3.58	0.218
sAHP amplitude (mV)	9	9	9.078 ± 3.54	5.54 ± 1.05	0.218

6 months of age and compared their electrophysiological extrinsic and intrinsic properties. Well in line with previous research, we found mitral cells to be spontaneously active, firing with various different firing patterns and frequencies (Fig. 18d). No difference in the spontaneous activity could be seen between the two genotypes. Stimulating the cells with negative and positive current injections, we found that the cells can be subdivided into two different subtypes, type 1 cells (WT: n = 13, APP^{NL-G-F}: n = 8) and type 2 cells (WT: n = 7, APP^{NL-G-F}: n = 11). So far, studies have only identified mitral cell subtypes by their laminar distribution based on immunohistochemical stainings. They are divided in type M1 cells that extract their secondary dendrites in the inner sublaminar layer of the external plexiform layer, whereas type M2 cells project their secondary dendrites to the outer sublaminar layer of EPL (Fig. 18a,b). Electrophysiologically, we identified mitral cells of type 1 to fire at high frequencies when stimulated, while mitral cells type 2 fire at lower frequencies due to a delayed excitation. Moreover, type 2 cells show a delayed repolarization back to baseline. None of the subtypes show a voltage sag, as it is common for pacemaker cells. We rather observed a negative sag in type 2 cells, plus a delay in bringing the membrane potential back to baseline (Fig. 18c). Comparing WT and APP^{NL-G-F} mitral cell subtypes no difference was observed with regard to the above listed characteristics and therefore we pooled them together for further analysis. The cells input resistance, capacitance and time constant tau was also comparable between the groups (Table 2). Creating a current-frequency curve for both mitral cell subtypes showed type 1 cells to be more excitable than type 2 cells, however when comparing the subtypes between APP^{NL-G-F} and WT animals, no difference in the firing frequency was detected

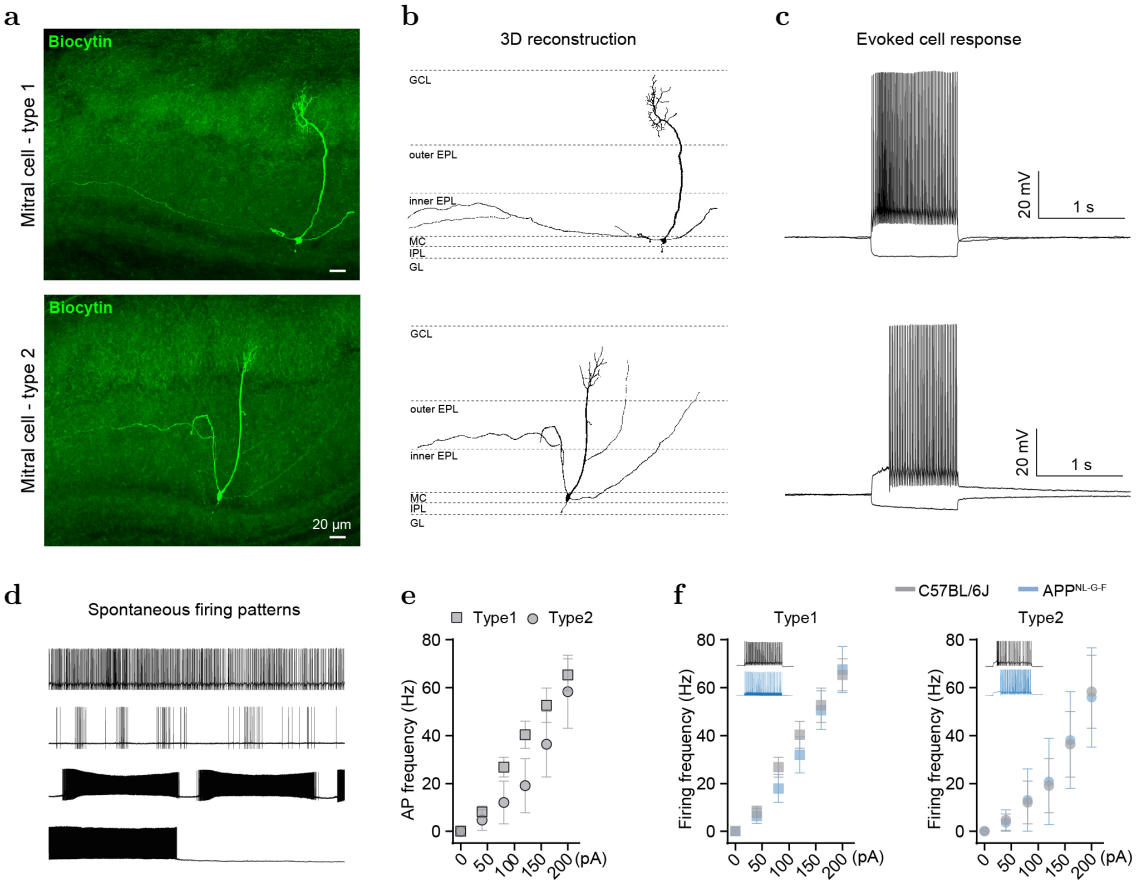

Figure 18: Electrophysiological properties of mitral cells in the olfactory bulb

(a) Perforated patch-clamp recordings with subsequent biocytin-filling and post-hoc staining (Biocytin, green) visualizes two morphologically different mitral cells in the olfactory bulb. **(b)** 3D reconstruction of biocytin-filled mitral cells shows type 1 cells to extend their dendrites into the inner external plexiform layer (EPL) and type 2 cells to span their dendrites in the outer EPL and glomerular cell layer (GCL). **(c)** Evoked cell response (-100 pA, +200 pA current injection) shows the two cell types to have different firing behaviors. **(d)** Mitral cells have diverse spontaneous firing patterns. **(e)** Current-frequency curve reveals that type 2 mitral cells fire less action potentials than type 1 cells. **(f)** Comparison of current-frequency responses in C57BL/6J and $APP^{NL\text{-}G\text{-}F}$ mice. No difference in the number of action potentials was found, neither in type 1, nor in type 2 mitral cells; Data are expressed as mean ± SEM.

(Fig. 18e,f). Biocytin fillings and post-hoc stainings with streptavidin were carried out after the recordings in order to reconstruct the morphology of mitral cells. From the cell body extends one primary dendrite to a single glomerulus in the glomerular layer and several lateral dendrites project to the external plexiform layer. We could match the electrophysiologically classified subtype 1 to the morphological subtype M1, which extends its

Table 2: Electrophysiological properties of mitral cells

Parameters mitral cells	# WT	APP^{NL-G-F}	C57BL/6J	APP^{NL-G-F}	p-value
Spontaneous firing	20	19	various patterns	no difference	
Input resistance (Ω)	12	16	89.77 ± 23.83	123.10 ± 33.32	0.173
Capacitance (pF)	12	16	237.00 ± 72.08	212.60 ± 24.40	0.738
Time constant tau (ms)	12	16	20.88 ± 5.38	25.21 ± 4.33	0.429
Rheobase (pA)	12	16	84.00 ± 18.55	84.26 ± 0.26	0.988

lateral dendrites into the inner sublaminar layer of the EPL and type 2 cells match type M2 cells projecting their dendrites into the outer sublaminar layer of the EPL and into the GCL (Fig. 18a-c).

3.4 Underlying mechanism of LC axon degeneration

3.4.1 Olfactory bulb microglia phygocytose LC axons

Microglia have been attracting considerable attention in the pathogenesis of AD. Since early axon loss coincides with an increased number of microglia, we set out to identify whether microglia could account for LC axon loss. To this end, we hypothesized that microglia phagocytose NET^+ axons in the OB. We performed near super-resolution imaging of NET fibers together with lysosomes in microglia and carried out 3D-reconstruction of these images (Fig. 19a). We found a higher volume of NET^+ protein in microglia cells from APP^{NL-G-F} mice compared to WT animals. Unexpectedly, WT microglia also contained a high amount of NET^+ protein (3.60 μm^3 ± 0.71 μm^3), however, significantly less than APP^{NL-G-F} microglia (6.19 μm^3 ± 2.59 μm^3). The microglia volume did not differ between the two genotypes, which speaks for healthy microglia. Instead, the volume of $CD68^+$ lysosomes inside microglia was increased (WT: 1.81 vol.% ± 0,21 vol.%, APP^{NL-G-F}: 2.52 vol. % ± 0.70 vol.%) suggesting an upregulated phagocytosis of APP^{NL-G-F} microglia in the olfactory bulb (Fig. 19b).

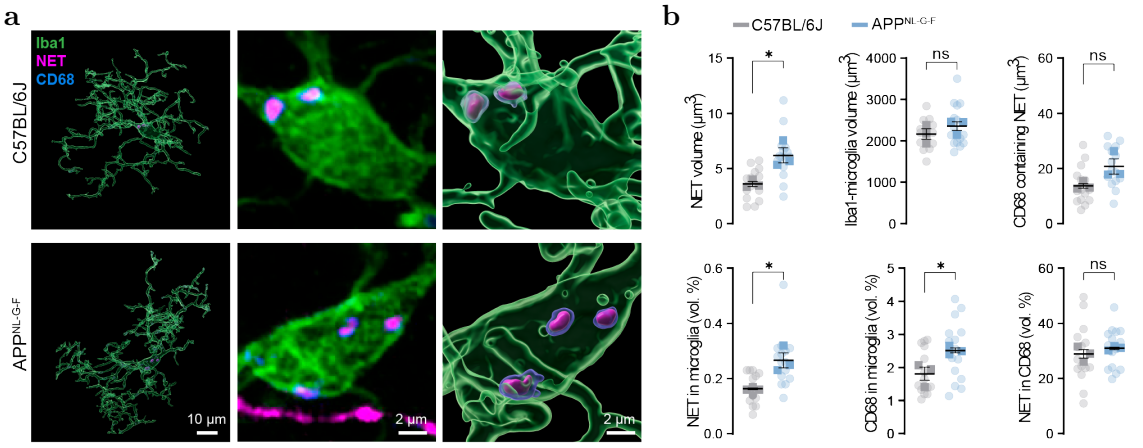

Figure 19: Increased APP^{NL-G-F} microglia phagocytosis of LC axons in the olfactory bulb
(a) Exemplary immunostaining and 3D reconstruction of microglia (Iba1, green), LC axons (NET, magenta) and lysosomes (CD68, blue) from a C57BL/6J and APP^{NL-G-F} animal. **(b)** In the upper row, quantification of the NET^{+} volume, Iba1^{+} volume and CD68^{+} volume containing NET. In the lower row, quantification of the percental volume of NET signal inside microglia, CD68 signal inside microglia and NET signal inside lysosomes (n = 3 mice per genotype, 5 cells per animal); Data are expressed as mean ± SEM; ns, not significant; *p<0.05.

3.4.2 APP^{NL-G-F} olfactory bulb microglia have increased phagocytotic activity

A remarkable heterogeneity of microglia has been revealed by proteomics and RNA sequencing in the APP^{NL-G-F} mouse model [167, 168]. Unfortunately though, these data were acquired by omitting the OB. Consequently, we set out to perform RNA sequencing and a phagocytosis assay of microglia isolated from OBs of WT and APP^{NL-G-F} mice at the age of 2 months to gain a closer insight into their profile.

Well in line with our immunohistology data, we observed an increased number of isolated microglia cells in the OB of APP^{NL-G-F} animals during quality control (WT: 252.688 ± 28.817, APP^{NL-G-F}: 344.625 ± 91.938; 36 % increase; data not shown here).

Bulk RNA sequencing revealed 2.344 significantly regulated genes, with a slight majority of them (1.283) being upregulated in APP^{NL-G-F} animals (Fig. 20a). Interestingly it has to be mentioned that most genes were significantly regulated in female mice only. In this list of genes, no common disease-associated microglia (DAM) signature genes, like

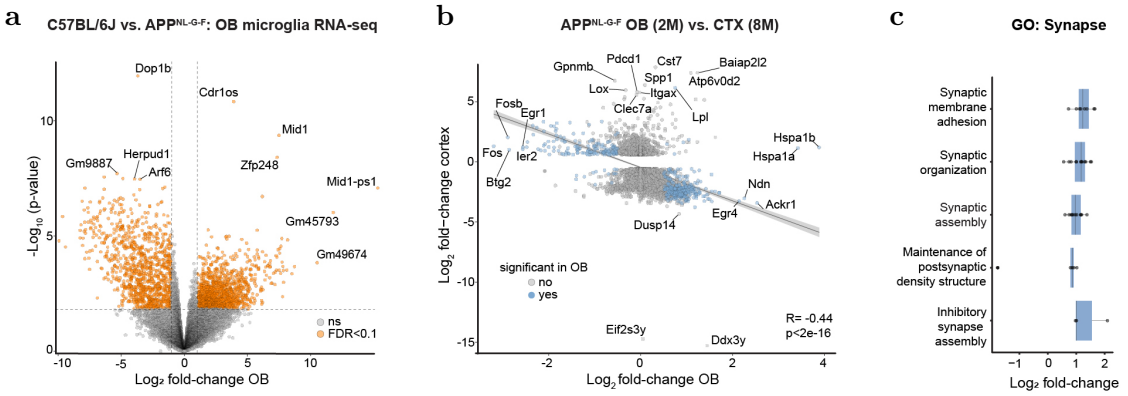

Figure 20: RNA sequencing of olfactory bulb microglia

(a) Volcano plot visualizing differentially expressed microglia genes (orange) in 2-month-old APP$^{\text{NL-G-F}}$ mice compared to C57BL/6J mice (n = 8 mice per genotype). **(b)** Volcano plot comparing microglia genes from the olfactory bulb of 2-month-old APP$^{\text{NL-G-F}}$ mice to the cortex of 8-month-old APP$^{\text{NL-G-F}}$ mice [167]. **(c)** Gene ontology (GO) enrichment analysis of genes involved in synapses.

TREM2, APOE4, CD33, ITGAX or BIN1 were found, indicating a physiological, healthy state of APP$^{\text{NL-G-F}}$ microglia. This was further proven by a direct comparison of our OB microglia RNA sequencing data set to a publicly available data set from 8-month-old cortical microglia from the same mouse line (Fig. 20b). Linear regression of log-fold changes in fact revealed a significant negative relationship (R = -0.44, P$<^{\text{2e-16}}$), suggesting that no such DAM response is seen in 2-month-old OB microglia. Gene ontology analysis revealed that the 20 most enriched terms relate to neuronal function and synaptic plasticity. Additionally, 73 genes related to the GO-term synapse were upregulated, suggesting increased synaptic pruning (Fig. 20c).

To support our RNA sequencing data of increased plasticity we performed a phagocytosis assay to measure the actual phagocytotic activity of cultures OB microglia. 2-month-old WT and APP$^{\text{NL-G-F}}$ microglia were harvested and cultured for 5 days. Then, cells were exposed to 2.5 μg/ml synaptosomes, coupled with pHrodo red and imaged over 24 hours. The pH-sentitive pHrodo dye has non to low fluorescent intensity at a neutral pH in the cell culture medium, but upon internalization in the cells lysosomes, the acidic milieu activates the fluorophore which can be captured by the microscope (Fig. 21a). Both WT

and $APP^{NL\text{-}G\text{-}F}$ microglia directly started to digest the added synaptosome substrate in an equal amount. After 5 hours, $APP^{NL\text{-}G\text{-}F}$ microglia started to phagocytose more than WT microglia. After 18 hours, WT microglia reached a plateau, whereas $APP^{NL\text{-}G\text{-}F}$ phagocytosis further increased (Fig. 21b). Next, we analysed the cells phagocytotic actitivty in more detail at the time point of 12 hours. Normalized to the microglia cell number, $APP^{NL\text{-}G\text{-}F}$ microglia phagocytosed 33 % more synaptosomes than WT microglia (WT: 100.0 % ± 6.96 %, $APP^{NL\text{-}G\text{-}F}$: 133.4 % ± 33.40 %). As a control, the phagocytotic activity was measured in the presence of cytochalasin D (Cyto D, 10 μM). Blocking phagocytosis with Cyto D showed a significant and equal downregulation of the fluorescent signal in both genotypes (Fig. 21c).

In addition to the application of synaptosomes we also added noradrenaline to the cells in order to investigate its effect on the phagocytic efficacy. 100 μM noradrenaline sped up phagocytosis in both genotypes equally. After 12 hours, microglia phagocytosed about 13 % more synaptosomes in the presence of noradrenaline, highlighting its importance for microglia function (Fig. 21d,e).

All together, our RNA sequencing data and the phygocytosis assay revealed $APP^{NL\text{-}G\text{-}F}$ olfactory bulb microglia to be in a healthy state, but to have an increased phagocytotic activity. This explains why we detect an elevated amount of NET^{+} protein inside microglia of $APP^{NL\text{-}G\text{-}F}$ mice.

3.4.3 Microglia sense compromised LC axons over phosphatidylserine-MFG-E8 signaling

Microglia sense molecular cues from damaged cells and actively migrate towards these structures for clearance in order to keep the microenvironment healthy. A variety of these cues, called 'find-me' and 'eat-me' signals, exists that are expressed by specific cell types. Accordingly, we aimed to work out which 'eat-me' signal labels LC axons in the OB for microglial phagocytosis. First, we considered C1q, which is known to tag inactive synapses in AD. C1q staining and reconstruction presented a dense punctuate signal in the OB with regular colocalization to NET fibers (Fig. 22a). However, comparing $APP^{NL\text{-}G\text{-}F}$ mice to WT mice and after normalizing to the NET fiber density, we did not detect

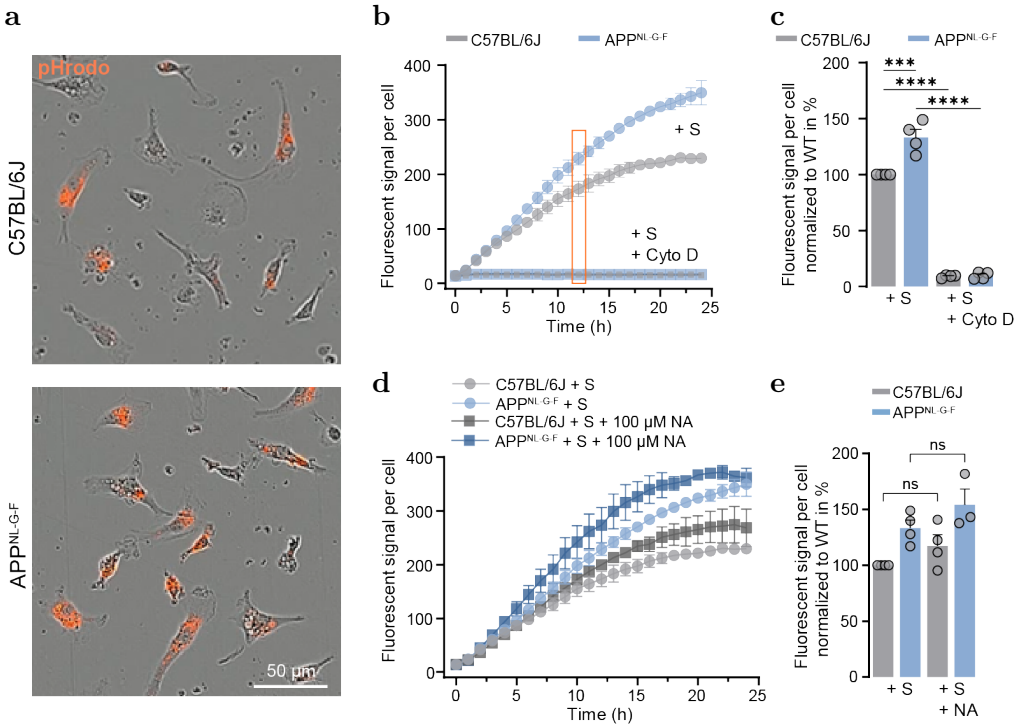

Figure 21: APP^{NL-G-F} microglia have an increased phagocytotic activity

(a) Microglia cell pictures taken with the Incucyte live-cell analysis system after 12 hours incubation with synaptosomes (pHrodo, orange). **(b)** pHrodo fluorescent signal per cell over 24 hours comparing the phagocytotic activity of C57BL/6J and APP^{NL-G-F} microglia. **(c)** Fluorescent signal per cell normalized to C57BL/6J at the time point 12 hours shows APP^{NL-G-F} microglia to phagocytose more synaptosomes than C57BL/6J microglia. Cytochalasin-D (CytoD) application inhibited phagocytosis (n = 4 mice per genotype, 3 replicates). **(d)** PHrodo fluorescent signal per cell over 24 hours comparing the phagocytotic activity of C57BL/6J and APP^{NL-G-F} microglia with and without additional noradrenaline application. **(e)** Fluorescent signal per cell normalized to C57BL/6J at the time point 12 hours shows that noradrenaline elevates the phagocytotic activity of microglia in both genotypes.; Data are expressed as mean ± SEM; ***p<0.001, ****p<0.0001.

any significant differences in the C1q signal colocalized to the fibers (Fig. 22b). Next, we checked for the 'eat-me' signal phosphatidylserine (PS) which was shown to mediate synaptic removal of newborn neurons especially in the OB region. Therefore, the OB of 5-month-old WT and APP^{NL-G-F} animals was injected with the dye PSVue550, which labels externalized PS on the membrane of compromised cells. 1 hour post injection, mice were perfused and OBs stained (Fig. 22c). PS punctuate was observed in both genotypes. 3D reconstruction and a colocalization analysis revealed an increased PS volume on NET

fibers of $APP^{NL\text{-}G\text{-}F}$ (Fig. 22c,d). Notably, we often found microglia in direct contact to externalized PS. This led us to probe, whether microglia have more contact points to NET fibers of $APP^{NL\text{-}G\text{-}F}$ mice than in WT mice. When analyzing the contact points and normalizing to the NET fiber density, no difference between the genotypes was observed, though (Fig. 22e,f). To further confirm our findings, we thought to detect the microglia receptor that recognizes the exposed PS on NET fibers. A plethora of receptors and adaptor proteins is known to bind to PS, such as MFG-E8 which is involved in synaptic pruning during adult neurogenesis in the OB. Staining and reconstruction of the MFG-E8 signal and NET fibers showed more MFG-E8 colocalized to LC axons of $APP^{NL\text{-}G\text{-}F}$ than on LC axons of WT animals (Fig. 22g,h). Additionally, a triple staining together with PS finally revealed that PS externalized on NET fibers is capped with MFG-E8 (Fig. 22i). Taken together, we could show that microglia sense and clear compromised LC axons in the OB over PS-MFG-E8 signaling.

3.4.4 Intracellular Aβ plays a role in driving LC axon damage

What is the reason for LC axon damage and consequently its loss?
Firstly, we checked if $APP^{NL\text{-}G\text{-}F}$ mice experience LC neuron loss. Therefore, we counted LC neurons from $APP^{NL\text{-}G\text{-}F}$ and WT animals at 12 months of age, but we could not detect a difference in their cell numbers (Fig. 23a,b). Secondly, we asked if the Aβ pathology might correlate with LC axon degeneration. In the LC region itself almost no Aβ-plaques were present. In the olfactory bulb, the formation of extracellular Aβ-plaques and the first loss of LC axons both started at 2 months of age. We correlated the density of Aβ-plaques with the LC axon loss for every picture per animal at 6 months of age, but they were independent from each other (Fig. 23c). Moreover, looking at other brain regions, like the hippocampus and piriform cortex in which the Aβ pathology is much stronger at young age, no NET fiber degeneration was observed (Fig. 11b). Hence, one can exclude extracellular Aβ to trigger LC axon degeneration.
Since not only extracellular Aβ, but also intracellular Aβ is toxic for neurons, we investigated intracellular Aβ to play a role in driving LC axon damage. Using the antibody WO-2 which stains the APP amino acids 4 and 10 we found LC neuron somata of 2-month-old $APP^{NL\text{-}G\text{-}F}$ mice to be loaded with intraneuronal Aβ in comparison to WT animals.

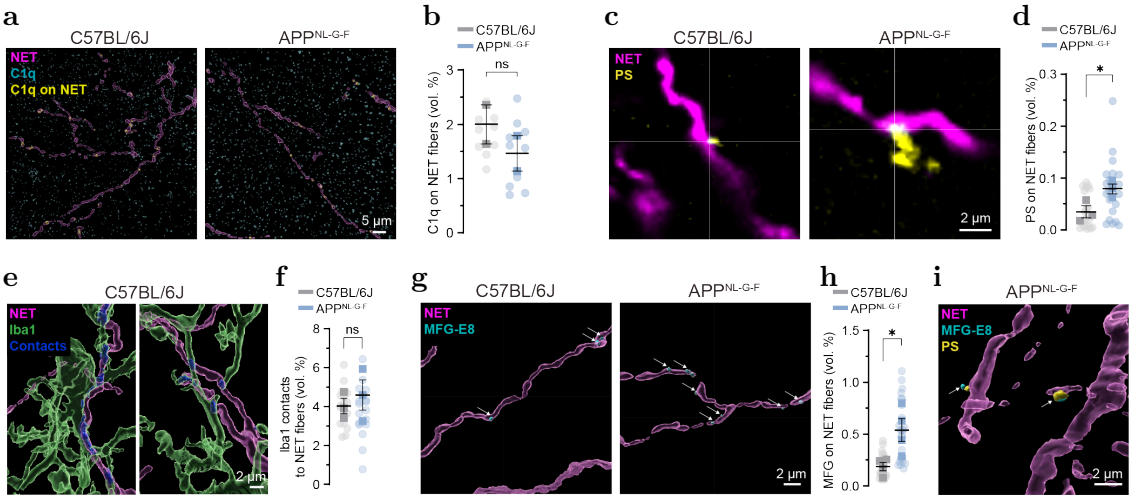

Figure 22: Phosphatidylserine (PS) and MFG-E8 decorate LC axons for microglia clearance **(a)** Immunostaining and reconstruction of LC axons (NET, magenta) and C1q (cyan). **(b)** Quantification of C1q signal colocalized to NET fibers. NET fibers are tagged with the 'eat-me' signal C1q but no difference between the groups was observed (n = 2 mice per group, 5 pictures per animal). **(c)** Immunostaining visualizing phosphatidylserine (PS, yellow) on LC axons (NET, magenta). **(d)** PS decorates NET fibers from $APP^{NL\text{-}G\text{-}F}$ mice in a higher proportion than NET fibers from C57BL/6J mice (n = 3 mice per group, 6 pictures per animal). **(e)** Contact points between microglia (Iba1, green) and NET fibers (NET, magenta) **(f)** Analysis of contact points shows the same amount of volume beeing colocalised between the groups (n = 3 mice per group, 6 pictures per animal). **(g)** 3D reconstruction of MFG-E8 adaptor protein (MFG-E8, cyan) colocalised to LC axons (NET, magenta). **(h)** Significantly more MFG-E8 was present on $APP^{NL\text{-}G\text{-}F}$ axons (n = 3 mice per group, 6 pictures per animal). **(i)** Tripple staining of LC axons (NET, magenta), PS (yellow) and MFG-E8 (cyan) shows that PS is externalized on NET fibers and capped by MFG-E8; Data are expressed as mean ± SEM; ns, not significant; *p<0.05.

At 6 months of age, the amount of intraneuronal Aβ was reduced again, pointing to an anterograde transport of intraneuronal Aβ (Fig. 23d,e).

Overall, we suggest intraneuronal Aβ to be taken into account as a driver of LC neuron hyperactivity and thereby to the induction of LC axon degeneration.

3.4.5 Tau induces mild degeneration of LC axons in the olfactory bulb

The $APP^{NL\text{-}G\text{-}F}$ mouse model only reflects the aspects of Aβ pathology involved in AD, but does not consider Tau. In order to address this issue we crossed heterozygous $APP^{NL\text{-}G\text{-}F}$ mice to heterozygous hTau mice.

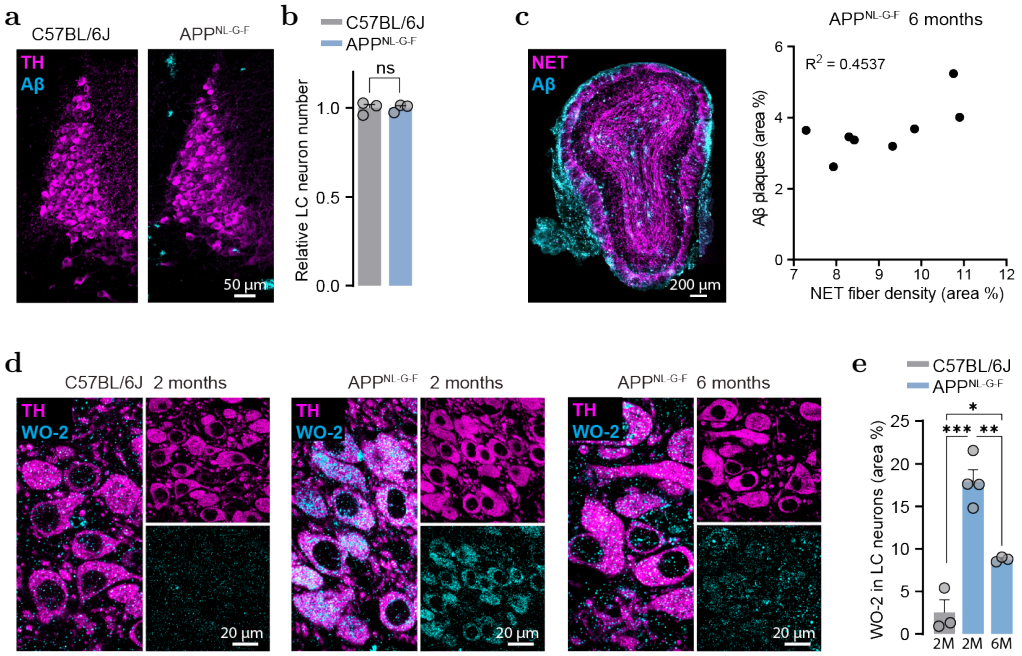

Figure 23: LC axon loss correlates with intraneuronal Aβ and not extracellular Aβ plaques **(a)** Representative confocal images of LC neurons (TH, magenta) and Aβ-plaques (cyan). **(b)** Relative LC neuron number in 12-month-old C57BL/6J and APP$^{NL\text{-}G\text{-}F}$ mice (n = 3 mice per group, 8 pictures per animal). **(c)** Correlation between NET fiber density and Aβ-plaque load in the OB of APP$^{NL\text{-}G\text{-}F}$ mice at 6 months of age (n = 8 mice per group, 4 pictures per animal). **(d)** Immunostaining against LC neurons (TH, magenta) and intraneuronal Aβ (WO-2, cyan) in a 2-month-old C57BL/6J animal and in a 2- and 6-month-old APP$^{NL\text{-}G\text{-}F}$ animal. **(e)** Quantification of WO-2 signal inside LC neurons reveals a high signal in 2-month-old APP$^{NL\text{-}G\text{-}F}$ mice that decreases at 6 months of age (n = 3-4 mice per group, 5 pictures per animal); Data are expressed as mean ± SEM; ns, not significant; *p<0.05, **p<0.01, ***p<0.001.

First, we analyzed LC axons in heterozygous APP$^{NL\text{-}G\text{-}F}$ mice at 6 months of age. No difference in NET fiber density was observed in those mice compared to WT mice. However, crossing in heterozygous hTau, reduced LC axons in the OB by approximately 16 %, showing that Tau induces LC axon degeneration, even though not to the same extent as Aβ in homozygous APP$^{NL\text{-}G\text{-}F}$ mice and not significantly different compared to WT and heterozygous APP$^{NL\text{-}G\text{-}F}$ mice (Fig. 24a,b).

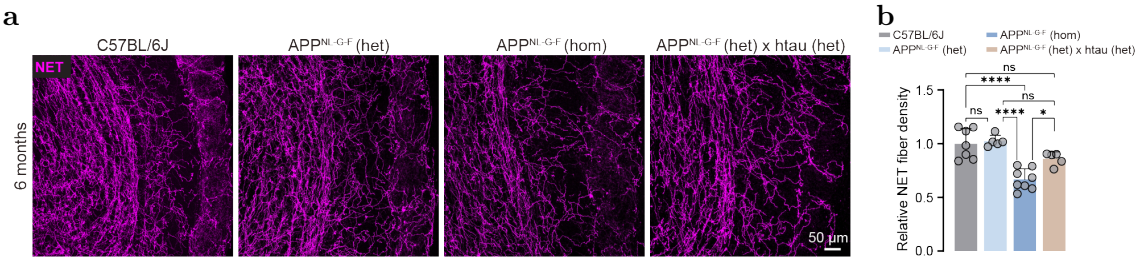

Figure 24: Human Tau induces mild LC axon loss in heterozygous APP$^{NL\text{-}G\text{-}F}$ mice
(a) Immunostaining visualizing LC axons (NET, magenta) in the olfactory bulb of 6-month-old C57BL/6J, heterozygous APP$^{NL\text{-}G\text{-}F}$, homozygous APP$^{NL\text{-}G\text{-}F}$ and heterozygous APP$^{NL\text{-}G\text{-}F}$ × heterozygous hTau mice. **(b)** Quantification of relative LC axon density per genotype (n = 5-8 mice per group, 4 pictures per animal); Data are expressed as mean ± SEM; ns, not significant; *p<0.05, ****p<0.0001.

3.5 Modulation of microglia function by deletion of TSPO abolishes LC axon loss and prevents olfactory dysfunction

3.5.1 TSPO-PET scans in APP$^{NL\text{-}G\text{-}F}$ mice show an increased number/activity of microglia in the olfactory bulb

Early microgliosis is a hallmark of APP$^{NL\text{-}G\text{-}F}$ animals as we have demonstrated in our immunohistochemical analysis (section 3.2.1, Fig. 12). PET scans with the tracer TSPO ([18]F-GE180), allow to observe microgliosis throughout the brain and they have the advantage to image the progression longitudinally. 16 female WT mice and 11 female APP$^{NL\text{-}G\text{-}F}$ mice were imaged between 2 and 12 months of age (Fig. 25a). In the OB, a 10 % increase in TSPO-SUVr signal was observed as early as 2-3 months of age, comparing APP$^{NL\text{-}G\text{-}F}$ to age matched WT animals (APP$^{NL\text{-}G\text{-}F}$: 0.227 SUVr ± 0.200 SUVr, WT: 0.207 SUVr ± 0.008 SUVr). With increasing age, the OB-TSPO signal increased steadily in APP$^{NL\text{-}G\text{-}F}$ mice and peaked with an 18 % increment at 12 months of age, while it remained unaffected in WT mice (R^2 = 0.2021 and R^2 = 0.0041) (Fig. 25b,c). As a comparison region, we chose to analyse the cortex, as this region shows a strong Aβ plaque deposition early on. Strikingly, at 2-3 months of age no difference in TSPO-SUVr signal was detected (0.1819 SUVr ± 0.0082 SUVr to 0.1826 SUVr ± 0.00065 SUVr). Only at 6 months of age, an increase in cortical TSPO signal was measured which then rapidly

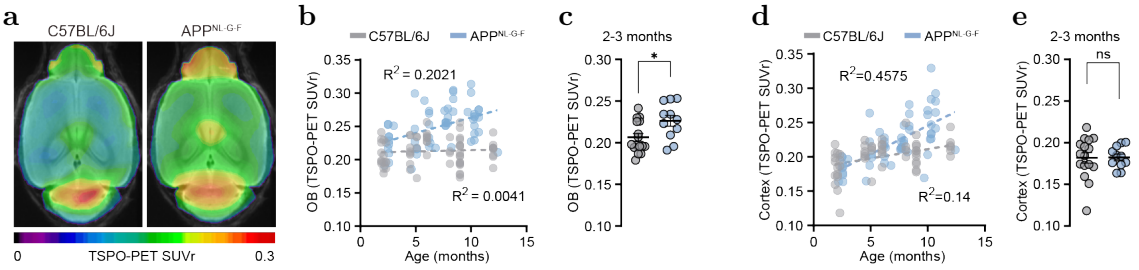

Figure 25: Elevated TSPO-PET signal in the olfactory bulb of young APP$^{NL\text{-}G\text{-}F}$ mice
(a) Small-animal TSPO-µPET in C57BL/6J and APP$^{NL\text{-}G\text{-}F}$ mice, horizontal plane through the brain at 3 months of age. **(b)** TSPO-PET signal in the OB, longitudinally measured from 2 to 12 months of age (n = 66 vs. 55 mice). **(c)** At 2-3 months of age, APP$^{NL\text{-}G\text{-}F}$ mice have a higher TSPO signal in the OB than C57BL/6J mice, while **(d,e)** in the cortex no difference in TSPO signal was observed (n = 16 vs. 11 mice); Data are expressed as mean ± SEM; not significant; *p<0.05.

further increased up to 22 % at 12 months of age (Fig. 25d,e). Comparing the slopes of increment, cortical TSPO increased faster (R^2 = 0.4574) than OB-TSPO (R^2 = 0.2021). However, the baseline TSPO signal in the OB is higher from the beginning on and peaks at the same level as cortical TSPO-SUVr.
Overall, TSPO-PET scans revealed an early increase in the number/activity of microglia in the OB that seems to be independent of Aβ-plaques.

3.5.2 Reduced microglial phagocytosis abolishes LC axons loss and prevents olfactory decline

Having uncovered microglial phagocytosis as the underlying mechanism of LC axon removal, we asked whether reducing phagocytosis could prevent LC axon loss in the OB. Microglial TSPO has recently been identified as a key-protein in fueling phagocytosis. Thus, we hypothesized that TSPO deletion and consequently decreased phagocytosis might be sufficient to prevent LC axon degeneration. Quantification of the NET fiber density in APP$^{NL\text{-}G\text{-}F}$ × TSPO-KO mice indeed revealed an almost complete abolishment of LC axon loss up to an age of 6 months. At 12 months of age, LC axons degenerate, even though not as much as in APP$^{NL\text{-}G\text{-}F}$ mice (Fig. 26a,b).
Importantly we checked next whether the reduced LC axons loss would result in restored

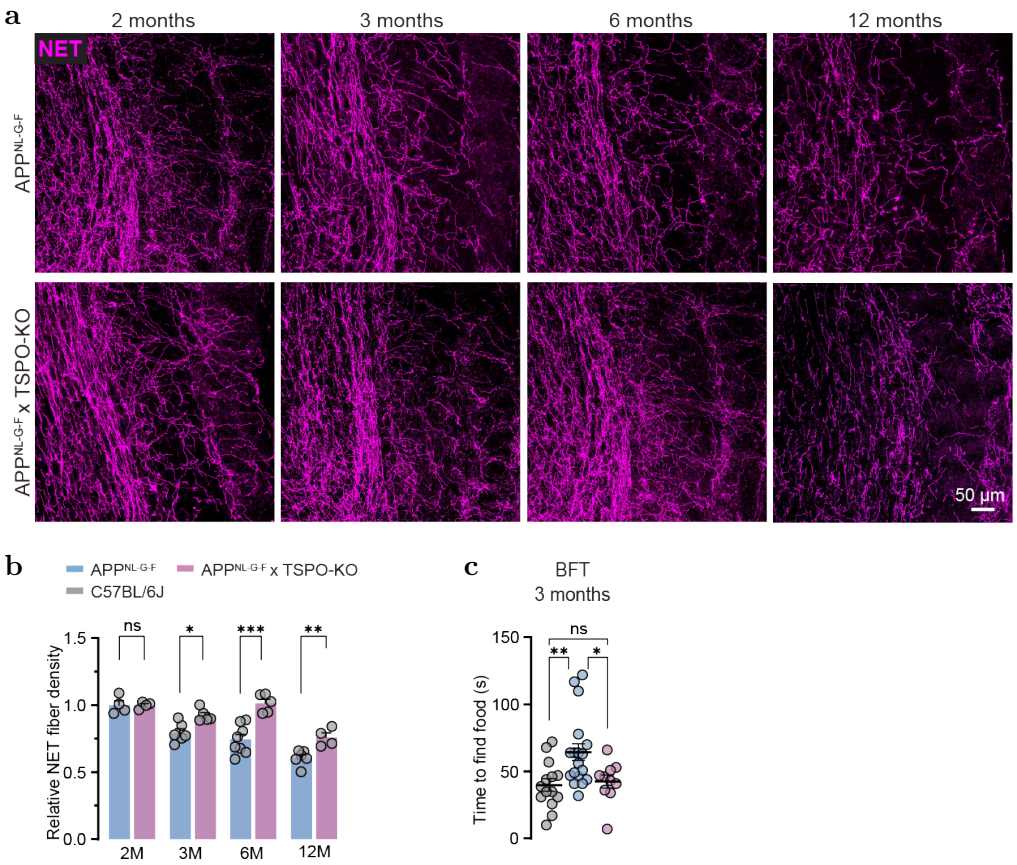

Figure 26: APP$^{NL\text{-}G\text{-}F}$ × TSPO-KO mice have no LC axon loss and normal olfaction

(a) Representative pictures of an immunofluorescent stain against NET (magenta), comparing the LC axon density in the OB of APP$^{NL\text{-}G\text{-}F}$ and APP$^{NL\text{-}G\text{-}F}$ × TSPO-KO mice. **(b)** APP$^{NL\text{-}G\text{-}F}$ × TSPO-KO mice have more NET fibers than APP$^{NL\text{-}G\text{-}F}$ mice (n = 4-8 mice per group, 4 pictures per animal). **(c)** Buried food test performed with 3-month-old animals shows no olfactory decline in APP$^{NL\text{-}G\text{-}F}$ × TSPO-KO mice (n = 10-18 mice per group); Data are expressed as mean ± SEM; ns, not significant; *p<0.05, **p<0.01, ***p<0.001.

olfaction of these animals. Therefore, 3-month-old APP$^{NL\text{-}G\text{-}F}$ × TSPO-KO mice underwent the buried food test. Indeed, the animals found the hidden food pellet faster than APP$^{NL\text{-}G\text{-}F}$ mice, almost in the same time than WT mice (APP$^{NL\text{-}G\text{-}F}$ × TSPO-KO: 42.40 s, APP$^{NL\text{-}G\text{-}F}$: 64.39 s, C57BL/6J: 39.86 s; Fig. 26c).

3.5.3 APP^{NL-G-F} × TSPO-KO LC axons are decorated with MFG-E8 but get phagocytosed less

Our last experiment clearly pinpointed microglial phagocytosis to be the underlying cause of the progressive LC axon loss in the olfactory bulb and demonstrated that the preservation of LC axons by knock-down of phagocytosis restores olfaction. To further confirm our findings we carried out an immunostaining with subsequent 3D reconstruction of NET protein inside the lysosomes of microglia in APP^{NL-G-F} × TSPO-KO mice at 3 months of age (Fig. 27a). The percental volume of NET^{+} protein inside microglia was significantly reduced in APP^{NL-G-F} × TSPO-KO mice compared to APP^{NL-G-F} mice, while no change in microglia volume and CD68 volume was observed (Fig. 27b). Having previously found, that LC axons are decorated with MFG-E8 for microglial recognition and phagocytosis we asked next if less of the MFG-E8 signal is present on the fibers of APP^{NL-G-F} × TSPO-KO mice. Staining and reconstruction of the signal, however, revealed a high amount of MFG-E8 colocalized to NET fibers that is even slightly higher than in APP^{NL-G-F} mice (Fig. 26c,d).

In summary, we hypothesize that LC axons in APP^{NL-G-F} × TSPO-KO animals are still internally impaired and get tagged with the 'eat-me' signals PS and MFG-E8 for microglia clearance but they cannot be phagocytosed and therefore persist, even distributing enough noradrenaline for a normal functioning of the olfactory sense.

3.6 Noradrenergic dysfunction alone is sufficient to replicate key findings observed in the APP^{NL-G-F} mouse model

3.6.1 Cholinergic and serotonergic system in the olfactory bulb is not affected

Since not only the noradrenergic system is involved in shaping olfaction, we set out to check other neurotransmitter systems in the OB. Cholinergic and serotonergic axons mainly innervate the glomerular and granular cell layer of the OB and distribute the neurotransmitter acetylcholine and serotonin to interneurons, thereby shaping the specificity of olfactory

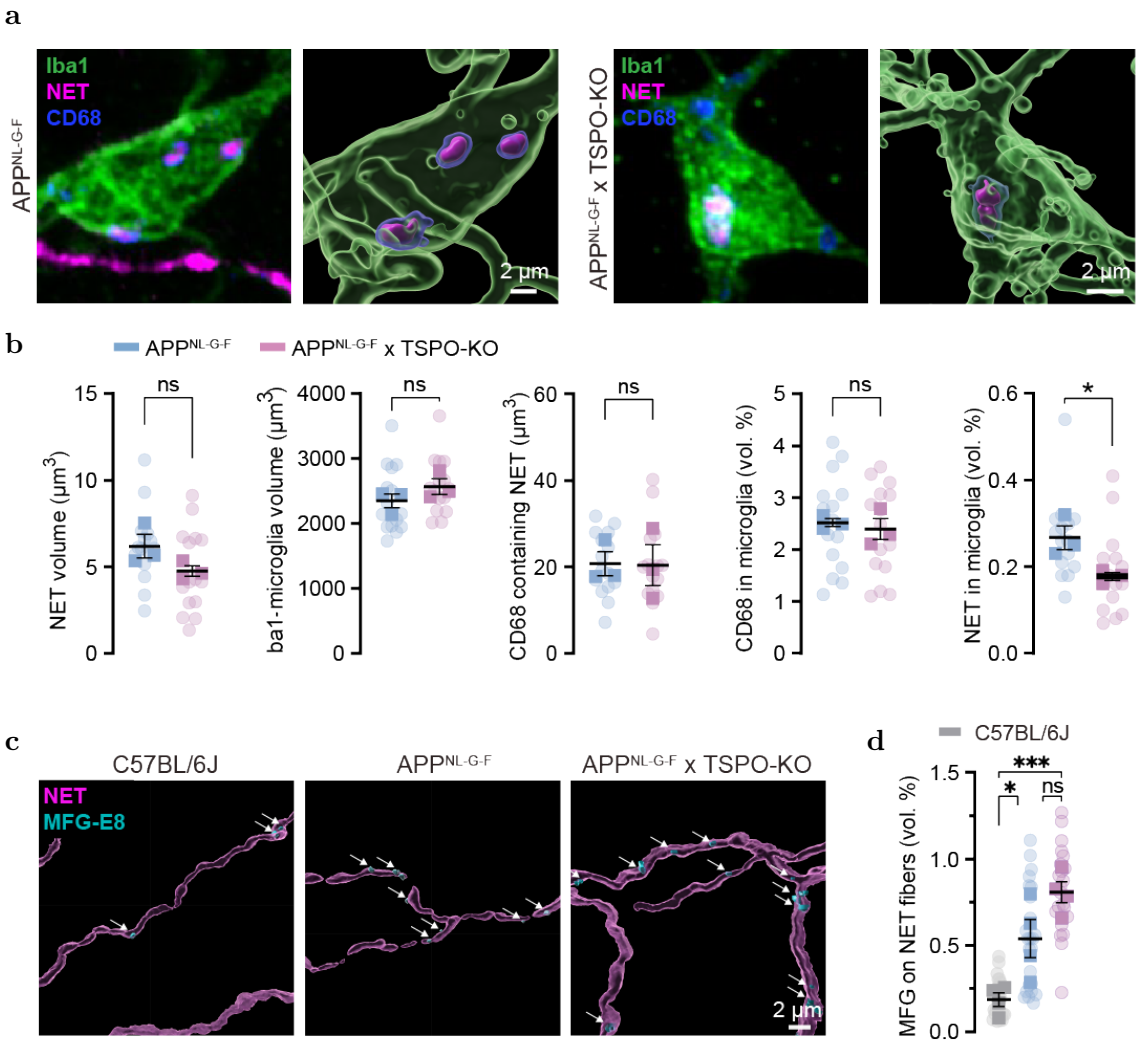

Figure 27: APP^{NL-G-F} × TSPO-KO LC axons get phagocytosed less, even though being decorated with MFG-E8

(a) Immunostaining and 3D reconstruction of microglia (Iba1, green), LC axons (NET, magenta) and lysosomes (CD68, blue) from a APP^{NL-G-F} and APP^{NL-G-F} × TSPO-KO animal. **(b)** Quantification of the NET^{+} volume, Iba1^{+} volume and CD68^{+} volume containing NET as well as quantification of the percental volume of CD68 inside microglia and NET inside microglia (n = 3 mice per group, 5 pictures per animal). **(c)** 3D reconstruction of MFG-E8 (MFG-E8, cyan) colocalised to LC axons (NET, magenta). **(d)** Significantly more MFG-E8 is present on the LC axons of APP^{NL-G-F} and APP^{NL-G-F} × TSPO-KO mice in comparison to C57BL/6J mice (n = 3 mice per group, 6 pictures per animal); Data are expressed as mean ± SEM; ns, not significant; *p<0.05, ***p<0.001.

responses. We immunohistochemically labeled cholinergic axons with the marker Choline Acetyltransferase (ChAT) and serotonergic axons with a serotonin transporter antibody

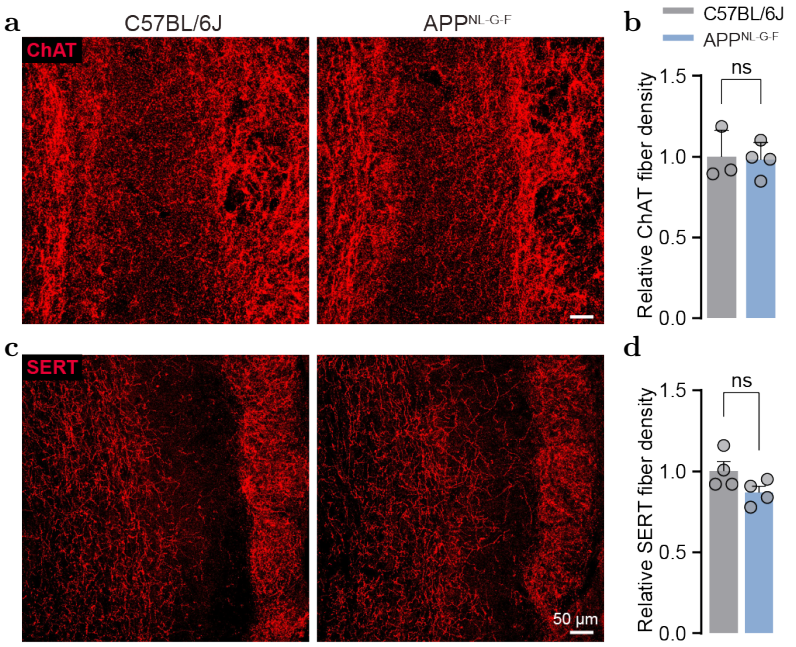

Figure 28: Cholinergic and serotonergic axons in the olfactory bulb persist

(a) Representative pictures of an immunofluorescent stain against ChAT (red), comparing the cholinergic axon density in the OB of C57BL/6J and APP^{NL-G-F} mice at 3 months of age. **(b)** Quantification of the ChAT axon density (n = 3-4 mice per group, 3 pictures per animal) **(c)** Representative pictures of an immunofluorescent stain against SERT (red), comparing the serotonergic axon density in the OB of C57BL/6J and APP^{NL-G-F} mice at 3 months of age. **(d)** Quantification of the SERT axon density (n = 4 mice per group, 3 pictures per animal); Data are expressed as mean ± SEM; ns, not significant.

(SERT). A comparison between 3-month-old WT and APP^{NL-G-F} animals showed no difference in cholinergic axons density (Fig. 28a,b), whereas serotonergic terminals show a trend to be reduced, however not significant (Fig. 28c,d).

3.6.2 LC specific AAV-hAPP^{NL-G-F} expression causes LC axon loss, increases microglial phagocytosis and induces olfactory impairment

The APP^{NL-G-F} mouse model is characterized by the expression of three familiar AD mutations in every APP positive cell, causing an elevated level of pathogenic Aβ [14]. This fact raises the question how specific the LC axons loss in the OB is. To this end, we wanted to

test whether $APP^{NL\text{-}G\text{-}F}$ expression in the LC alone might be sufficient to recapitulate our histological and behavioral findings. Thus, we engineered a custom-built Cre-dependent virus (Fig. 29a) to transduce LC neurons of healthy Dbh mice with the human $APP^{NL\text{-}G\text{-}F}$ mutations (Dbh-$hAPP^{NL\text{-}G\text{-}F}$) and injected another cohort with a control virus leading to the expression of a fluophore only (Dbh-EYFP) (Fig. 29b,c). 3 months post injection, an immunohistochemical validation revealed a sufficient transduction of LC neurons without neuron loss (Dbh-$hAPP^{NL\text{-}G\text{-}F}$: 34 %, Dbh-EYFP: 89 %; Fig. 28c,d). In the OB of Dbh-$hAPP^{NL\text{-}G\text{-}F}$ mice we observed LC axon degeneration of 15 % compared to Dbh-EYFP mice (Fig. 29g,h). 3D reconstruction of NET^{+} protein in lysosomes of microglia showed Dbh-$hAPP^{NL\text{-}G\text{-}F}$ microglia to phagocytose more, as they had an increased CD68 volume compared to Dbh-EYFP. Moreover, Dbh-$hAPP^{NL\text{-}G\text{-}F}$, like $APP^{NL\text{-}G\text{-}F}$ mice had an increased amount of NET^{+} protein inside microglia which explains the NET fiber loss in these animals (Fig. 29e,f). At 5 months of age, we also performed a buried food test. Dbh-EYFP control mice found the food pellet in 36.20 s ± 12.87 s, a comparable time WT animals at the age of 3 months needed to find the food pellet. Dbh-$hAPP^{NL\text{-}G\text{-}F}$ mice needed significantly more time than Dbh-EYP mice, namely 130.40 s ± 94.20 s (Fig. 29i). Comparing this time to $APP^{NL\text{-}G\text{-}F}$ mice at the age of 3 month, Dbh-$hAPP^{NL\text{-}G\text{-}F}$ take 50 % longer to find the food pellet, even though less NET fibers, only 15 % instead of 33 % are lost. When correlating the NET fiber density with the time to find the food pellet a strong negative correlation was observed. Dbh-EYFP mice which have a high NET fiber density, find the food pellet quickly, while on the other hand Dbh-$hAPP^{NL\text{-}G\text{-}F}$ mice have a low NET fiber density and need a long time to find the hidden food pellet (Fig. 29j).
In summary, our approach to induce Dbh-$hAPP^{NL\text{-}G\text{-}F}$ pathology in LC neurons explicitly reveals that the expression is indeed sufficient to recapitulate olfactory bulb specific aspects as observed in the $APP^{NL\text{-}G\text{-}F}$ mouse line.

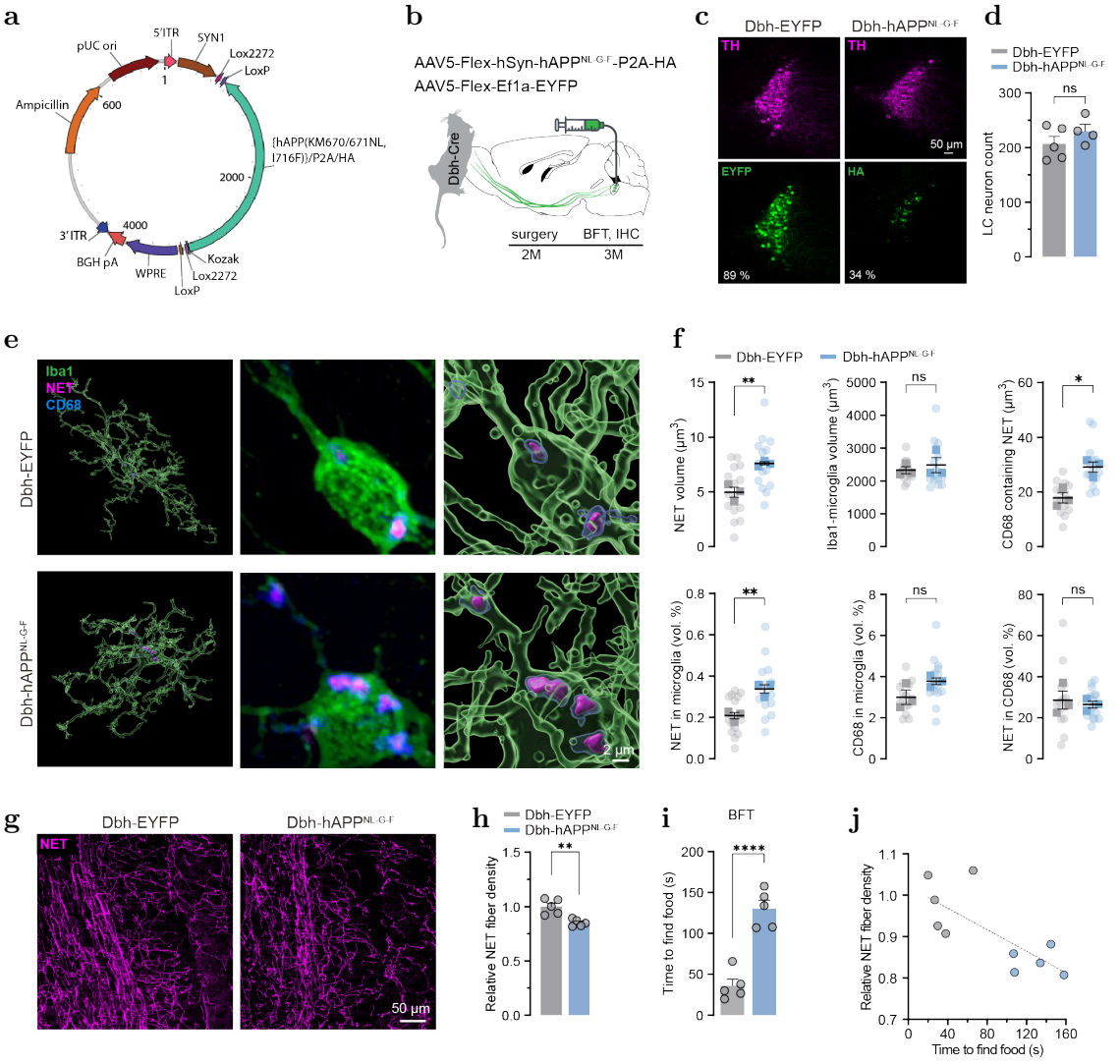

Figure 29: LC specific AAV-hAPP$^{NL\text{-}G\text{-}F}$ expression causes LC axon loss, increases microglial phagocytosis and induces olfactory impairment

(a) AAV-hAPP$^{NL\text{-}G\text{-}F}$ virus construct. **(b)** Experimental setup of virus injection and subsequent experiments (n = 5 mice per group). **(c)** Immunostaining of LC neurons (TH, magenta) and the respective fluorophore expression of each virus (Dbh-EYFP: EYFP and Dbh-hAPP$^{NL\text{-}G\text{-}F}$: HA-tag). **(d)** LC neuron count (n = 5 vs. 4 mice). **(e)** Immunostaining and 3D reconstruction of microglia (Iba1, green), lysosomes (CD68, blue) and LC axons (NET, magenta). **(f)** In the upper row, quantification of the NET$^+$ volume, Iba1$^+$ volume and CD68$^+$ volume containing NET. In the lower row, quantification of the percental volume of NET signal inside microglia, CD68 signal inside microglia and NET signal inside lysosomes (n = 3 mice per group, 5 pictures per animal). **(g)** Immunostain against LC fibers (NET, magenta) in the olfactory bulb. **(h)** Quantification of NET fiber density (n = 5 mice per group, 4 pictures per animal). **(i)** Buried food test (n = 5 mice per group). **(j)** Correlation between the NET fiber density and the time to find the buried food; Data are expressed as mean ± SEM; ns, not significant; *p<0.05, **p<0.01, ****p<0.0001.

3.7 Translational approach: Olfactory bulb LC axon loss and hyposmia serve as early biomarkers of AD in humans

3.7.1 Post-mortem tissue analysis of prodromal AD patients reveals LC axon loss in the olfactory bulb

Translating our histological finding from the $APP^{NL\text{-}G\text{-}F}$ mouse line to humans, we set out to decipher whether LC axon loss can be recapitulated in post-mortem olfactory bulb tissue of prodromal AD patients. To test this, olfactory bulb tissue from 7 healthy patients, 6 prodromal AD patients and 6 AD patients was provided from the Munich brain bank. Patients had mixed gender in all groups and an age range between 60-90 years (Table 3). The disease stage of the brain was assessed based on an immunostaining against Aβ (Thal phase) and Tau (Braak stage) in the frontal cortex. Tissue was classified as prodromal AD when the Thal phase and Braak stage was ranging between 1-3. AD was diagnosed when Thal phase and Braak stage 3-5 was reached. Aβ and Tau load in the olfactory bulb varied a lot between the patients and groups (Fig. 30d). Staining the OB tissue from prodromal AD cases for LC axons with the NET antibody revealed a pronounced NET fiber degeneration of 60 % compared to healthy controls (HC: 6.867 area %, pAD: 2.723 area %). Interestingly, no significant further reduction in NET fiber density was observed when looking at late stage AD tissue (pAD: 2.723 area %, AD: 2.378 area %; Fig. 30a-c).

3.7.2 Prodromal AD patients have an elevated TSPO-PET signal in the olfactory bulb and show signs of hyposmia

We hypothesized that the OB LC axon loss in prodromal AD patients may correlate with an increased number of microglia, as detected in the $APP^{NL\text{-}G\text{-}F}$ mouse model by PET scans and immunohistochemistry. Additionally, we though to investigate whether these patients experience olfactory difficulties. With the help of clinicians from the hospital Munich, department of Nuclear Medicine and Psychiatry/Psychotherapy, we carried out TSPO-PET scans in 17 prodromal AD cases, subjects with subjective cognitive decline (SCD) and mild cognitive impairment (MCI), 16 diagnosed Alzehimer's diseases patients

Table 3: Demographic details of subjects donating brain tissue

Brain tissue was donated from the Munich brain bank. Abbreviations: pAD = Prodromal Alzheimer's disease, AD = Alzheimer's disease, ARS = Arteriosclerosis, SVD = Small vessel disease, AgD = Argyrophilic grain disease, ARTAG = Aging-related tau astrogliopathy, CAA = Cerebral amyloid angiopathy

Patient	Diagnosis	Age (years)	Gender	Thal-phase	Braak-stage	Neuropathological diagnosis
1	Control	60	F	0	1	No significant abnormalities
2	Control	82	M	0	2	No significant abnormalities, ARS
3	Control	62	M	0	1	No significant abnormalities, ARS
4	Control	63	F	0	1	No significant abnormalities
5	Control	81	F	0	1	No significant abnormalities
6	Control	64	F	0	1	No significant abnormalities, ARS, mild SVD
7	Control	65	M	0	1	No significant abnormalities
8	pAD	73	M	2	1	Aβ and Tau accumulation
9	pAD	81	F	2	1	Aβ and Tau accumulation
10	pAD	87	-	2	3	Aβ and Tau accumulation, AgD
11	pAD	84	M	1	3	Aβ and Tau accumulation, ARTAG
12	pAD	86	M	2	3	Aβ and Tau accumulation, olivo-ponto-cerebellar dysplasia
13	pAD	67	M	3	1	Aβ and Tau accumulation, infarction, ischemic
14	AD	88	F	5	4	Aβ and Tau accumulation, meningeom
15	AD	90	F	4	3	Aβ and Tau accumulation, loss of mylein in spinal tract
16	AD	75	F	5	4	Aβ and Tau accumulation, CAA
17	AD	73	F	5	2	Aβ and Tau accumulation, ARS
18	AD	90	F	4	3	Aβ and Tau accumulation, AgD, CAA, hippocampal sclerosis
19	AD	78	M	4	4	Aβ and Tau accumulation, CAA, ARS

and 14 cognitively normal patients (Fig. 31a). Diagnosis was based on Tau and Aβ levels measured in the cerebro spinal fluid (Table 4). PET scans identified a significant elevated TSPO signal in the OB of prodromal AD patients compared to healthy patients (pAD: 1.003 SUVr ± 0.077 SUVr, HC: 0.9255 SUVr ± 0.019SUVr), indicative for an enrichment or higher activation of microglia. In diagnosed AD patients, the TSPO signal did not increase much further than in pAD patients (Fig. 31b). After the PET scan, patients got an examination of their sense of smell in order to analyze, whether already prodromal AD patients show signs of hyposmia. Performing standard-olfactory tests, in which patients

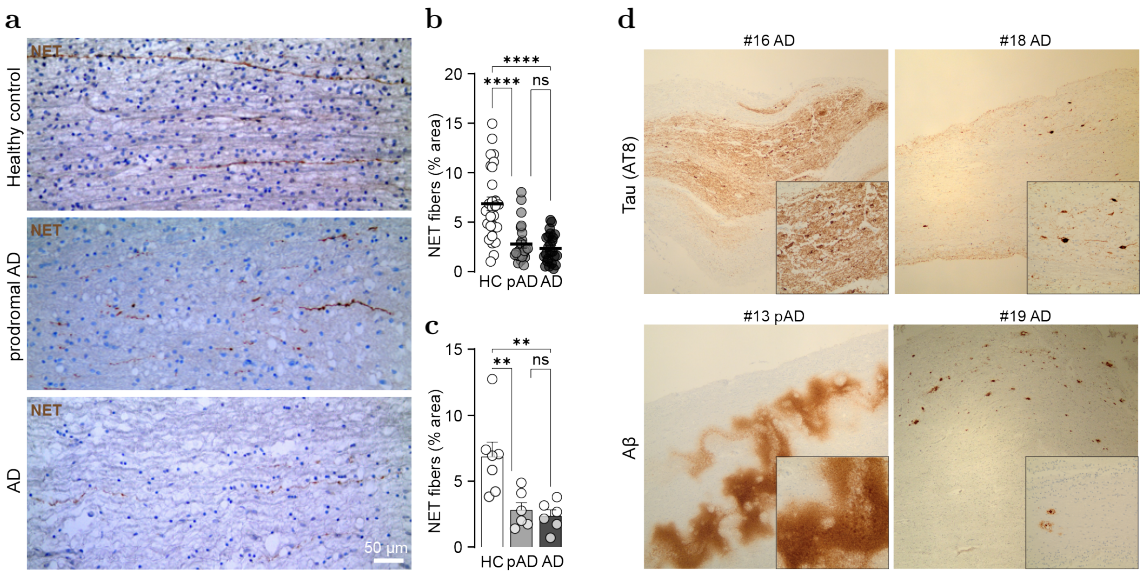

Figure 30: LC axon degeneration in human olfactory bulb tissue of AD patients

(a) Brightfield images of human OB tissue stained against NET (brown), comparing LC axon density in healthy patients (HC), patients with prodromal AD (pAD) and AD patients (AD). **(b)** Percental NET fiber area per image (4 images per sample, 1 sample per patient). **(c)** Percental NET fiber area per patient (HC n = 7, pAD n = 6, AD n = 6). Prodromal AD and AD patients show a strong decline in LC axon density. **(d)** Representative images of a Tau and Aβ stain in the olfactory bulb of different AD patients. Both Tau and Aβ were detected in different OB layers and expressed to different extents; Data are expressed as mean ± SEM; ns, not significant; **p<0.01, ****p<0.0001

needed to identify commonly known odors, revealed only a slight trend of decreased olfaction from 82.14 % correct identification score in healthy patients to 78.47 % in pAD. However, diagnosed AD patients showed strong olfactory deficits with only 62.50 % identification score (Fig. 31c).

Taken together, these translational data implicate early hyposmia, most likely due to the loss of LC axons and consequently reduced noradrenaline release in the olfactory bulb, as an early biomarker of Alzheimer's disease.

Table 4: Demographic details of subjects participating in the TSPO-PET and olfaction identification test study

Abbreviations: SCI = Subjective cognitive decline, MCI = Mild cognitive impairment, AD = Alzheimer's disease

Diagnosis	#	Age (years)	Gender M | F	β-amyloid 1-42 (pg/ml)	β-amyloid 1-40 (pg/ml)	Tau (pg/ml)	p-Tau (pg/ml)
Control	14	71.26	7 | 7	1118.440	14111.077	290.119	55.978
SCI / MCI	17	68.11	9 | 8	517.949	13968.500	675.225	90.384
AD	16	73.87	3 | 13	520.738	13125.833	476.127	83.358

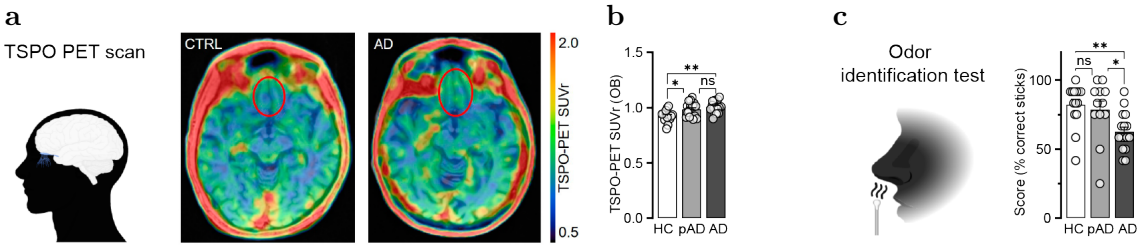

Figure 31: Clinical assessment of AD patients

(a) Human TSPO-PET scan. Horizontal section of a healthy and an AD human brain imaged with TSPO PET tracer. The olfactory bulb is highlighted by a red circle. **(b)** Standardized uptake value ratio (SUVr) of TSPO in the OB is elevated in pAD and AD patients (Control: n = 14, pAD: n = 17, AD: n = 16). **(c)** Odor identification test revealed pAD patients to perform only sightly worse in identifying the correct odor than healthy patients, while AD patients showed strong olfactory deficits (HC: n = 14, pAD: n = 12, AD: n = 16); Data are expressed as mean ± SEM; ns, not significant; *p<0.05, **p<0.01.

4 Discussion

The present study provides evidence that early onset degeneration of locus coeruleus axons in the olfactory bulb drives olfactory impairment in Alzheimer's disease.
Hyposmia, a reduction in the sense of smell is an early symptom in the preclinical phase of AD with approximately 60 % of MCI patients experiencing olfactory difficulties. Up to date, it is not yet understood why olfaction is one of the first systems to be affected and what causes the olfactory impairments. To address these questions, we investigated the role of the LC-noradrenergic system in the olfactory bulb in an Aβ-mouse model of AD and in human patients. The LC is considered a selectively vulnerable cell population that suffers from toxic protein accumulation and cell loss early on. In contrast, little attention has been paid to its axons which project to almost the entire central nervous system.

The main findings of this project are:
LC axons in the OB of $APP^{NL\text{-}G\text{-}F}$ mice already degenerate at 2 months of age. This early axon loss is specific to the olfactory bulb and is accompanied by a reduction in odor-induced noradrenaline release, leading to olfactory deficits in these animals. LC axons are most likely compromised internally by intraneuronal Aβ. This causes hyperexcitability which induces the externalization of the 'eat-me' signal phosphatidylserin triggering microglia to phagocytose the axons via MFG-E8 (Fig. 32). Modulation of microglia function could abolish LC axon loss and prevent olfactory decline. Importantly, we were able to translate our findings to humans. In post-mortem OB tissue from prodromal AD patients, significant LC axon loss was observed. In living AD patients, TSPO-PET scans revealed an early OB specific microgliosis and hyposmia was diagnosed.

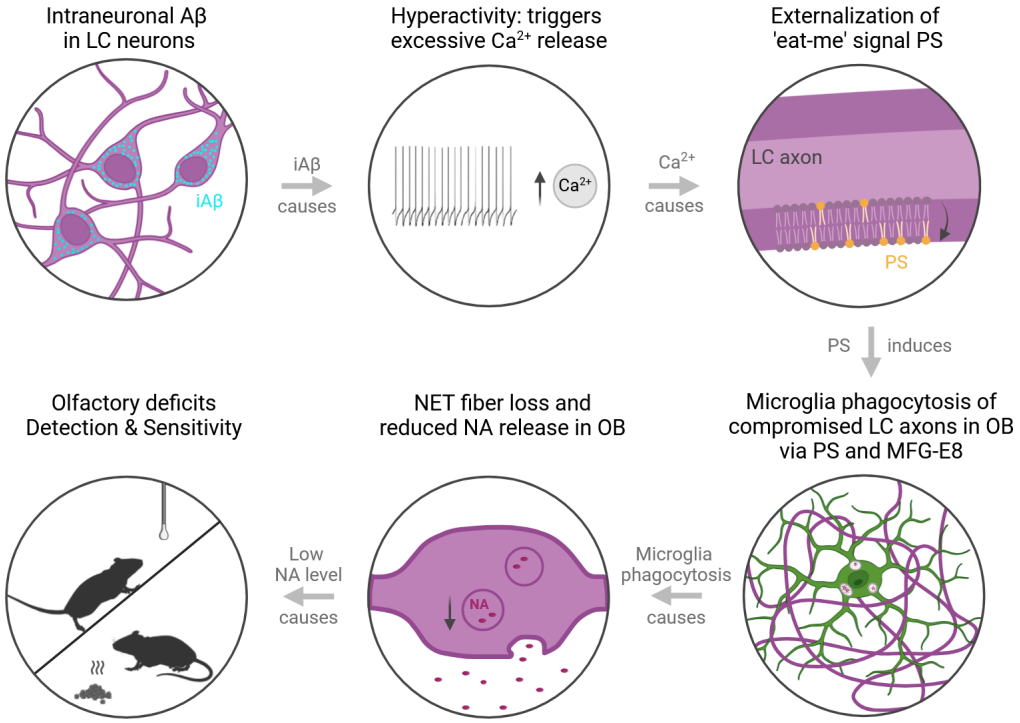

Figure 32: Degeneration of LC-noradrenergic system

Flow diagram visualizing the successive decline of the locus coeruleus-noradrenergic system which leads to olfactory deficits in $APP^{NL\text{-}G\text{-}F}$ mice (Graphic was created on BioRender).

4.1 Early LC axon loss is specific to the olfactory bulb

By systematic comparison of brain regions that are specifically early affected in the development of AD, we aimed to decipher in which region the LC-noradrenergic system of $APP^{NL\text{-}G\text{-}F}$ mice is impaired first. One study has already analyzed the LC axon density in this mouse model, however only at late disease stages of 12 and 24 months of age. They demonstrated a prominent LC axon loss in the neocortex and hippocampus, as well as in the entorhinal cortex and prefrontal cortex [165]. We revealed the olfactory bulb to show LC axon degeneration as early as 2 months of age. With increasing age, axon loss further progressed and was mainly observed in the internal and external plexiform layer of the OB. Other brain regions, such as the dentate gyrus, medial prefrontal cortex and piriform cortex did not show a change in LC axon density until 6 months of age. In the S1 cortex, LC axons degenerated, but only to a third of the extent as in the OB at

the same age. In another Aβ-AD model, the APPPS1 mouse line, LC axon degeneration already started at 3 months of age in the DG and PFC and at 12 months of age spread to the CA1 hippocampal region and anterior cingulate cortex [169]. In the OB, Rey et al., 2012, observed no LC axon degeneration in the same mouse line. Instead, they induced it with the neurotoxin DSP4 which caused Aβ plaque formation and olfactory deficits [123]. However, this pharmacological depletion of LC axons does not mimic the underlying disease mechanism and therefore is not suitable for investigating its origin and consequences. Hence, we are the first to explore noradrenergic axon decline at the preclinical stage of AD in an Aβ-AD model and also beyond an immunohistological analysis, correlating it to olfactory impairment.

4.2 APP$^{\text{NL-G-F}}$ mice experience olfactory deficits due to reduced noradrenaline release in the olfactory bulb

Previous studies have shown that LC axon loss underlies cognitive deficits in AD mouse models [120–123, 170], as for example object-memory impairment [121], spatial learning [122] and olfactory deficits [123]. Our results confirm this, showing APP$^{\text{NL-G-F}}$ mice to suffer from olfactory impairments. Importantly, 1-month-old APP$^{\text{NL-G-F}}$ animals did not show an olfactory phenotype which coincides with no LC axon loss at that age. Instead, the degree of LC axon loss correlates with the decline in olfactory performance, clearly pointing to a direct, causal relationship. Of note, 6 month-old male mice performed significantly better in the buried food test than female mice and interestingly both in WT and APP$^{\text{NL-G-F}}$ mice. In 5xFAD mice, the same sex difference was observed. 6.5-month-old males found the buried food pellet faster than females [170]. Possible differences in WT mice were not discussed, however, another study reported female WT mice to have a higher odor sensitivity compared to male mice which is contrary to our finding [171]. There could be several explanations for the observed sex difference in APP$^{\text{NL-G-F}}$ mice. Masuda et al., 2016 quantified the Aβ plaque load in these animals and revealed old females to have higher amyloidosis in the forebrain and midbrain compared to males [172]. In the olfactory bulb we observed no significant difference in Aβ plaque density between

the genders and thereby we exclude it as a possible reason. Moreover, also the LC axon density was comparable between the genders at all ages. In humans, females are more prone to develop Alzheimer's disease but men show olfactory dysfunction earlier and more severely than female patients. Around 90 years of age, both genders reach a comparable level of olfactory impairment [173]. The early olfactory sex difference was suggested to be due to a lower number (-43.2 %) of olfactory bulb neurons and glial cells with respect to OB mass [174]. Whether this difference is present in the OB of $APP^{NL\text{-}G\text{-}F}$ mice would need to be addressed, but it can not explain the better olfactory performance observed in male animals.

Another interesting finding was that even WT mice needed more time to find the food pellet when getting older. 6-month-old mice took more than double the amount of time to locate the hidden food compared to 3-month-old animals, highlighting the normal decay of the olfactory sense which can also be observed in humans. In 2023, Slabik and Garaschuk, reported a decline in olfaction as a function of age. People older than 60 years are prone to develop olfactory deficits, mainly in the form of olfactory detection problems [151].

Which odor ability (identification, sensitivity, detection or discrimination) is primarily impaired in $APP^{NL\text{-}G\text{-}F}$ mice was not tested in detail. The buried food test mainly accesses olfactory detection, the ability of an animal to perceive the presence of an odor, here the buried food pellet. The sensitivity test on the other hand measures the olfactory sensitivity and determines a threshold for detecting an odor. $APP^{NL\text{-}G\text{-}F}$ mice showed an impairment in both test. Our data suggest that the mice have a reduced sense of smell with a higher threshold for detecting odors and therefore we conclude that the mice have an impairment in the odor abilities detection and sensitivity.

Noradrenaline plays an important role in odor detection and facilitation of low odor concentrations [75, 129, 130]. Mitral cells, the main output neurons of the OB, are primarily influenced by NA, as they express all three noradrenergic receptors [129]. NA release increases the mitral cell excitability by binding to $\alpha 1$ receptors and thereby converting a subthreshold excitatory synaptic response into a suprathreshold response that can trigger action potential firing. In addition, NA acts on inhibitory granular cells. Modulating their strength influences the inhibition of mitral cells as a function of NA level [129, 130]. Behaviorally, this increases the sensitivity to weak odors. Escanilla et al., 2010, showed in

vivo that an infusion of NA into the OB increases the detection threshold of low concentration odorants [38]. Given that in $APP^{NL\text{-}G\text{-}F}$ mice LC axons are strongly reduced in the internal and external plexiform layer we suggest that mitral cells and granular cells which are located in these layers are primary affected by a reduction in NA level, explaining the observed olfactory phenotype.

Several studies have already shown LC axon loss to result in a reduction of NA release. [120, 175, 176]. Therefore, we hypothesized that the loss of LC axons in the OB also induces a decline in the NA concentration and that this underlies the olfactory impairment. In order to prove this we carried out four independent experiments that accessed the noradrenaline concentration and related it to olfaction.

First, a noradrenaline Elisa from OB tissue of WT and $APP^{NL\text{-}G\text{-}F}$ mice was performed, that showed only a trend towards a reduced NA level, but no significant difference. Several methodological reasons could explain this outcome. For the harvest of the brain, mice were anesthetized with isoflurane and subsequently injected with ketamine-xylazine before perfusion. Both isoflurane and ketamine were shown to increase LC neuron firing and the noradrenaline concentration [177–181]. Ketamine inhibits the norepinephrine transporter (NET) resulting in an excess of NA in the synaptic cleft that cannot be recycled back into the LC axons. On top of this, the animals are exposed to stress in form of handling and anesthesia application, which further increases NA levels. These factors can explain why a possible difference in tissue NA levels could not be detected by an ELISA as excessive NA release might diminish different baseline NA levels.

Thus, we proposed that an olfactory stimulated noradrenaline release measured in vivo would be more appropriate. In comparison to WT mice, $APP^{NL\text{-}G\text{-}F}$ mice released drastically less NA in response to a vanilla air puff. NA level measurements in the cortex of a WT mouse showed no change in NA level when applying a vanilla air puff. These experiments confirm a direct connection between LC axon loss, reduced noradrenaline release and olfactory deficits.

Finally, we aimed to mimic the reduced NA level and olfactory impairment in WT mice with the help of optogenetics. However, OB specific inhibition of NA release caused no difference in the time to find a buried food pellet in comparison to control injected mice. We speculate that the inhibition of NA release in the OB was not long enough to sufficiently

change the output behavior of OB neurons, even though in patch clamp recordings LC neurons hyperpolarized and stopped firing quickly. Other studies successfully correlated reduced NA levels and olfaction, however only in the context of odor-memory tasks. Pharmacological blockage of bulbar NA receptors decreased reward motivated odor responses in rats [131] and DSP4 lesioning of cortical LC axons in mice caused a failure to remember odors [182]. In 2020, Linster et al., used optogenetic inhibition of NA release in the OB to show that a low NA level alters perseverance, duration, and specificity of odor memory, but it has no effect on odor–reward acquisition [134].

In the last approach, we used chemogenetic activation of LC neurons in $APP^{NL\text{-}G\text{-}F}$ mice to reinstate olfaction. However, CNO application to activate LC neurons could not accelerate the time to find a buried food pellet. We speculate that too many LC axons are already damaged at 6 months of age and the remaining axons cannot release enough NA for a proper functioning of the olfactory sense. This is supported by our 2-photon NA release experiment that showed a 90 % reduction in NA release already at 3 months of age, at which time point only 27 % LC axons loss was observed. Neurocircuit-homeostasis is only able to balance molecular and structural changes to a certain extent. Another possibility might be that CNO application once was not sufficient to activate NA release long-term. Two independent studies confirm that a single CNO injection cannot facilitate a previously declined behavioral performance. Instead, daily injection for several days could significantly improve delayed motor learning [120] and restore spatial reversal learning [176], both in animals that showed LC axon loss and a reduced NA level. This argues for a positive effect of increased NA in the context of olfaction and could be proven by repeating the experiment with several days of CNO application.

Taken together, the reduction of NA release in the OB, in an odor-stimulated context in vivo, points to a structure-to-function relationship between LC axons and olfaction. NA is known to enhance the detection of odorants and to increase the signal-to-noise ratio, increasing the sensitivity for weak inputs. The reduced NA release in the OB of $APP^{NL\text{-}G\text{-}F}$ mice causes a higher detection threshold for weak odors, as observed in the sensitivity test and either because of this lower sensitivity or due to odor detection/localization problems animals need more time to find the food pellet in the buried food test.

4.3 APP$^{NL\text{-}G\text{-}F}$ olfactory phenotype is LC-system specific

Although we have previously demonstrated that a reduced NA concentration in the OB correlates with olfactory deficits in APP$^{NL\text{-}G\text{-}F}$ animals, it remains questionable whether LC system dysfunction is exclusively responsible for the olfactory impairment. Not only the neurotransmitter noradrenaline, but also dopamine, acetylcholine and serotonin play an important role in olfactory perception and odor processing as explained in the introduction (see section 1.3.2). In the late 20th century, studies in human AD patients revealed a reduced acetylcholine activity in the olfactory tubercle and a loss of the dopamine D2 receptor in the OB [183, 184], however no connection to olfaction was made. Other studies investigated the impact of the different neurotransmitters in the OB on olfaction but not with regard to Alzheimer's disease [138, 139, 146, 185–188]. Thus we are the first to directly correlate LC-noradrenergic dysfunction to olfactory impairments in AD.
We carried out two complementary experiments to answer the question of specificity. First, we immunohistologically accessed the axon density of the cholinergic and serotonergic system in the OB of 3-month-old WT and APP$^{NL\text{-}G\text{-}F}$ animals. Both axonal projections remained unaffected, suggesting mainly LC axons in this mouse line to be impaired. To be more precise and to avoid the problem that potentially every cell in APP$^{NL\text{-}G\text{-}F}$ animals carries the three APP mutations and thereby affecting several systems and cell populations, we designed a virus that expresses the APP$^{NL\text{-}G\text{-}F}$ mutation only in LC neurons. APP$^{NL\text{-}G\text{-}F}$ expression in healthy Dbh-Cre mice caused LC axon degeneration in the OB and resulted in olfactory deficits. With the help of this experiment we were able to assign all effects observed in the APP$^{NL\text{-}G\text{-}F}$ mouse line specifically to the LC-system. Hence, we claim noradrenergic dysfunction exclusively to drive olfactory impairments in AD.

4.4 Electrophysiology reveals APP$^{NL\text{-}G\text{-}F}$ LC neurons to be hyperactive and the mitral cell integrity to be intact

Electrophysiological recordings of single neurons enable to get an insight into the cells intrinsic and extrinsic properties, cellular excitability and ion channel functions. We used the perforated patch-clamp method because it has the advantage of preserving the cell's

intracellular environment. This allows for more accurate measurements of physiological properties, such as ion channel activity and cellular responses to stimuli [189].

The properties and excitability of LC neurons and mitral cells of 6-month-old WT and $APP^{NL\text{-}G\text{-}F}$ animals were compared to elucidate possible alterations. The most intriguing finding was a hyperactive phenotype of LC neurons. This is in line with recent data of LC neurons in neurodegenerative diseases [23, 190, 191], but was not yet shown in the $APP^{NL\text{-}G\text{-}F}$ mouse line. Here, the spontaneous firing frequency was double as high as in WT neurons. Pacemaking of LC neurons is suggested to be mediated by low-threshold L-type and T-type Ca^{2+} currents. The firing frequency is mainly influenced by calcium-activated potassium channels (SK channels) and voltage-gated potassium channels (Kv channels) [96, 97]. SK channels are activated by calcium influx and lead to a potassium efflux that hyperpolarizes the membrane, resulting in the LC typical afterhyperpolarization that follows each action potential. Kv channels contribute to the repolarization during and after the action potential. They influence the duration of the action potential and the subsequent afterhyperpolarization, thereby helping to set the firing frequency. Mice lacking Kv1.4 channels were shown to have increased firing rates in the suprachiasmatic nucleus neurons and nucleus accumbens neurons, suggesting that the loss of Kv1.4 expression leads to higher firing rates in neurons [192]. We did not look into ion channels, and can therefore only speculate that the increased firing frequency observed in $APP^{NL\text{-}G\text{-}F}$ neurons is due to a change in SK and/or Kv channel properties or expression. None of the other LC neuron properties, such as delayed excitation, input resistance or conduction that could have explained the hyperactivity were affected. Additionally, not all $APP^{NL\text{-}G\text{-}F}$ neurons were hyperactive, just roughly 50 %. Either only some cells are compromised at that disease stage or it is in general only a subset of neurons being affected. Type 1 cells, mainly fusiform neurons have a narrow AP shape and project to the forebrain. Type 2 cells are multipolar neurons that send their axons to the spinal cord and cerebellum [70, 101, 102]. With regard to the degeneration of LC axons exclusively in the OB at early time points, it is likely that mainly fusiform, type 1 neurons are hyperactive.

Furthermore, we found that the $APP^{NL\text{-}G\text{-}F}$ cell excitability upon current stimulation was reduced. However, one would have expected an increased excitability based on the hyperactivity. Most likely SK channels are involved again, increasing the hyperpolarization

phase after the action potential by potassium efflux. A prolong afterhyperpolarization was not observed in the neuron, though. We rather measured a decrease of the slow afterhyperpolarization amplitude which is again contradictory to the decreased excitability.

Next to LC neurons, we recorded mitral cells, since the olfactory phenotype observed might be a consequence of impaired mitral cell function. However, in 6-month-old $APP^{NL\text{-}G\text{-}F}$ we could not detect any electrophysiological differences compared to WT animals. All mitral cells showed a diverse spontaneous firing pattern with unaltered frequencies. In a recent study from Deng et al., 2024, 3-month-old APPPS1 mitral cells were found to be hyperactive, because of reduced GABAergic transmission [193]. In 2-month-old P301S mice a reduced mitral cell activity was recorded with mitral cell loss at 9 months of age because of Tau accumulation inside the neurons [194].
We identified two mitral cell subpopulations based on their intrinsic properties. To the best of our knowledge, these two electrophysiological different subtypes have not been described until now. Studies have found different intrinsic properties, expression of different markers, different ion channels [195] and depending if mitral cells project to the same or a different glomeruli they have a different strength of the sag which was shown to be mediated by hyperpolarization activated cyclic nucleotide gated channel 2 [196, 197]. But so far, mitral cells were mainly classified based on their secondary dendrites which project either to the inner or outer external plexiform layer [198]. We were able to match the electrophysiological subtype 1 to the morphological subtype that extents its dendrites into the inner layer of the EPL. Subtype 2 projects its secondary dendrites into the outer layer of the EPL. Based on this morphological difference, the mitral cell synaptic activity is differentially modulated. Subtype 1 cells mainly receives inhibitory input by granular neurons, whereas subtype 2 cells are innervated and inhibited by tufted cells.
Collectively, we identified two different electrophysiological and morphological mitral cell subtypes in the olfactory bulb. Their integrity in $APP^{NL\text{-}G\text{-}F}$ mice remained unaltered, and therefore we conclude that the olfactory impairment observed in those animals is not driven by compromised mitral cells. Instead, we hypothesize that hyperactive LC neurons trigger a signaling cascade that is responsible for the degeneration of LC axons and thereby a reduced noradrenaline release. Lack of NA modulation consequently underlies

the olfactory phenotype. Important to note here is the discordance between hyperactivity and a lower neurotransmitter level. Theoretically, one would have expected a high firing frequency to cause a high transmitter release. However, the NA level measurement in vivo showed a strong decline. Either the available neurotransmitter pool is depleted or not all action potentials reach the far-away synaptic terminals in the OB. Since LC axons are non-myelinated and the distance to the OB is very long, electrical stimulation in $APP^{NL\text{-}G\text{-}F}$ axons might not be sufficient to trigger high neurotransmitter release or axons are clogged with accumulated proteins, organelles and vesicles, impairing axonal transport and action potential propagation [199, 200].

4.5 $APP^{NL\text{-}G\text{-}F}$ olfactory bulb microglia have an increased phagocytotic activity, clearing hyperactive LC axons over PS - MFG-E8 signaling

Microglia are dynamic and heterogeneous immune cells that communicate with other cell types in the brain and play both protective and deleterious roles in AD. RNA sequencing and proteomics revealed a remarkable heterogeneity of microglia in the $APP^{NL\text{-}G\text{-}F}$ mouse model [167, 168]. Olfactory bulb microglia were not yet profiled.

Our data revealed an increased number of OB microglia by three independent experiments. Immunofluorescence, microglia isolation and TSPO-PET scans of 2-3 months old mice showed an average increase of 21 % in microglia number/activity in $APP^{NL\text{-}G\text{-}F}$ animals compared to WT animals. Notably, the single cell volume and morphology was unchanged.

In small animal TSPO-PET scans, TSPO expression in healthy WT mice was found to be low in the brain, and only increases upon inflammation. A remarkable exception is the olfactory bulb and olfactory epithelium. Here, TSPO binding is high already in young WT mice, as we and others could show [201]. In $APP^{NL\text{-}G\text{-}F}$ mice the OB is also the first region to show an increase in TSPO signal as early as 2.5 months of age. In other regions, including the cortex and hippocampus, TSPO signals only increased between 5-7.5 months of age [202]. Studies looking closer into TSPO signal differences identified

female mice to have a stronger TSPO signal longitudinally measured, which positively correlates to oligomeric Aβ plaques in the cortex [172] but was independent of fibrillar Aβ that was shown to be sex independent [203]. In our small animal TSPO-PET study, only female mice were used, limiting the possibility of a correlation between gender and Aβ deposition. Of note, in immunostainings the increase of microglia area correlated with the extracellular Aβ plaque load but no sex difference in oligemeric Aβ plaques in the OB was observed at 3 and 6 months of age. Additionally, when comparing the OB to other brain regions like the cortex, which displays a higher plaque load at the early disease stage, no such microglia increase was observed. Thus, we conclude that microglia respond to Aβ but some other mechanism specific to the olfactory bulb has to trigger the strong increase of microglia number/activity.

RNA bulk sequencing of isolated microglia identified 2344 significantly regulated genes that describe a homeostatic microglia population without DAM signature. Gene ontology analysis suggested microglia on top to be actively involved in synaptic pruning. 8-month-old cortical microglia on the other hand showed a decrease of homeostatic genes and an increase in disease-associated genes [167]. Hence, this points towards a more homeostatic phenotype of OB microglia in 2-month-old $APP^{NL\text{-}G\text{-}F}$ mice. A phagocytosis assay of isolated OB microglia further confirmed this assumption. $APP^{NL\text{-}G\text{-}F}$ microglia phagocytosed more synaptosomes than WT microglia. Together with the data collected from immunstaining and RNA sequencing, we can classify OB microglia as healthy, active phagocytosing. Since they have a normal ramified morphology and don't express pro-inflammatory cytokines such as tumor necrosis factor-alpha and interleukin-beta, they are not reactive excessive phagocytosing as it is often the case in neurodegeneration [204, 205].
Collectively, $APP^{NL\text{-}G\text{-}F}$ OB microglia are actively surveying and phagocytosing immune cells which is a neuroprotective function, as it helps clear debris, prevent inflammation, and maintain tissue homeostasis.

But, can microglia phagocytosis account for the LC axon loss taking place in the OB? To this end, we performed an immunostaining for LC axons, microglia and their lysosomes with subsequent 3D reconstruction. In both genotypes, we detected NET signal

inside the lysosomes of microglia which suggests an uptake of LC axons my microglia, also in healthy animals. However, comparing the volume of NET signal between the groups showed a higher proportion in $APP^{NL\text{-}G\text{-}F}$ microglia than in WT microglia. Thus, degradation of LC axons by microglia is largely increased in $APP^{NL\text{-}G\text{-}F}$ mice.

Microglial structural remodeling of noradrenergic axons has been shown before in the spinal nucleus of rats [206]. Hayashi et al., 2023 demonstrated that LC axons innervating the trigeminal spinal subnucleus caudalis degenerate after nerve injury and microglia via the histocompatibility complex class I are responsible for the degradation of these axons [206]. In the OB of $APP^{NL\text{-}G\text{-}F}$ we found PS-MFG-E8 signaling to initiate microglial phagocytosis. We identified PS, a commonly known 'eat-me' signal expressed on LC axons. PS in healthy cells is mainly localized to the inner cellular membrane. Upon a stimulus it will be flipped to the extracellular membrane and thus serve as a tag for microglia recognition [58]. The main stimulus for the externalization is calcium. An elevation in intracellular calcium levels activates the scramblase TMEM16 which flips PS from the inner to the outer membrane [207]. Our data suggest that LC neurons of $APP^{NL\text{-}G\text{-}F}$ mice contain more intracellular calcium due to their hyperactive phenotype. During the spontaneous action potential firing voltage-gated calcium channels open and calcium enters the cell. Hyperactivity causes these channels to open more frequently, elevating intracellular calcium levels. Therefore, a higher amount of flipped PS can be found on $APP^{NL\text{-}G\text{-}F}$ LC axons than on WT LC axons. Once PS is exposed extracellular it can be recognized by several microglial receptors [208]. We identified MFG-E8, a glycoprotein and adaptor molecule to bind to PS which in turn binds to microglial vitronectin receptors, the $\alpha v\beta 3/5$ integrins [208–210]. Interestingly, we didn't detect more contact points between microglia and LC axons in $APP^{NL\text{-}G\text{-}F}$, as one would have expected. Several studies reported microglia both in the healthy and diseased state to frequently contact neurons to monitor their state. Via 2-photon-microscopy it was shown that microglia in their resting state have highly mobile protrusions, making minutes long contacts to cells in their environment, monitoring their state and only upon positive feedback, like 'eat-me' signals initiate phagocytosis and otherwise retract again [211, 212]. In addition, one has to take into account that microglia are heavily modulated by noradrenaline [109, 111, 213, 214]. Our phagocytosis assay demonstrated an increased microglial phagocytosis of synaptosomes in the presence

of noradrenaline. This is in line with an in vivo study showing noradrenaline stimulation to promote microglia migration towards Aβ and a higher Aβ phagocytosis. The effects reversed when depleting noradrenaline [111]. These findings are contradictory to our data of elevated phagocytosis in APP$^{\text{NL-G-F}}$ that evidently have reduced noradrenaline levels in the OB. Hence, we hypothesized that microglia in the OB are unique compared to other brain regions. Either they are differentially regulated by noradrenaline or generally have a different genetic profile. They have equal contacts to LC axons in WT and APP$^{\text{NL-G-F}}$ mice and only in case of an exposed PS signal clear compromised LC axons.

In the olfactory bulb and dentate gyrus, two regions of adult neurogenesis, synaptic pruning takes place via PS-MFG-E8 signaling. Here, less active spines of adult-born cells get tagged with PS, which is recognized by MFG-E8 and subsequently phagocytosed by microglia [57]. The constant exposure to PS as a signal in order to promote synaptic plasticity might sensitize microglia to this specific stimulus. Therefore, PS located on hyperactive LC axons in the olfactory bulb is detected with a higher probability and fidelity compared to other regions, providing a rationale for the early axon loss preceding all other highly LC-innervated regions.

In summary, we elucidated a mechanism underlying LC axon loss in the OB via PS-MFG-E8 signaling and subsequent clearance by microglia.

4.6 Vulnerability of the LC-noradrenergic system

The human LC is one of the first regions to display pathological Tau aggregates and cell loss, both in aging and in a variety of neurodegenerative diseases. But why do LC neurons show this selective early-onset neuronal vulnerability? Since decades, scientists try to answer this question and several possible scenarios have been suggested.

First, LC neurons have very long, unmyelinated axons and are autonomous pace making cells. Both characteristics require very high energy demand. ATP production relies on glycolysis and mitochondrial oxidative phosphorylation. We and others could show that LC neurons in AD are hyperactive. This leads to a higher influx of Ca^{2+} which contributes to autonomous pace making. If Ca^{2+} is present excessively, though, it produces reactive oxygen species (ROS), leading to oxidative stress in mitochondria which eventually triggers

mitochondrial dysfunction and therefore sufficient energy supply is not ensured anymore [97, 215].

Second, LC neurons are prone to environmental factors. Inflammation [122, 216], viral infection, sleep [217, 218], diet [219], and stress [220] have been shown to negatively influence the LC function and disease progression in the course of AD.

Third, the LC is located adjacent to the fourth ventricle, directly exposing it to substances circulating the CSF. It was shown that LC neurons exhibit cellular stress in response to toxic molecules from the CSF [221, 222]. In the LC of AD patients, DOPEGAL, a toxic monoamine oxidase A metabolite of NA, was found to be increased. Kang et al., 2020 showed that overactivation of LC neurons leads to the production of DOPEGAL which activates an asparagine endopeptidase that cleaves Tau and promotes its aggregation. This cascade induces neurotoxicity and LC neuron death [221, 222].

Next to these threats that should potentially effect the whole LC population uniformly, it is important to consider that in humans LC neurons do not degenerate evenly distributed. During AD pathology the rostral part of the LC is more vulnerable than the caudal portion [223–226]. The LC consists of a heterogeneous cell population with small fusiform cells localized along the rostral-caudal axis that project to the forebrain. Neurons in the caudal part of the LC are large multipolar neurons that project to the cerebellum and spinal cord [66]. In the human LC, hyperphoshorylated Tau mainly accumulates within the rostrally located fusiform neurons and the LC neuron loss is most prominent rostrally [224–226]. Rostral neurons send output to and receive input from forbrain regions like the hippocampus and piriform cortex which are heavily affected by Tau and Aβ pathology in AD. Moreover, we speculate that these long range axon projections have a higher energy demand than short range projection from the caudal LC region. Rostral fusiform LC neurons were shown to have different electrophysiological properties than caudal multipolar neurons [70, 101] and likely express different receptors which might make them differentially vulnerable to toxic Tau and/or Aβ.

4.7 Intraneuronal Aβ compromises LC neurons in APP$^{\text{NL-G-F}}$ mice

Several studies tried to unravel the underlying mechanism of olfactory dysfunction in AD mouse models. Despite the use of different mouse lines most of them suggest Tau and/or extracellular Aβ to be the trigger of olfactory impairment. In APPPS1 mice, Aβ correlates with olfactory deficits [227] and causes hyperexcitability of mitral cells [193]. In 5xFAD mice, olfactory impairment was observed due to Aβ induced degeneration of OSNs [159], while an additional Aβ seeding in the OB altered neurogenesis and reduced the mitral cell activity, leading to severe deficits in several olfactory tests [228]. In Tg2576, Aβ triggered the death of periglomerular cells [229] and in 3xTG mice Aβ induced degeneration of neurons found in the EPL and GL layer of the OB [170]. Apart from these publications, only one study investigated the role of the LC-noradrenergic system in olfaction in AD, however with the use of toxin-induced degeneration of LC projections. The group of Heneka and colleagues, employed a 9-month-long DS4P treatment in APPPS1 mice. DSP4 ablated LC axons in the OB and increased the Aβ-plaque load. Olfactory recognition tests showed 12-month-old APPPS1 mice to exacerbate their olfactory phenotype under DSP4 induced LC axon loss [123].

Our study could show intraneuronal WO-2-positive Aβ oligomers inside LC neurons of 2-month-old APP$^{\text{NL-G-F}}$ mice. The signal was present in all cell bodies, without any difference in the rostro-caudal axis. In 6-month-old mice, the signal declined. We could not visualize intraneuronal Aβ in LC axons of the OB due to technical limitations and the question of the correct time point to detect it there. Electron microscopy could be carried out to visualize the signal. We speculate that intraneuronal Aβ inside LC neurons is cleaved from APP as early as 1 month of age and then is transported anterogradely by multivesicular bodies through the LC axons into the OB [28, 30]. Alternatively, it might also get internalized from the extracellular space by Aα7nAChR receptors. Notably, these receptors are mainly expressed on LC and dorsal raphe nuclei, possibly explaining why LC neurons have a high intraneuronal Aβ load [27]. LC axons in the infralimbic mPFC of Dbh-rats were shown to contain endogenous intraneuronal Aβ42 (MOAB2) by electron microscopy [230] and in human post-mortem tissue from AD patients and in APP-PSEN1

mice, Kelly and colleagues also detected intraneuronal Aβ in the cytoplasm of LC neurons, although using a different antibody [23]. The choice of antibody for detecting intraneuronal Aβ is of importance as several marker against the C-terminus of the APP protein exists but their possible cross-reactivity to the full-length APP protein limits their specificity. Therefore, our finding with the WO-2 antibody has to be interpreted with caution. Nevertheless, the fact of a strong signal at the early stage that declines over time makes us confident to suggest that LC neurons are compromised internally by intraneuronal Aβ, likely triggering LC neurons to become hyperactive.
Important to keep in mind is that the $APP^{NL\text{-}G\text{-}F}$ mouse line used in this study only models the Aβ pathology. Crossing heterozygous $APP^{NL\text{-}G\text{-}F}$ with heterozygous hTau mice showed that also Tau can induce LC axon degeneration in the OB, however not to the same extend as Aβ and only starting at a more advanced disease stage.

Why do $APP^{NL\text{-}G\text{-}F}$ mice experience LC axon loss selectively in the olfactory bulb at early time points? We were able to exclude LC neuron loss and intraneuronal Aβ accumulation to be specific for the LC neuron subpopulation that projects to the olfactory bulb. Instead, we found just a subset of neurons to be hyperactive, but if that is just biological variance between the animals or if this subset exclusively projects to the olfactory bulb, remains to be further investigated. We speculate that the excessive Ca^{2+} influx in hyperactive neurons, due to elevated intraneuronal Aβ, triggers an externalization of the 'eat-me' signal PS and that microglia in the OB detect PS with a higher probability to other regions, as the OB is known for PS mediated removal of synaptic spines during adult neurogenesis by microglia. In addition, LC axons that project to the OB are one of the longest LC projections and therefore they have a high energy demand, making them vulnerable for ROS and mitochondrial dysfunction [97, 215].

4.8 Modulation of microglia function abolishes LC axon loss and prevents olfactory decline

The discovery of microglial phagocytosis to drive LC axon degeneration, let us to probe whether a genetic down regulation of microglia phagocytosis might abolish the LC axon

loss and prevent olfactory deficits. In 2023, Fairley and colleagues identified the mitochondrial membrane protein TSPO as a crucial player in microglial respiratory metabolism and energy supply for phagocytosis. The knockout of TSPO in WT mice induced impaired mitochondrial oxidative phosphorylation, reduced mitochondrial ATP levels and reduced respiration. A phagocytosis assay with cultured TSPO-KO microglia demonstrated an impairment in the phagocytosis of Aβ [231]. Additionally, the study also investigated the knockout of TSPO in 9-month-old $APP^{NL\text{-}G\text{-}F}$ mice and could show a similar reduction in the phagocytosis of Aβ. Making use of this discovery, we quantified the LC axon density in the OB of $APP^{NL\text{-}G\text{-}F}$ x TSPO-KO animals. Notably, the LC axon loss was abolished in all age groups and less NET signal was found inside the lysosomes of microglia compared to $APP^{NL\text{-}G\text{-}F}$ mice. Thus, the reduction of phagocytosis by TSPO-KO could indeed halt microglia from phagocytosing LC axons. Whether this finding implies that LC axons are healthy and distribute sufficient amounts of noradrenaline for the normal function of the olfactory sense, needed to be elucidated, though. A staining against MFG-E8 showed, that LC axons are highly tagged with the adaptor protein MFG-E8 and therefore theoretically also with the 'eat-me' signal PS, pointing towards compromised LC axons. The buried food test in 3-month-old animals, however, showed that the animals have a good olfactory ability, even comparable to WT mice.

Altogether, we could demonstrate once more, that microglial phagocytosis is responsible for the degeneration of LC axons and its inhibition can abolish the axon loss, even preserving olfaction. What remains to be proven, is that the LC system, although still compromised, can apparently release enough noradrenaline in the OB for a normal functioning of the olfactory sense. In order to show this, one would again need to measure the noradrenaline release in vivo with olfactory stimulation, as done in the results section 3.2.2.

4.9 Olfactory bulb LC axon loss, microglia activation and hyposmia serve as early biomarkers for AD in humans

Hyposmia is increasingly recognized as a potential biomarker for Alzheimer's disease, since many patients exhibit olfactory deficits in the preclinical stage of the disease. However,

despite its diagnostic relevance, the underlying mechanisms linking olfactory dysfunction to AD pathology remain unclear. We translated our data collected in the $APP^{NL\text{-}G\text{-}F}$ mouse model to human patients in order to access the translatability of our proposed mechanism for olfactory dysfunction.

We found LC axon loss in OB post-mortem tissue of prodromal AD patients. Surprisingly, it did not decline much further in the late AD stage. So far, human studies have only addressed the LC-noradrenergic system at the level of the LC. The volume and number of LC neurons decreases as a function of disease progression [23, 112, 115, 116]. Here lies the main difference between the human situation and the mouse model we used in this study. $APP^{NL\text{-}G\text{-}F}$ mice don't experience LC neuron loss, only axon degeneration. We did not have post-mortem tissue from the OB and LC regions of the same patients to investigate whether LC axons or LC cell bodies degenerate first. However, the fact that 60 % of LC axons are lost in the OB of pAD patients, while only 30 % of LC neurons have declined at this stage according to Kelly et al., 2017 [113], points towards LC axon loss preceding cell loss. In humans, the degeneration of LC cell body would follow, while in $APP^{NL\text{-}G\text{-}F}$ mice, somata are preserved. Axonal swelling and degeneration were shown to be common phenomenons in several neurodegenerative diseases [26, 200]. In AD, LC axons experience some kind of damage, possibly by intraneuronal Aβ, initiating Wallerian degeneration, a progressive breakdown of the cytoskeleton from the axon terminal towards the cell body. We hypothesize that in the $APP^{NL\text{-}G\text{-}F}$ mouse model Aβ only causes LC axon loss, while Tau in humans induces LC neurodegeneration.

In addition to the analysis of post-mortem tissue, we had the opportunity to obtain live human data. TSPO-PET scans showed an increase in microglia number and/or activity in the OB of pAD patients, which, similar to the LC axon density did not change much further in AD patients. This finding was accompanied by no further increase or decrease in CSF Tau and Aβ levels, respectively. TSPO-PET scans in humans are frequently carried out to access neuroinflammation as an indication for neurodegenerative diseases. Over the past decades, different TSPO radiotracers ([11C]-PK11195, [11C]-PBR28, [11C]-ER176, [18F]-GE-180, [18F]-GE-387, and [18F]-DPA714) have been used and refined to provide the most accurate prognosis of neuroinflammation in order to classify patients in disease progression [232–234]. Depending on the tracer, the sample size of the groups and the

ethnicity of participants, opposite conclusions and correlations have been drawn. In most studies, the TSPO signal in MCI and AD patients correlates with Aβ and Tau as well as with cognitive, memory and language performance [235, 236]. On the other hand, some studies reported no association between neuroinflammation and either Tau or Aβ and cognitive function [237–239]. A comprehensive overview of all studies can be found in the review by Gouilly et al., 2022 [240].

To the best of our knowledge, no human TSPO-PET study has yet evaluated the TSPO signal in the OB in the context of olfaction in AD. Klein et al., 2021, demonstrated an association between olfactory impairment and microglial neuroinflammation, but only in the cortex and in the hippocampus [241]. Our study is therefore the first to demonstrate neuroinflammation in the OB of MCI patients. Despite the widespread use of TSPO-PET scans it remains unclear whether TSPO is a marker for microglial density or activation state. Two independent publications have recently stated that TSPO in humans reflects the microglia number, whereas in mice it is an indicator for microglia activation [242, 243]. In our animal model, we were able to show that the elevated TSPO-PET signal is associated with both an increase in microglia numbers, but also with an increased phagocytotic activity. For our human TSPO-PET data this needs to be further investigated.

Despite this disagreement between TSPO-microglia density or activation, our finding of LC axon loss in post-mortem tissue coupled to an upregulation of TSPO-PET signals in the OB of living human pAD patients makes us suggest that microglia phagocytose LC axons, as observed in $APP^{NL\text{-}G\text{-}F}$ mice.

Following TSPO PET scans, olfactory assessment of the same group of patients showed a trend towards olfactory deficits in pAD, whereas hyposmia could be diagnosed in late-stage AD patients. Correlation between the odor identification score and TSPO PET signals showed no relationship. Various studies have accessed olfactory impairment as an early biomarker for AD with similar results. About 60 % of MCI patients suffer from hyposmia, several years before the onset of cognitive symptoms. The olfactory ability was strongly related to the patient's gender, ApoE allele and disease stage [158, 244] but not to Aβ or Tau [245, 246].

Our human study has certain limitations, including the small sample size, the focus on Caucasian participants and the lack of ApoE information. This reduces the specificity of

our data and most likely explains why MCI only showed a trend towards impaired olfaction, but not showed hyposmia as observed in studies with a large sample size. Moreover, not all subjects participated in the odor identification test after the PET scan, reducing the power to detect possible correlations. Nevertheless, since olfactory impairment in pAD is a recognized symptom in early AD, the data supports the hypothesis that early LC axon degeneration contributes to hyposmia in AD.

4.10 Conclusion and future perspectives

In conclusion, our study highlights that degeneration of the LC-noradrenergic system drives olfactory deficits in Alzheimer's disease. It is the first time that a mechanism linking the preclinical symptom hyposmia and LC axonal dysfunction has been provided. Future work can now further expand on the following questions: Why are LC axons in the OB most vulnerable compared to other brain regions, is intraneuronal Aβ really the trigger for LC system dysfunction, and most importantly, how can our findings actively promote early detection and intervention of Alzheimer's disease. We suggest that olfactory testing and measurements of noradrenaline levels should become an essential part of the clinical assessment of patients at risk. In case of suspicion, PET scans and MRI scans with functional connectivity between the LC and OB should follow to help disease intervention at the earliest possible time point.

5 Material and Methods

5.1 Animals

All animal experiments were approved by the Government of Upper Bavaria and followed the regulations of the Ludwig Maximilian University of Munich. Mice were bred and kept in the animal housing facility of the Center for Stroke and Dementia Research (CSD) in standard GreenLine cages (30 × 15 × 20 cm, Tecniplast) on a 12-h light/dark cycle with food and water ad libitum. For the present study, mice of both gender at the age of 1,2,3,6 and 12 months were included. The following mouse line were used:

C57BL/6J: C57BL/6J are the most widely used inbread strain. Their genome is fully sequenced. They are mainly used as a control group, when investigating diseases. C57BL/6J mice were purchased from Charles River (Germany).

APP$^{\text{NL-G-F}}$: The APP$^{\text{NL-G-F}}$ mouse line is a knock-in model, were pathogenic Aβ is elevated by inserting 3 different mutations that are associated with AD. The swedish mutation 'NL' leads to an increased total Aβ production, the ibarian mutation 'G' increases the Aβ42/ Aβ40 ratio and the arctic mutation 'F' promotes Aβ aggregation and reduces Aβ degradation. APP on the other hand is not overexpressed. APP$^{\text{NL-G-F}}$ mice are characterized by diffuse amyloid plaques starting to develop at 2 months of age, going hand in hand with micro- and astrogliosis. At 4 months of age they show synaptic loss in the hippocampus and cortex, but no neuron degeneration or neurofibrillary tangles. The mice develop memory impairment starting at 6 months of age. Mice are bread homozygous on a C57BL/6J background.

APP$^{\text{NL-G-F}}$ × Dbh-Cre: APP$^{\text{NL-G-F}}$ mice were crossed with Dbh-Cre to manipulate the locus coeruleus-noradrenergic system. Dbh-Cre are knock-in mice that express the Cre recombinase under the dbh (dopamine beta hydroxylase) promotor, making the adrenergic system accessible. The Dbh-cre has to be heterozygous the get viable and fertile mice.

APP^{NL-G-F} × TSPO-KO: APP^{NL-G-F} mice were crossed with TSPO-KO mice to access the effect of a TSPO knock-out on the noradrenergic system. The TSPO-KO mouse line was generated by the use of the Cre-lox system in which a targeting construct containing the loxP side flanks exon 2 and 3 and a neomycin cassette inserted between exon 3 and 4. The knock-out of TSPO mainly causes a reduction in microglia phagocytosis. These mice can be bread homozygous and have a global knock out of TSPO in all cells.

APP^{NL-G-F} × hTau: Heterozygous APP^{NL-G-F} mice were crossed with heterozygous hTau mice to investigate the role of Tau on the LC system. Htau mice exclusively express human Tau isoforms, no mouse Tau and have to be bread heterozygous to get viable and fertile offspring. They develop an age-dependent taupathology with hyperphoshorylated tau and neurofibrillary tangles, mainly found in the hippocampus and neocortex.

5.2 Immunohistochemistry: Mouse tissue

Mice were deeply anesthetized and transcardially perfused with phosphate-buffered saline (PBS) and 4 % paraformaldehyde (PFA). Brains got fixed by immersion in PFA at 4°C for 16 h. 50 μm thick slices were cut in a coronal plane using a vibratome (VT1200S, Leica Biosystems). Each 3-5 slices per animal containing the olfactory bulb, piriform cortex, hippocampus and locus coeruleus were used for an immunohistochemical analysis. Immunohistochemistry was performed on free-floating sections. Slices were blocked with blocking solution (10 % normal goat serum and 10 % normal donkey serum in 0.3 % Triton and PBS) for 2 hours at RT. Primary antibodies used in this study are listed in table 3. Antibodies were diluted in blocking solution and incubating over-night at 4°C on the shaker. Secondary antibodies (Table 4) were applied for 2 hours at RT on the shaker, protected against light. Slices were mounted and cover slipped with mounting medium, containing DAPI (Dako, Santa Clara, USA). Three-dimensional images were acquired with a Zeiss LSM900 confocal microscope (Carl Zeiss, Oberkochen).
For the quantification of the NET fiber density as well as Iba1$^+$ microglia and NAB288$^+$ Aβ-plaque area z-stack images of 25 μm using a 10x objective were acquired (8-bit stacks of

101.41x101.41). The staining density (area %) was analyzed with ImageJ. After a manual brightness/contrast adjustment, a threshold was set to calculate the perceptual area of NET^+ LC fibers, $Iba1^+$ microglia and $NAB288^+$ Aβ plaques. Results from 4 sections per animal from 5-8 animals per group were averaged and reported as mean ± standard error of the mean. For the quantification of intrneuronal Aβ (WO-2) in TH^+ LC neurons, single plane images with 63x magnification were acquired from 5 different locations in the LC from 4 animals each. The staining density (area %) of WO-2 in TH neurons was analyzed with ImageJ using an automated script to apply the same brightness/contrast and threshold for all pictures.

5.2.1 Microglia engulfment analysis

For the engulfment of NET protein in lysosomes of microglia, near super-resolution airyscan images were taken with a Zeiss LSM900 confocal microscope (Carl Zeiss, Oberkochen) using a plan-apochromat 63x/1x NA oil immersion objective. Images were acquired in the external plexiform layer of the OB from 5 microglia per mouse from 3 animals per group. A z-stack image of 30 μm (0.14 μm interval) was taken and microglia were selected by having their cell body in the middle of the stack, in order to visualize their full morphology. Images were subsequently 3D airyscan processed. NET signal inside $CD68^+$ lysosomes within microglia were 3D reconstructed and quantified using the Surface module in Imaris (9.6.1).

5.3 Antibodies

Table 3: Primary antibodies used in the study

Antibody name	Host	Dilution	Supplier	Catalogue no.
NET	rabbit	1:500	Abcam	ab254361
NET	mouse	1:1000	Thermo Fisher	MA5-24647
Iba1	guinea pig	1:500	Synaptic Systems	234308
Aβ (NAB228)	mouse	1:500	Santa Cruz	sc-3277
TH	chicken	1:500	Abcam	ab76442
CD68	rat	1:500	BioRad	MCA1957
WO-2	mouse	1:1000	Merck Millipore	MABN10
MFG-E8	goat	1:500	R&D Systems	AF2805
ChAT	goat	1:500	Merck Millipore	AB144P
SERT	rabbit	1:500	Merck Millipore	AB9726
HA-tag	rabbit	1:500	Sigma	H6908
GFP	chicken	1:1000	Abcam	ab13970
GFP	goat	1:5000	Abcam	ab6673
GFP	rabbit	1:1000	Thermo Fisher	A21311
Streptavidin	-	1:1000	Invitrogen	S32354
Streptavidin	-	1:1000	Invitrogen	S32357

Table 3: Secondary antibodies used in the study

Antibody name	Host	Dilution	Supplier	Catalogue no.
anti-rabbit Alexa Fluor 647	donkey	1:500	Invitrogen	A31573
anti-rabbit Alexa Fluor 488	goat	1:500	Invitrogen	A11034
anti-chicken Alexa Fluor 488	goat	1:500	Invitrogen	A11039
anti-chicken Cy3	goat	1250	Jackson	103-165-155
anti-guniea pig Alexa Fluor 488	goat	1:500	Invitrogen	A11073
anti-guniea pig Alexa Fluor 647	goat	1:500	Invitrogen	A21450
anti-guniea pig Alexa Fluor 555	goat	1:500	Invitrogen	A21435
anti-goat Alexa Fluor 488	donkey	1:500	Invitrogen	A11055
anti-rat Alexa Fluor 647	rabbit	1:500	Invitrogen	A21210
anti-mouse Alexa Fluor 647	donkey	1:500	Invitrogen	A31571
anti-mouse Alexa Fluor 594	goat	1:500	Invitrogen	A32742

5.4 Acute slice electrophysiology

Mice were anaesthetized with isoflurane and decapitated, before the brain was rapidly removed and stored in cold (4 °C) glycerol aCSF. 300 μm thick slices containing the region of the locus coeruleus and the olfactory bulb were cut in carbogenated (95 % O_2 and 5 % CO_2) glycerol aCSF using a vibration (Leica VT1200S, Leica Biosystems, Wetzlar, Germany). Slices were immediately transferred into a maintenance chamber with warm (36 °C) carbogenated aCSF. After 50 min recovery, slices were kept at room temperature (22 °C) waiting for recordings. For electrophysiological recordings, slices were individually transferred into a recording chamber and perfused with carbogenated aCSF at a flow rate of 2.5 ml/min. The temperature was controlled with a heat controller and set to 26 °C. Perforated patch-clamp recordings were obtained from LC neurons and OB mitral cells visualized with an upright microscope using a 60x water immersion objective. Biocytin labelling and post-hoc immunohistochemistry was used to confirm the right cell type. Patch pipettes were fabricated from borosilicate glass capillaries (outer diameter: 1.5 mm, inner diameter: 0.86 mm, length: 100 mm, Harvard Apparatus) with a vertical pipette puller (Narishige PC-10, Narishige Int. Ltd., London, UK). When filled with internal solution (tip-filled with potassium-D-gluconate intracellular pipette solution 1 and back-filled with potassium-D-gluconate intracellular pipette solution 2) and if needed 1 % biocytin (pH 7.2, 290 mOsm), they had a resistance of 4-5 MΩ.

Recordings on AAV5-EF1α-Flex-eNpHR3.0-EYFP injected animals were performed to validate the efficiency of the virus that by optogenetic activation should inhibit LC firing and thereby the NA release. LC neurons were patched and stimulated with a 520 nm laser diode that was placed 1 cm far away from the slice in the recording chamber (Doric Lenses, Quebec, Canada). Moreover, recordings on AAV-hSyn-DIO-h3MDGs injected animals were performed to validate the efficiency of the virus that by chemogenetic activation with CNO should activate LC firing and thereby increase the NA release. Therefore, the spontaneous firing of LC neurons was recorded before and after bath application of 3 µM CNO.

All experiments were performed using an EPC10 patch clamp (HEKA, Lambrecht, Germany) and were controlled with the software PatchMaster (version 2.32, HEKA). The

liquid junction potential (14.6 mV) was compensated prior to seal formation and recordings were always compensated for series resistance and capacity. All executed protocols were recorded with Spike 2 (version 10a, Cambridge Electronic Design, Cambridge, UK). Data were sampled with 10 to 25 kHz and low-pass filtered with a 2 kHz Bessel filter.

5.4.1 Solutions

Glycerol based slicing aCSF

230 mM Glycerol, 2.5 mM KCl, 1.2 mM NaH_2PO_4, 10 mM HEPES, 21 mM $NaHCO_3$, 5 mM glucose, 2 mM $MgCl_2$, 2 mM $CaCl_2$ (pH 7.2, 300-310 mOsm)

Regular extracellular aCSF

125 mM NaCl, 2.5 mM KCl, 1.2 mM NaH_2PO_4, 10 mM HEPES, 21 mM $NaHCO_3$, 5 mM glucose, 2 mM $MgCl_2$, 2 mM $CaCl_2$ (pH 7.2, 300-310 mOsm)

Potassium-D-gluconate intracellular pipette solution

140 mM potassium-D-gluconate, 10 mM KCl, 10 mM HEPES, 0.1 mM EGTA, 2 mM $MgCl_2$ (pH 7.2, 290 mOsm)

Potassium-D-gluconate intracellular pipette solution 2

140 mM potassium-D-gluconate, 10 mM KCl, 10 mM HEPES, 0.1 mM EGTA, 2 mM $MgCl_2$, 0.02 % Rhodamin Dextran, 200 mg/ml Amphotericin B (dissolved in DMSO) and if needed 1 % biocytin (pH 7.2, 290 mOsm)

5.4.2 Stimulation protocols and data analysis for LC neurons and mitral cells

Recorded data were analyzed with the analysis package from Spike 2. For the aquisition of electrophysiological cell parameters the following stimulation protocols and definitions were used:

Spontaneous firing frequency of LC neurons: The frequency is based on the spike count in 180 sec., without additional current injections.

Delayed excitation of LC neurons: Without additional current injections, cells were stimulated with a hyperpolarizing current pulses (1 s pulse, -10 pA increments), until the membrane potential reached -120 mV. The latency (time in ms) between the end of the stimulation and first appearing AP was measured.
Slow Afterhyperpolarization (sAHP) of LC neurons: Voltage difference (amplitude in mV) between the cell's resting membrane potential and AHP trough.
I-F curve of LC neurons: Firing frequency (number of APs per second) over increasing current injections (1 s pulse, +10 pA increments, 0-50 pA).
I-F curve of mitral cells: Firing frequency (number of APs per second) over increasing current injections (1 s pulse, +40 pA increments, 0-200 pA).
Input resistance of cell (IR): Measure of how much the membrane potential of the cell changes in response to a given input current. Using Ohm's law, dividing the membrane potential difference of the resting membrane potential and membrane potential at each current step by the current injection.
Time constant tau (τ): Time it takes from the cell's the resting membrane to reach 63 % of the cells final membrane potential. τ can be calculated by multiplying the cell's input resistance and capacitance.
Capacitance of cell (C): Measure of the cell's membrane to store electrical charge. Time constant τ divided by input resistance.
Rheobase current: Minimal current necessary to elicit an action potential, measured at a current ramp.

5.5 Behavioural experiments

All behavioral experiments were conducted during the light-phase of the animals, at the same day-time, and if possible performed in a blinded manner.

5.5.1 Buried food test

To evaluate possible differences in odor performance, C57BL/6J, $APP^{NL\text{-}G\text{-}F}$ and $APP^{NL\text{-}G\text{-}F}$ × TSPO-KO mice underwent a buried food test, which is based on the natural use of sense for food search. If an animal is unable to locate a food source within a maximum time span

of 10 minutes or if the time span is significantly longer compared to the control group, it can be concluded that olfaction is impaired. One day before the test, animals got food deprived for 18 hours. On the test day, animals got acclimated to the new environment for at least 30 minutes in a fresh cage with increased bedding volume. The test begins with placing the animal in the test cage with a food pellet hidden in the bedding. The time animals need to reach the food pellet was analyzed based on a video recording. The mean search time per genotype was calculated and compared by an unpaired student's t-test.

5.5.2 Buried food test under optogenetic and chemogenetic manipulation

Optogenetic inhibition of the noradrenaline release in the olfactory bulb was used to access the influence of a reduced noradrenaline level on olfaction. For the test, Dbh-Cre animals were treated in the same way as for the normal buried food test. After the acclimatization phase the animals optogenetic ferrule got connected to the fiber of the stimulation box and the animal could get used to the connection for 15 minutes in a fresh home cage. Then the laser (520 nm, 112 mA) was turned on for 2 minutes to inhibit the release of noradrenaline before the start of the test. The animal got transferred to the test cage and had 10 minutes to search for the food pellet, while the light was continuously switched on. The time animals with reduced noradrenaline level needed to find the hidden food pellet compared to animals with normal noradrenaline levels was compared with an unpaired student's t-test.

Chemogenetic activation of LC neurons was used to test whether an enhancement of noradrenaline release in $APP^{NL\text{-}G\text{-}F}$ could reinstate olfaction. For the test, WT and $APP^{NL\text{-}G\text{-}F}$ animals were treated in the same way as for the normal buried food test. After the acclimatization phase animals were injected intraperitoneal (i.p.) with 1 mg/kg CNO. 30 minutes later, the test started and the time both groups need to find the hidden food pellet were measured.

5.5.3 Olfactory sensitivity test

The sensitivity test evaluates whether mice can perceive odors even at weak concentrations and if they can discriminate between them. At the beginning of the experiment, the

animals got acclimated to the odor applicator (a dry cotton swab without scent) for 20 minutes to exclude the applicator itself as a potential source of error and a new, interesting object. For the test, a pleasant-smelling odor, vanilla (Dr. Oetker Bourbon Vanille-Extrakt, 7201507), got applied to a cotton swab at 2 different concentration (low 1:1000 and high 1:1). Each concentration got presented to the mouse for 2 minutes consecutively, with 1 minute break in between to change the odorant. Water, in which the odor was dissolved, was used as a control. The behavior of the animals was documented by a video recording. The time and frequency animals spent interacting with the odor delivery stick (investigation zone <2 cm) was analyzed.

5.6 Virus injections

Different viral injection into the LC region or olfactory bulb were carried out in this study. In short, mice were anesthetized with a mixture of Medetomidin, Midazolam and Fentanyl at 0.5, 5 and 0.05 mg/kg body weight respectively. Dexamethason was injected i.p. at 100 mg/kg to reduce inflammatory responses. Subsequently mice got headfixed in a stereotactic frame. The skin was cut vertically to expose bregma and lambda.
For injections into the olfactory bulb the following coordinates were used: right OB (AP: 5.00, ML: -1.07, DV: 2.57) and left OB (AP: 4.28, ML: 0.41, DV: 2.45). For injection into the LC region the following coordinates were used: left LC (AP: -5.44, ML: -0,89, DV: 4.07) and right LC (AP: -5.44, ML: -0,99, DV: 3.99).
The Neurostar surgical robot was then used to drill the marked positions until the skull disk could be removed. PBS was always applied from this point forward to avoid drying out. The dura mater was removed before the hamilton syringe was lowered into the brain to the respective position. After all surgeries mice received 5 mg/kg Enrofloxacin as an antibiotic, 25 mg/kg Carprofen to reduce inflammation and 0.1 mg/kg Buprenorphin as an analgesic. A mixture of Atipamezol and Flumazenil (2.5 and 0.5 mg/kg) was used to antagonize the anesthesia. All animals were closely monitored the days after surgery to ensure recovery without complications.

5.6.1 AAV5-Flex-Ef1α-eNpHR3.0-EYFP / AAV-5-Flex-Ef1α-EYFP

Optogenetic neuronal inhibition of LC neurons was achieved by the use of a halorhodopsin from natronomonas (NpHR). It is a chloride-specific light-activated ion pump activated by green light wavelengths of approximately 520 nm. Light activation of NpHR leads to an influx of chloride ions causing the cell to hyperpolarize, and thereby beeing inhibited, not able to generate action potentials. eNpHR3.0 is the latest version of halorhodopsins having an additional potassium channel (Kir2.1) which makes it localize to the cell's membrane, instead of the endoplasmic reticulum as in the earlier versions [247]. AAV5-Flex-Ef1α-eNpHR3.0-EYFP was injected bilaterally into the LC of 3-month-old Dbh-Cre mice. In Dbh-Cre positive LC neurons the flex switches on and inserts eNpHR3.0 under the neuron specific promotor Ef1α. ENpHR3.0 is flagged with the fluorophor EYFP for post-hoc virus expression validation. As a control virus, AAV-5-Flex-Ef1α-EYFP was injected.

5.6.2 AAV-hSyn-DIO-h3MDGs / AAV1-Syn-GCamp8f

Chemogenetic activation of LC neurons was carried out to investigate if an increase in noradrenaline release could rescue the impaired olfaction in APP$^{\text{NL-G-F}}$ $\times$ Dbh-Cre mice. 5-month-old mice were bilaterally injected in the LC with the virus AAV-hSyn-DIO-h3MDGs or the control virus AAV1-Syn-GCamp8f. H3MDGs is an excitatory ligand gated G-protein coupled receptor that gets inserted into LC neurons under the Cre recombinase and neuronal promotor hSyn. H3MDGs signals through the Gas G-protein that activates neurons by increasing intracellular cyclic AMP concentrations, when activated by its ligand CNO. In vivo, mice were injected i.p. with 1 mg/kg CNO, 30 min prior to the buried food test. For patch clamp recordings, a concentration of 3 µM was used.

5.6.3 AAV5-Flex-hSyn1-APP$^{\text{NL-G-F}}$-P2A-HA / AAV-5-Flex-Ef1α-EYFP

To investigate APP$^{\text{NL-G-F}}$ expression exclusively in the LC, we designed a custom-build Cre-dependent AAV virus. It is a mammalian FLEX conditional gene expression AAV virus (Cre-on) with the full vector name: pAAV[FLEXon]-SYN1>LL:rev(hAPP(KM670/671NL, I716F)/P2A/HA):rev(LL):WPRE. It has a size of 6902 base pairs. The inserted ORF: hAPP(KM670/671NL, I716F)/P2A/HA is flanked by two LoxP sides and two

LX2272 sides. In the presence of Cre, the LoxP and Lox2272 sites undergo recombination with the other LoxP / Lox2272 sites respectively which results in the insertion of the ORF. The virus is flagged with an HA-tag, a surface glycoprotein, for post-hoc virus expression validation.

5.7 In vivo noradrenaline release measurement ($GRAB_{NE}$)

5.7.1 Stereotactic surgery and chronic olfactory bulb window

To study pathology dependent noradrenaline release in the olfactory bulb, 10-11-week-old $APP^{NL\text{-}G\text{-}F}$ and C57BL/6J control animals (n=3) were injected with the norepinephrine sensor pAAV-hSyn-$GRAB_{NE1m}$ into the centre of the olfactory bulb (450 nl at 45 nl/min) at a depth of 400 μm. The steroeotactic surgery followed then same procedure as described above under virus injection. Additional to the virus injection, mice were fitted with a cranial window. Therefore, surface edging was performed by scoring the skull lightly with a scalpel and applying a UV light curing mildly corrosive agent (IBond Self Etch, Kulzer 66046243). A 3 mm circular cover slip was inserted over the craniotomy area. The window was fixed in place with tissue adhesive glue (Surgibond tissue adhesive, Praxisdienst, 190740). The entire area with exposed skull was subsequently filled with dental cement (Gradia Direct Flo BW, Spree Dental, 2485494) and a headbar suitable for the later utilized two-photon microscope quickly placed over the window. The cement was cured with UV.

5.7.2 2-Photon imaging

One month after the surgery all mice were trained on the wheel used for awake in vivo imaging, their windows cleaned and the injection site checked for expression. A delivery method for a vanilla scent was established by combining a tube connected to a picospritzer system (PSES-02DX) with a vial containing vanilla aroma (Butter-Vanille, Dr. Oetker, 60-1-01-144800). The tube opening was placed at a fixed distance of roughly 4 cm in front of the mouse and a vacuum pump placed slightly behind the head to insure quick dispersion of the scent after an airpuff was delivered. The two-photon microscope system was the Femptonix system ATLAS with a Coherent Chameleon tunable laser at 920 nm.

Three locations were imaged per mouse at depths between 30 μm and 60 μm below the surface with an 16x objective. Over three minutes a z-stack of 120x120x30 μm with a pixel size of 0.22 μm and a z step of 1 μm was recorded at 1.13 Hz. After one minute 10 seconds of a vanilla delivering airpuff was administered. After each three-minute recording 20 minutes of waiting time before the subsequent recording ensured the dispersion of the odor insight the setup.

For an additional long term trial, one WT mouse was imaged for 18 minutes with the above mentioned settings. Here, vanilla airpuffs at 10 seconds of length were applied at 5, 10 and 15 minutes.

For analysis, the recordings were loaded into Fiji and each z-stack projected with a summation of all 30 slices. Afterwards the EZCalcium Motion Correction (based on NoRMCorre)(PMID: 32499682) was used to reduce motion artifacts to a minimum. The motion corrected files were again imported with Fiji and a z-axis profile created and exported. For each individual recording the frame brightness was normalized to the average of the baseline frames 20-67 before the vanilla airpuff and the average of three adjusted curves calculated. The first 20 frames were removed to account for inconsistencies at the start of each recording, such as startling of the animal. Heatmaps were created with the Python Seaborn distribution, all other graphs were plotted with GraphPad Prism 9.

5.8 Noradrenaline Elisa

In order to measure potential difference in the noradrenaline concentration between C57BL/6J mice and $APP^{NL\text{-}G\text{-}F}$ mice, a noradrenaline ELISA was carried out. Mice were deeply anesthetized and perfused with PBS and their brain rapidly removed. The olfactory bulb was dissected and snap frozen using liquid nitrogen. The tissue was homogenized in 0.01 M HCl in the presence of 0.15 mM EDTA and 4 mM sodium metabisulfite, before being processed with an ELISA kit (BA E-5200) according to the manufacturer's protocol.

5.9 Microglia isolation

Primary microglia were isolated from the olfactory bulb of 2-month-old C57BL/6J and $APP^{NL\text{-}G\text{-}F}$ mice using MACS technology (Miltenyi Biotec) according to manufacturer's instructions. Briefly, mice were perfused with PBS and the brain washed in ice cold HBSS (Gibco) supplemented with 7 mM HEPES (Gibco). To maintain cellular viability and RNA quality, samples and buffers were kept on ice throughout the procedure. Olfactory bulbs were separated from the brain and the meninges removed under a dissection microscope using fine forceps. Chopped tissue pieces were incubated with digestion medium D-MEM/GlutaMax high glucose and pyruvate (Gibco) supplemented with 20 U papain per ml (Sigma P3125) and 0.01 % L-Cysteine (Sigma) for 15 min at 37°C in a water bath. Subsequently, enzymatic digestion was stopped using blocking medium 10 % heat-inactivated FBS (Sigma) in D-MEM/GlutaMax high glucose and pyruvate. Mechanical dissociation was gently but thoroughly performed by using three fire-polished, BSA-coated glass Pasteur pipettes with decreasing diameter. To achieve variable diameters and smooth edges, a Bunsen burner was used. Subsequently, microglia were magnetically labeled with CD11b microbeads (Miltenyi Biotec, 130-097-678) in MACS buffer (0.5 % BSA, 2 mM EDTA in 1x PBS, sterile filtered) and the suspension loaded onto a pre-washed LS-column (Miltenyi Biotec, 130-042-401). Following washing with 3x1 ml MACS buffer, magnetic separation resulted in a CD11b enriched and a CD11b depleted fraction. To increase purity further, the microglia-enriched fraction was loaded onto another LS-column. Total numbers of obtained microglia fractions were quantified using C-Chip chambers (Nano EnTek, DHC-N01). Isolated primary microglia were washed twice with 1x PBS (Gibco) and immediately processed for sequencing.

5.10 Phagocytosis assay

5.10.1 Isolation of Synaptic Protein

Synaptic Protein was enriched using the Syn-PER™ Synaptic Protein Extraction Reagent (Thermo Fisher) according to manufacturer's protocol. In brief, fresh brains from C57BL/6J mice at 4 months of age were isolated and homogenized in 10mL per gram of brain tissue of

Syn-PER™ reagent substituted with protease and phosphatase inhibitor. The homogenate was then centrifuged at 1200 rpm at 4°C for 10 minutes to separate the nuclear fraction (pellet) from the cytosolic fraction (supernatant). The supernatant containing the synaptic fraction was then transferred into a new tube and spun at 15.000 rpm at 4°C for 20 minutes. The supernatant was aspirated and the pellet of synaptic protein was resuspended in 1mL of Syn-PER™ reagent containing 5 % (v/v) DMSO per gram tissue originally used. Synaptosome extracts were then stored at -80°C before further usage.

5.10.2 Flourescent labeling with pHrodo™

Synaptic Protein was labeled with the pHrodo™ Red succinimidyl ester (Thermo Fisher Scientific), which emits a red fluorescent signal only in acidic environments, therefore signaling when substrates where uptaken into phagosomes. Labeling was performed as previously described [248]. In brief, synaptic protein was washed in 100 mM sodium bicarbonate, pH 8.5 and spun down (17.000 rpm for 4 min at 4°C). pHrodo™ dye was dissolved in 150 μL DMSO per 1 mg dye to a concentration of 10 mM. The pHrodo™ stock solution was added to the synaptic protein at a concentration 1 μl pHrodo per 1 mg of synaptic protein. After incubating the reaction at room temperature for 2 hours, protected from light, the labeled protein was washed twice in DPBS and spun down (at 17.000 rpm for 4 min at 4°C). After resuspending synaptic protein with 100 mM sodium bicarbonate, pH 8.5 to a concentration of 1000 μg/ml, it was aliquoted and stored at -80°C before usage.

5.10.3 Phgocytotic uptake assay

Primary microglia were cultured in tissue culture treated 96-well plates in microglia-medium adding freshly 10 ng/ml GM-CSF (R&D Systems) for three days in vitro (DIV) at 37°C, 5 % CO2, changing medium at DIV 1. For the phagocytic uptake assay, medium was replaced with medium in which pHrodo™ labeled synaptic protein was resuspended at the desired concentration (2.5 μg/mL). For the Cytochalasin D control, cells were treated with 10 μM CytoD (Sigma) for 30 minutes, before adding medium with labeled synaptic protein and CytoD. Immediately after adding the substrates the cells were placed in an Incucyte™ S3 Live-Cell Analysis System (Sartorius). Scans were performed every hour

with 20x maginification and both phase contrast and red fluorescent channels, acquiring a minimum of three images per well and scan. Quantification was done using the cell-by-cell adherent analysis (Segmentation adjustment: 0.7; Cleanup: 150 μm2 Hole Fill, Cell Detection sensitivity: 0.7, Cell Contrast: 2, Cell Morphology: 4, Area: 150-1500 μm2). Phagocytic index was calculated using the total integrated intensity (RCU x μm^2/Image) normalized to the number of cells per image.

5.11 RNA sequencing and Bioinformatics

RNA was isolated from microglial cell pellets using the RNeasy Plus Micro kit (Qiagen, 74034). Briefly, samples were lysed with RLT Plus lysis buffer containing beta-Mercaptoethanol, genomic DNA was removed by passing the lysate through gDNA eliminator columns, and the eluate was applied to RNeasy spin columns. Contaminants were removed with repeated Ethanol washes before RNA was eluted with 20 µL molecular grade water. All steps were carried out automatically on a Qiacube machine. RNA was quantified on a Qubit Fluorometer (Invitrogen, Q33230) and 6 ng of total RNA were used as input for library preparation with the Takara SMART-seq Stranded kit (Takara, 634444) following the manufacturer's instructions. Fragmentation time was kept at 6 minutes and AMPure XP beads (Beckman Coulter, A63880) were used for all clean-up steps. Library QC using a Bioanalyzer revealed average insert sizes around 350 bps. The molarity of each of the 16 libraries was determined by using the ddPCR Library Quantification Kit for Illumina TruSeq (Bio-Rad, 1863040) according to the manufacturer's instructions. Libraries were then diluted to 4 nM and pooled in an equimolar fashion. Paired-end sequencing was carried out for 150 cycles on a NextSeq 550 sequencer (Illumina, 20024907) using a High-Output flow cell. After sample demultiplexing, reads were aligned using STAR v2.7.8 to a customized genome based on the GRCm39 assembly and the gencode vM32 primary annotation that additionally contained sequences and annotations for the human APP gene. Group assignments were verified by manually inspecting alignments to the (human) APP sequence and checking for presence of the NL-, G- and F- mutations in transgenic animals. The count matrix produced by STAR v2.7.8 was used as an input for differential expression testing using edgeR. The count matrix was filtered to retain genes with at least

5 counts in at least 50 % of samples and quasi-likelihood tests were conducted after fitting appropriate binomial models. Differential expression was considered significant if FDR <0.1 and if the absolute log-fold-change exceeded 0.5. Gene lists were annotated with the enrichR package. All analyses made heavy use of the tidyverse and ggplot2 packages and were performed on a server running Arch Linux, R version 4.3.2 and Rstudio Server 2023.03.0.

5.12 Small animal TSPO μPET

All small animal positron emission tomography (μPET) procedures followed an established standardized protocol for radiochemistry, acquisition and post-processing [249]. In brief, [18F]GE-180 TSPO μPET with an emission window of 60-90 mins post injection was used to measure microglial activity. $APP^{NL\text{-}G\text{-}F}$ and age-matched C57BL/6J mice were studied at ages between 2 and 12 months. All analyses were performed by PMOD (V3.5, PMOD technologies, Basel, Switzerland). Normalization of injected activity was performed by the previously validated myocardium correction method [250]. TSPO μPET estimates deriving from predefined volumes of interest of the Mirrione atlas were used: olfactory bulb (22.9 mm^3) and cortical composite (144.9 mm^3) [251]. Intensity normalization of all PET images was performed by calculation of standardized uptake value ratios (SUVr) using the cerebellum as an established pseudo-reference tissue for TSPO-PET. Associations of TSPO μPET estimates with age and genotype as well as the interaction of age and genotype were tested by a linear regression model.

5.13 Human TSPO-PET imaging acquisition and analysis

For PET imaging an established standardized protocol was used [252, 253]. All participants were scanned at the Department of Nuclear Medicine, LMU Munich, using a Biograph 64 PET/CT scanner (Siemens, Erlangen, Germany). Before each PET acquisition, a low-dose CT scan was performed for attenuation correction. Emission data of TSPO-PET were acquired from 60 to 80 minutes after the injection of 187 ± 11 MBq [18F]GE-180 as an intravenous bolus, with some patients receiving dynamic PET imaging over 90 minutes.

The specific activity was >1500 GBq/μmol at the end of radiosynthesis, and the injected mass was 0.13 ± 0.05 nmol. All participants provided written informed consent before the PET scans. Images were consistently reconstructed using a 3-dimensional ordered subsets expectation maximization algorithm (16 iterations, 4 subsets, 4 mm gaussian filter) with a matrix size of 336 × 336 × 109, and a voxel size of 1.018 × 1.018 × 2.027 mm. Standard corrections for attenuation, scatter, decay, and random counts were applied. 60-80 min post injection, images of all patients and controls were analysed.

5.14 Histology: Human brain tissue

Human brain tissue from 7 healthy control subjects, 6 prodromal AD subjects and 6 AD patients was provided from the Munich brain bank. Usage of this tissue was approved by the Ethics Committee of the Ludwig-Maximilians University Munich. Demographic details of the subjects are listed in table 3. Paraffin embedded brain sections (5 μm) of the olfactory bulb were cut in a horizontal plane, using a microtome (Leica SM2010R) and mounted on glass slides until further processing. Sections were deparaffinized with xylene and rehydrated through a series of descending alcohol concentrations. For the staining, an automated IHC/SH slice staining system (Ventana BenchMark ULTRA) was used. On separate slices, NET 1:200, Aβ 1:5000 and Tau 1:400 was stained and visualized with an upright Bridgefield microscope. Each four 20x magnification pictures per subject were acquired and analyzed in ImageJ Fiji regarding their perceptual density of LC axons.

5.15 Human olfactory identification test

For detecting decreased olfactory performance due to neurodegenerative diseases, the "Sniffin' Sticks - Screening 12" test was employed. Developed in collaboration with the Working Group "Olfactology and Gustology" of the German Society for Otorhinolaryngology, Head and Neck Surgery, the test provides a preliminary diagnostic orientation and can be conveniently used in everyday settings. It classifies individuals as anosmics (no olfactory ability), hyposmics (reduced olfactory ability), or normosmics (normal olfactory ability). The 12 pens contain health-safe aromas, mostly used in food as flavorings, which

participants must recognize. Their advantage over natural aromas includes longer shelf life and known qualitative composition. For the testing procedure, only one cap from each pen is removed at a time to expose the participant to the aroma. To maintain the aroma's integrity and the pen's longevity, the cap is immediately replaced after exposure. The participants are informed about the testing method and are presented with 12 familiar scents. Both nostrils are accessed simultaneously. Each scent is presented with a multiple-choice format, where participants choose one of four terms that best describe the scent, even if they perceive no smell. During testing, no feedback is provided to ensure unbiased responses. Demographic details of the subjects are listed in table 4.

5.16 Statistics

All statistical analyses were performed in GraphPadPrism (version 9.5 and 10.1.1). For the comparison of two groups the two tailed unpaired Student's t-test was used. When comparing more than two groups a one-way ANOVA was applied, followed by Tukey's or Šidák multiple comparison test. All data are reported as mean ± standard error of the mean (SEM). Significance was set at $p<0.05$ and expressed as $^{*}p<0.05$, $^{**}p<0.01$, $^{***}p<0.001$ and $^{****}p<0.001$. Statistical details of every experiment are explained in the figure legends.

Abbreviations

AAV	Adeno-assocaited virus
ACSF	Artificial cerebrospinal fluid
AD	Alzheimer's disease
AHP	Afterhyperpolarization
AICD	Amyloid-precursor-protein intracellular domain
AP	Action potential
ApoE	Apolipoprotein E
APP	Amyloid-precursor-protein
ATP	Adenosine triphosphate
Aβ	Amyloid-beta protein
α7nAChR	α7 nicotinic acetylcholine receptor
BACE1	β-secretase 1
BFT	Buried food test
C	Capacitance
$CaCl^2$	Calcium chloride
CALR	Calreticulin
CD68	Cluster of differentiation 68 protein expressed by monocytes and macrophages
ChAT	Choline Acetyltransferase
CNiFER	Cell-based neurotransmitter fluorescent engineered reporter
CNO	Clozapine-N-oxide

Cre	Cyclization recombination
CSF	Cerebrospinal fluid
CTFβ	C-terminal fragment of amyloid-precursor-protein
CytoD	Cytochalasin D
C1q	Complement component 1
C3b	Complement component 3b
C57BL/6J	C57BL mice, substrain 6
C83	Carboxy-terminal fragment
C99	C-terminal fragment of amyloid-precursor-protein
DAM	Disease-associated microglia
DAPI	4',6-diamidino-2-phenylindole
Dbh	Dopamin beta hydroxylase
DDC	DOPA-decarboxylase
DE	Delayed excitation
DG	Dentate gyrus
DREADD	Designer-receptor exclusively activated by designed drugs
DOPEGAL	3,4-Dihydroxyphenylglycolaldehyde
Ef1α	Human elongation factor-1 alpha promotor
EGTA	Ethylene glycol-bis(β-aminoethyl ether)-N,N,N',N'-tetraacetic acid
ELISA	Enzyme-linked Immunosorbent Assay
eNpHR	Enhanced Halorhodopsin from Natronomonas
EPL	External plexiform layer

EYFP	Enhanced yellow flourescent protein
Flex	Flip-Excision
G	Granular cell
Gal3	Galactin 3
Gas6	Growth-arrest-specific gene-6
GL	Glomerular layer
GO	Gene ontology
$GRAB_{NE}$	Genetically endocded flourescent sensor for norepinephrine
GRL	Granular cell layer
HA-tag	Hemagglutinin tag
HC	Healthy control
HEPES	4-(2-hydroxyethyl)-1-piperazineethanesulfonic acid
Het	Heterozygous
hM3Dq	Human M3 muscarinic, excitatory ligand-gated G-protein-coupled receptor
Hom	Homozygous
hSyn	Human synapsin 1 promotor
Hz	Hertz (Unit of frequency, 1/s)
Iba1	Ionized calcium-binding adapter molecule 1
i.p.	Intraperitoneal
IPL	Internal plexiform layer
IR	Input resistance

KCl	Potassium
Kv	Voltage-gated potassium channel
LC	Locus coeruleus
MCI	Mild cognitive impairment
MCL	Mitral cell layer
MFG-E8	Milk fat globule-EGF factor 8 protein
$MgCl_2$	Magnesium chloride
mOsm	Milliosmole (osmotic concentration, number of moles/liter)
mPFC	Medial prefrontal cortex
MVB	Multivesicular body
Na	Sodium
NA or NE	Noradrenaline or norepinephrine
$NaHCO_3$	Sodium hydrogencarbonate
NaH_2PO4_4	Sodium dihydrogen phosphate
NET	Norepinephrine transporter
NFT	Neurofibrillary tangles
OB	Olfactory bulb
ONL	Olfactory nerve layer
OSN	Olfactory sensory neuron
pAD	Prodromal AD
PET	Positron emission tomography
PG	Periglomerular cell

Pir	Piriform cortex
PS	Phosphatidylserine
ROS	Reactive oxygen species
SCD	Subjective cognitive decline
SERT	Serotonin Transporter
SK	Calcium-activated potassium channel
SUVr	Standardized uptake value ratio
S1	Primary somatosensory cortex
T	Tufted cell
Tau	Tubulin associated unit
TH	Tyrosin hydroxylase
TREM2	Triggering receptor expressed on myeloid cells 2
TSPO	Translocator protein, expressed on outer mitochondrial membrane
TSPO-KO	Translocator protein knock-out
τ	Time constant tau
WT	Wild-type (C57BL/6J mice)

List of Figures

List of Tables

References

1. Meyer, C., Niedermeier, T., Feyen, P., *et al.* Noradrenergic axon loss drives olfactory dysfunction in Alzheimer's disease. *Res. Sq.* (2024).

2. Hardy, J., Selkoe, D. J., Hardy, J., *et al.* The amyloid hypothesis of Alzheimer's disease: Progress and problems on the road to therapeutics. *Science* **297,** 353–356 (2016).

3. Hippius, H. & Neundörfer, G. The discovery of Alzheimer's disease. *Dialogues Clin. Neurosci.* **5,** 101–108 (2003).

4. Beyreuther, K. & Masters, C. L. Amyloid precursor protein (APP) and βA4 amyloid in the etiology of Alzheimer's disease: Precursor-product relationships in the derangement of neuronal function. *Brain Pathol.* **1,** 241–251 (1991).

5. Hardy, J. & Allsop, D. Amyloid deposition as the central event in the aetiology of Alzheimer's disease. *Trends Pharmacol. Sci.* **12,** 383–388 (1991).

6. Boyd, R. J., Avramopoulos, D., Jantzie, L. L., *et al.* Neuroinflammation represents a common theme amongst genetic and environmental risk factors for Alzheimer and Parkinson diseases. *J. Neuroinflammation* **19,** 1–20 (2022).

7. Zhang, Y., Chen, H., Li, R., *et al.* Amyloid β-based therapy for Alzheimer's disease: challenges, successes and future. *Signal Transduct. Target. Ther.* **8,** 1–26 (2023).

8. Ameen, T. B., Kashif, S. N., Abbas, S. M. I., *et al.* Unraveling Alzheimer's: the promise of aducanumab, lecanemab, and donanemab. *Egypt. J. Neurol. Psychiatry Neurosurg.* **60,** 1–12 (2024).

9. Mahase, E. Lecanemab: European drug agency rejects Alzheimer's drug amid debate over efficacy and safety. *BMJ* **386** (2024).

10. European-Medicine-Agency. *Alzheimer patient Leqembi recommended for treatment of early Alzheimer's disease, year = 2024, url = https://www.ema.europa.eu/en/news/leqembi-recommended-treatment-early-alzheimers-disease, urldate = 2024-12-02*

11. Müller, U. C., Deller, T. & Korte, M. Not just amyloid: Physiological functions of the amyloid precursor protein family. *Nat. Rev. Neurosci.* **18,** 281–298 (2017).

12. Chow, V. W., Mattson, M. P., Wong, P. C., *et al.* An overview of APP processing enzymes and products vivian. *Neuromolecular Med.* **12** (2010).

13. Zhang, Y.-w., Thompson, R., Zhang, H., *et al.* APP processing in Alzheimer's disease. *Mol. Brain* **4,** 1–13 (2011).

14. Saito, T., Matsuba, Y., Mihira, N., *et al.* Single App knock-in mouse models of Alzheimer's disease. *Nat. Neurosci.* **17,** 661–663 (2014).

15. Selkoe, D. J. Alzheimer's disease : Genes, proteins, and therapy. **81,** 741–760 (2001).

16. Gouras, G. K., Almeida, C. G. & Takahashi, R. H. Intraneuronal Aβ accumulation and origin of plaques in Alzheimer's disease. *Neurobiol. Aging* **26,** 1235–1244 (2005).

17. Billings, L. M., Oddo, S., Green, K. N., *et al.* Intraneuronal Aβ causes the onset of early Alzheimer's disease-related cognitive deficits in transgenic mice. *Neuron* **45,** 675–688 (2005).

18. Youmans, K. L., Tai, L. M., Kanekiyo, T., *et al.* Intraneuronal Aβ detection in 5xFAD mice by a new Aβ-specific antibody. *Mol. Neurodegener.* **7,** 1–14 (2012).

19. D'Andrea, M. R., Nagele, R. G., Wang, H. Y., *et al.* Consistent immunohistochemical detection of intracellular β-amyloid42 in pyramidal neurons of Alzheimer's disease entorhinal cortex. *Neurosci. Lett.* **333,** 163–166 (2002).

20. Gouras, G. K., Tsai, J., Naslund, J., *et al.* Intraneuronal Aβ42 accumulation in human brain. *Am. J. Pathol.* **156,** 15–20 (2000).

21. Zhao, J., Liu, X., Xia, W., *et al.* Targeting amyloidogenic processing of APP in Alzheimer's disease. *Front. Mol. Neurosci.* **13,** 1–17 (2020).

22. Wesén, E., Jeffries, G. D., Dzebo, M. M., *et al.* Endocytic uptake of monomeric amyloid-β peptides is clathrin- and dynamin-independent and results in selective accumulation of Aβ(1-42) compared to Aβ(1-40). *Sci. Rep.* **7,** 1–14 (2017).

23. Kelly, L., Seifi, M., Ma, R., *et al.* Identification of intraneuronal amyloid beta oligomers in locus coeruleus neurons of Alzheimer's patients and their potential impact on inhibitory neurotransmitter receptors and neuronal excitability. *Neuropathol. Appl. Neurobiol.* **47,** 488–505 (2021).

24. Pensalfini, A., Albay, R., Suhail Rasool, *et al.* Intracellular amyloid and the neuronal origin of Alzheimer neuritic plaques. *Neurobiol. Dis.* **0,** 53–61 (2014).

25. Wirths, O., Multhaup, G., Czech, C., *et al.* Intraneuronal Aβ accumulation precedes plaque formation in β-amyloid precursor protein and presenilin-1 double-transgenic mice. *Neurosci. Lett.* **306,** 116–120 (2001).

26. Wirths, O., Weis, J., Kayedc, R., *et al.* Age-dependent axonal degeneration in an Alzheimer mouse model. *Neurobiol. Aging* **28,** 1689–1699 (2007).

27. Nagele, R. G., D'Andrea, M. R., Anderson, W. J., *et al.* Intracellular accumulation of β-amyloid1-42 in neurons is facilitated by the α7 nicotinic acetylcholine receptor in Alzheimer's disease. *Neuroscience* **110,** 199–211 (2002).

28. Almeida, C. G., Takahashi, R. H. & Gouras, G. K. β-Amyloid accumulation impairs multivesicular body sorting by inhibiting the ubiquitin-proteasome system. *J. Neurosci.* **26,** 4277–4288 (2006).

29. Willén, K., Edgar, J. R., Hasegawa, T., *et al.* Aβ accumulation causes MVB enlargement and is modelled by dominant negative VPS4A. *Mol. Neurodegener.* **12,** 1–18 (2017).

30. Takahashi, R. H., Milner, T. A., Li, F., *et al.* Intraneuronal Alzheimer Aβ42 accumulates in multivesicular bodies and is associated with synaptic pathology. *Am. J. Pathol.* **161,** 1869–1879 (2002).

31. Schaefer, P. M., Von Einem, B., Walther, P., *et al.* Metabolic characterization of intact cells reveals intracellular amyloid beta but not its precursor protein to reduce mitochondrial respiration. *PLOS ONE* **11,** 1–23 (2016).

32. Caspersen, C., Wang, N., Yao, J., *et al.* Mitochondrial Aβ: a potential focal point for neuronal metabolic dysfunction in Alzheimer's disease. *FASEB J.* **19,** 2040–2041 (2005).

33. Manczak, M., Anekonda, T. S., Henson, E., *et al.* Mitochondria are a direct site of Aβ accumulation in Alzheimer's disease neurons: Implications for free radical generation and oxidative damage in disease progression. *Hum. Mol. Genet.* **15,** 1437–1449 (2006).

34. Christensen, D. Z., Kraus, S. L., Flohr, A., *et al.* Transient intraneuronal Aβ rather than extracellular plaque pathology correlates with neuron loss in the frontal cortex of APP/PS1KI mice. *Acta Neuropathol.* **116,** 647–655 (2008).

35. Casas, C., Sergeant, N., Itier, J. M., *et al.* Massive CA1/2 neuronal loss with intraneuronal and N-terminal truncated Aβ42 accumulation in a novel Alzheimer transgenic model. *Am. J. Pathol.* **165,** 1289–1300 (2004).

36. Echeverria, V., Ducatenzeiler, A., Dowd, E., *et al.* Altered mitogen-activated protein kinase signaling, tau hyperphosphorylation and mild spatial learning dysfunction in transgenic rats expressing the β-amyloid peptide intracellularly in hippocampal and cortical neurons. *Neuroscience* **129,** 583–592 (2004).

37. Leon, W. C., Canneva, F., Partridge, V., *et al.* A novel transgenic rat model with a full Alzheimer's-like amyloid pathology displays pre-plaque intracellular amyloid-β-associated cognitive impairment. *J. Alzheimer's Dis.* **20,** 113–126 (2010).

38. España, J., Giménez-Llort, L., Valero, J., *et al.* Intraneuronal β-amyloid accumulation in the amygdala enhances fear and anxiety in Alzheimer's disease transgenic mice. *Biol. Psychiatry* **67,** 513–521 (2010).

39. Pigino, G., Morfini, G., Atagi, Y., *et al.* Disruption of fast axonal transport is a pathogenic mechanism for intraneuronal amyloid beta. *Proc. Natl. Acad. Sci. U. S. A.* **106,** 5907–5912 (2009).

40. Gouras, G. K., Tampellini, D., Takahashi, R. H., *et al.* Intraneuronal β-amyloid accumulation and synapse pathology in Alzheimer's disease. *Acta Neuropathol.* **119,** 523–541 (2010).

41. Weingarten, M. D., Lockwood, A. H., Hwo, S.-y., *et al.* A protein factor essential for microtubule assembly. **72,** 1858–1862 (1975).

42. Alonso, A. D. C., Zaidi, T., Grundke-Iqbal, I., *et al.* Role of abnormally phosphorylated tau in the breakdown of microtubules in Alzheimer disease. *Proc. Natl. Acad. Sci. U. S. A.* **91,** 5562–5566 (1994).

43. Iqbal, K., Grundke-iqbal, I., Zaidi, T., *et al.* Defective brain microtubule assembly in Alzheimer's disease. *The Lancet,* 421–426 (1986).

44. Ubeda-Bañon, I., Saiz-Sanchez, D., Flores-Cuadrado, A., *et al.* The human olfactory system in two proteinopathies: Alzheimer's and Parkinson's diseases. *Transl. Neurodegener.* **9,** 1–20 (2020).

45. Braak, H. & Braak, E. Neuropathological stageing of Alzheimer-related changes. *Acta Neuropathol.* **82,** 239–259 (1991).

46. Kovács, T., Cairns, N. J. & Lantos, P. L. Olfactory centres in Alzheimer's disease: olfactory bulb is involved in early Braak's stages. *Neuroreport* **12,** 285–288 (2001).

47. Ghosh, A., Torraville, S. E., Mukherjee, B., *et al.* An experimental model of Braak's pretangle proposal for the origin of Alzheimer's disease: The role of locus coeruleus in early symptom development. *Alzheimer's Res. Ther.* **11,** 1–17 (2019).

48. Lawson, L. J., Perry, V. H., Dri, P., *et al.* Heterogeneity in the distribution and morphology of microglia in the normal adult mouse brain. *Neuroscience* **39,** 151–170 (1990).

49. Stopper, L., Bălşeanu, T. A., Cătălin, B., *et al.* Microglia morphology in the physiological and diseased brain – From fixed tissue to in vivo conditions. *Rom. J. Morphol. Embryol.* **59,** 7–12 (2018).

50. Tejera, D. & T. Heneka, M. Microglia in Alzheimer's disease: The good, the bad and the ugly. *Curr. Alzheimer Res.* **13,** 370–380 (2016).

51. Garaschuk, O. & Verkhratsky, A. *Microglia: Methods and Protocols* 1–340. ISBN: 9781493996575 (Springer, 2019).

52. Hopperton, K. E., Mohammad, D., Trépanier, M. O., *et al.* Markers of microglia in post-mortem brain samples from patients with Alzheimer's disease: A systematic review. *Mol. Psychiatry* **23,** 177–198 (2018).

53. Bonsack, F. & Sukumari-Ramesh, S. TSPO: An evolutionarily conserved protein with elusive functions. *Int. J. Mol. Sci.* **19,** 1–13 (2018).

54. Yu, F., Wang, Y., Stetler, A. R., *et al.* Phagocytic microglia and macrophages in brain injury and repair. *CNS Neurosci. Ther.* **28,** 1279–1293 (2022).

55. Peet, G., Bennett, F. C. & Bennett, M. L. Please eat (only part) of me: synaptic phosphatidylserine cues microglia to feast. *EMBO J.* **39,** 2–4 (2020).

56. Li, W. Eat-me signals: Keys to molecular phagocyte biology and "appetite" control. *J. Cell Physiol.* **227,** 1291–1297 (2012).

57. Kurematsu, C., Sawada, M., Ohmuraya, M., *et al.* Synaptic pruning of murine adult-born neurons by microglia depends on phosphatidylserine. *J. Exp. Med.* **219,** 1–22 (2022).

58. Nagata, S., Suzuki, J., Segawa, K., *et al.* Exposure of phosphatidylserine on the cell surface. *Cell Death Differ.* **23,** 952–961 (2016).

59. Brown, G. C. & Neher, J. J. Microglial phagocytosis of live neurons. *Nat. Rev. Neurosci.* **15,** 209–216 (2014).

60. Poe, G. R., Foote, S., Eschenko, O., *et al.* Locus coeruleus: a new look at the blue spot. *Nat. Rev. Neurosci.* **21,** 644–659 (2020).

61. Reil, J. Untersuchungen über den Bau des grossen Gehirns im Menschen. *Archives of Physiology and Biochemistry* (1809).

62. Baker, G, Hornung, P & Halasz, P. The human locus coeruleus complex: an immunohistochemical and three dimensional reconstruction study. *Exp. brain Res.* **77,** 257–270 (1989).

63. Samuels, E. & Szabadi, E. Functional neuroanatomy of the noradrenergic locus coeruleus: Its roles in the regulation of arousal and autonomic function part I: Principles of functional organisation. *Curr. Neuropharmacol.* **6,** 235–253 (2008).

64. Sharma, Y., Xu, T., Graf, W. M., *et al.* Comparative anatomy of the locus coeruleus in humans and nonhuman primates. *J. Comp. Neurol.* **518,** 963–971 (2010).

65. Mouton, P. R., Pakkenberg, B., Gundersen, H. J. G., *et al.* Absolute number and size of pigmented locus coeruleus neurons in young and aged individuals. *J. Chem. Neuroanat.* **7,** 185–190 (1994).

66. Schwarz, L. A. & Luo, L. Organization of the locus coeruleus-norepinephrine system. *Curr. Biol.* **25,** R1051–R1056 (2015).

67. Sara, S. J. The locus coeruleus and noradrenergic modulation of cognition. *Nat. Rev. Neurosci.* **10,** 211–223 (2009).

68. Grzanna, R. & Molliver, M. E. The locus coeruleus in the rat: An immunohistochemical delineation. *Neuroscience* **5,** 21–40 (1980).

69. Swanson, L. W. The locus coeruleus: A cytoarchitechtonic, golgi, immunhistochemical study in the albino rat. **110,** 39–56 (1976).

70. McKinney, A., Hu, M., Hoskins, A., *et al.* Cellular composition and circuit organization of the locus coeruleus of adult mice. *Elife* **12,** 1–30 (2023).

71. Szabadi, E. Functional neuroanatomy of the central noradrenergic system. *J. Psychopharmacol.* **27,** 659–693 (2013).

72. Theofilas, P., Dunlop, S., Heinsen, H., *et al.* Turning on the light within: Subcortical nuclei of the isodentritic core and their role in Alzheimer's disease pathogenesis. *J. Alzheimer's Dis.* **46,** 17–34 (2015).

73. Kebschull, J. M., Garcia da Silva, P., Reid, A. P., *et al.* High-throughput mapping of single-neuron projections by sequencing of barcoded RNA. *Neuron* **91,** 975–987 (2016).

74. Breton-Provencher, V. & Sur, M. Active control of arousal by a locus coeruleus GABAergic circuit. *Nat. Neurosci.* **22,** 218–228 (2019).

75. Escanilla, O., Arrellanos, A., Karnow, A., *et al.* Noradrenergic modulation of behavioral odor detection and discrimination thresholds in the olfactory bulb. *Eur. J. Neurosci.* **32,** 458–468 (2010).

76. Manunta, Y. & Edeline, J. M. Noradrenergic induction of selective plasticity in the frequency tuning of auditory cortex neurons. *J. Neurophysiol.* **92,** 1445–1463 (2004).

77. Martins, A. R. & Froemke, R. C. Coordinated forms of noradrenergic plasticity in the locus coeruleus and primary auditory cortex. *Nat. Neurosci.* **18,** 1483–1492 (2015).

78. Navarra, R. L., Clark, B. D., Gargiulo, A. T., *et al.* Methylphenidate enhances early-stage sensory processing and rodent performance of a visual signal detection task. *Neuropsychopharmacol.* **42,** 1326–1337 (2017).

79. Tsetsenis, T., Badyna, J. K., Li, R., *et al.* Activation of a locus coeruleus to dorsal hippocampus noradrenergic circuit facilitates associative learning. *Front. Cell. Neurosci.* **16,** 1–11 (2022).

80. Tully, K. & Bolshakov, V. Y. Emotional enhancement of memory: How norepinephrine enables synaptic plasticity. *Mol. Brain* **3,** 1–9 (2010).

81. Wilmot, J. H., Diniz, C. R., Crestani, A. P., *et al.* Phasic locus coeruleus activity enhances trace fear conditioning by increasing dopamine release in the hippocampus. *Elife* **12,** 1–29 (2024).

82. Kaufman, A. M., Geiller, T. & Losonczy, A. A role for the locus coeruleus in hippocampal CA1 place cell reorganization during spatial reward learning. *Neuron* **105,** 1018–1026 (2020).

83. Kempadoo, K. A., Mosharov, E. V., Choi, S. J., *et al.* Dopamine release from the locus coeruleus to the dorsal hippocampus promotes spatial learning and memory. *Proc. Natl. Acad. Sci. U. S. A.* **113,** 14835–14840 (2016).

84. McGaughy, J., Ross, R. S. & Eichenbaum, H. Noradrenergic, but not cholinergic, deafferentiation of prefrontal cortex impairs attentional set-shifting. *J. Neurosci.* **153,** 63–71 (2008).

85. Reynaud, A. J., Froesel, M., Guedj, C., *et al.* Atomoxetine improves attentional orienting in a predictive context. *Neuropharmacol.* **150,** 59–69 (2019).

86. Bouras, N. N., Mack, N. R. & Gao, W. J. Prefrontal modulation of anxiety through a lens of noradrenergic signaling. *Front. Syst. Neurosci.* **17,** 1–18 (2023).

87. Ferry, B., Roozendaal, B. & McGaugh, J. L. Basolateral amygdala noradrenergic influences on memory storage are mediated by an interaction between β- and α1-adrenoceptors. *J. Neurosci.* **19,** 5119–5123 (1999).

88. Maness, E. B., Burk, J. A., McKenna, J. T., *et al.* Role of the locus coeruleus and basal forebrain in arousal and attention. *Brain Res. Bull.* **188,** 47–58 (2022).

89. Clewett, D. V., Huang, R., Velasco, R., *et al.* Locus coeruleus activity strengthens prioritized memories under arousal. *J. Neurosci.* **38,** 1558–1574 (2018).

90. Aston-Jones, G. & Bloom, F. E. Activity of norepinephrine-containing locus coeruleus neurons in behaving rats anticipates fluctuations in the sleep-waking cycle. *J. Neurosci.* **1,** 876–886 (1981).

91. Clayton, E. C., Rajkowski, J., Cohen, J. D., *et al.* Phasic activation of monkey locus ceruleus neurons by simple decisions in a forced-choice task. *J. Neurosci.* **24,** 9914–9920 (2004).

92. Devilbiss, D. M. & Waterhouse, B. D. Phasic and tonic patterns of locus coeruleus output differentially modulate sensory network function in the awake rat. *J. Neurophysiol.* **105,** 69–87 (2011).

93. Berridge, C. W. & Waterhouse, B. D. The locus coeruleus-noradrenergic system: Modulation of behavioral state and state-dependent cognitive processes. *Brain Res. Rev.* **42,** 33–84 (2003).

94. Foote, S. L., Aston-Jones, G. & Bloom, F. E. Impulse activity of locus coeruleus neurons in awake rats and monkeys is a function of sensory stimulation and arousal. *Proc. Natl. Acad. Sci. U. S. A.* **77,** 3033–3037 (1980).

95. Aston-Jones, G. & Cohen, J. D. An integrative theory of locus coeruleus-norepinephrine function: Adaptive gain and optimal performance. *Annu. Rev. Neurosci.* **28,** 403–450 (2005).

96. Matschke, L. A., Bertoune, M., Roeper, J., *et al.* A concerted action of L- and T-type Ca^{2+} channels regulates locus coeruleus pacemaking. *Mol. Cell. Neurosci.* **68,** 293–302 (2015).

97. Sanchez–Padilla, J., Guzman, J., Ilijic, E., *et al.* Mitochondrial oxidant stress in locus coeruleus is regulated by activity and nitric oxide synthase. *Nat. Neurosci.* **17,** 832–840 (2014).

98. Williams, J. T., North, R. A., Shefner, S. A., *et al.* Membrane properties of rat locus coeruleus neurones. *Neuroscience* **13,** 137–156 (1984).

99. Shibata, R., Nakahira, K., Shibasaki, K., *et al.* A-type K^+ current mediated by the Kv4 channel regulates the generation of action potential in developing cerebellar granule cells. *J. Neurosci.* **20,** 4145–4155 (2000).

100. Andrade, R., Foehring, R. C. & Tzingounis, A. V. The calcium-activated slow AHP: Cutting through the Gordian Knot. *Front. Cell. Neurosci.* **6,** 1–38 (2012).

101. Su, Z. & Cohen, J. Y. Two types of locus coeruleus norepinephrine neurons drive reinforcement learning. *bioRxiv* (2022).

102. Nakamura, S. Some electrophysiological properties of rat locus coeruleus. *J. Physiol.* **267,** 641–658 (1977).

103. Chiti, Z. & Teschemacher, A. G. Exocytosis of norepinephrine at axon varicosities and neuronal cell bodies in the rat brain. *FASEB J.* **21,** 2540–2550 (2007).

104. Séguéla, P., Watkins, K. C., Geffard, M., *et al.* Noradrenaline axon terminals in adult rat neocortex: An immunocytochemical analysis in serial thin sections. *Neuroscience* **35,** 249–264 (1990).

105. Daubner, S. C., Le, T. & Wang, S. Tyrosine hydroxylase and regulation of dopamine synthesis. *Archives of Biochemistry and Biophysics* **508,** 1–12 (2011).

106. Zhang, M. R., Maeda, J., Ogawa, M., *et al.* Development of a new radioligand, N-(5-Fluoro-2-phenoxyphenyl)-N-(2-[18F]fluoroethyl-5-methoxybenzyl)acetamide, for PET imaging of peripheral benzodiazepine receptor in primate brain. *J. Med. Chem.* **47,** 2228–2235 (2004).

107. Sugama, S. & Kakinuma, Y. Noradrenaline as a key neurotransmitter in modulating microglial activation in stress response. *Neurochem. Int.* **143,** 1–8 (2021).

108. Mercan, D. & Heneka, M. T. Norepinephrine as a modulator of microglial dynamics. *Nat. Neurosci.* **22,** 1745–1746 (2019).

109. Stowell, R. D., Sipe, G. O., Dawes, R. P., *et al.* Noradrenergic signaling in the wakeful state inhibits microglial surveillance and synaptic plasticity in the mouse visual cortex. *Nat. Neurosci.* **22,** 1782–1792 (2019).

110. Liu, G., Froudarakis, E., Patel, J. M., *et al.* Target specific functions of EPL interneurons in olfactory circuits. *Nat. Commun.* **10,** 1–14 (2019).

111. Heneka, M. T., Nadrigny, F., Regen, T., *et al.* Locus ceruleus controls Alzheimer's disease pathology by modulating microglial functions through norepinephrine. *Proc. Natl. Acad. Sci. U. S. A.* **107,** 6058–6063 (2010).

112. Lin, C. P., Frigerio, I., Bol, J. G., *et al.* Microstructural integrity of the locus coeruleus and its tracts reflect noradrenergic degeneration in Alzheimer's disease and Parkinson's disease. *Transl. Neurodegener.* **13,** 1–17 (2024).

113. Kelly, S. C., He, B., Perez, S. E., *et al.* Locus coeruleus cellular and molecular pathology during the progression of Alzheimer's disease. *Acta Neuropathol. Commun.* **5,** 1–14 (2017).

114. Betts, M. J., Cardenas-Blanco, A., Kanowski, M., *et al.* Locus coeruleus MRI contrast is reduced in Alzheimer's disease dementia and correlates with CSF Aβ levels. *Alzheimer's Dement. Diagnosis, Assess. Dis. Monit.* **11,** 281–285 (2019).

115. Zarow, C., Lyness, S. A., Mortimer, J. A., *et al.* Neuronal loss is greater in the locus coeruleus than nucleus basalis and substantia nigra in Alzheimer and Parkinson diseases. *Arch. Neurol.* **60,** 337–341 (2003).

116. Theofilas, P., Ehrenberg, A. J., Dunlop, S., *et al.* Locus coeruleus volume and cell population changes during Alzheimer's disease progression: A stereological study in human postmortem brains with potential implication for early-stage biomarker discovery. *Alzheimer's Dement.* **13,** 236–246 (2017).

117. Kobro-Flatmoen, A., Hormann, T. M. & Gouras, G. Intracellular amyloid-β in the normal rat brain and human subjects and its relevance for Alzheimer's disease. *J. Alzheimer's Dis.* **95,** 719–733 (2023).

118. Matchett, B. J., Grinberg, L. T., Theofilas, P., *et al.* The mechanistic link between selective vulnerability of the locus coeruleus and neurodegeneration in Alzheimer's disease. *Acta Neuropathol.* **141,** 631–650 (2021).

119. Liu, Y., Yoo, M. J., Savonenko, A., *et al.* Amyloid pathology is associated with progressive monoaminergic neurodegeneration in a transgenic mouse model of Alzheimer's disease. *J. Neurosci.* **28,** 13805–13814 (2008).

120. Rorabaugh, J. M., Chalermpalanupap, T., Botz-Zapp, C. A., *et al.* Chemogenetic locus coeruleus activation restores reversal learning in a rat model of Alzheimer's disease. *Brain* **140,** 3023–3038 (2017).

121. Francis, B. M., Yang, J., Hajderi, E., *et al.* Reduced tissue levels of noradrenaline are associated with behavioral phenotypes of the TgCRND8 mouse model of Alzheimer's disease. *Neuropsychopharmacol.* **37,** 1934–1944 (2012).

122. Song, S., Jiang, L., Oyarzabal, E. A., *et al.* Loss of brain norepinephrine elicits neuroinflammation-mediated oxidative injury and selective caudo-rostral neurodegeneration. *Mol. Neurobiol.* **56,** 2653–2669 (2019).

123. Rey, N. L., Jardanhazi-Kurutz, D., Terwel, D., *et al.* Locus coeruleus degeneration exacerbates olfactory deficits in APP/PS1 transgenic mice. *Neurobiol. Aging* **33,** 426.e1–426.e11 (2012).

124. Ache, B. W. & Young, J. M. Olfaction: Diverse species, conserved principles. *Neuron* **48,** 417–430 (2005).

125. Francia, S. & Lodovichi, C. The role of the odorant receptors in the formation of the sensory map. *BMC Biol.* **19,** 1–18 (2021).

126. Sharma, A., Kumar, R., Aier, I., *et al.* Sense of smell: Structural, functional, mechanistic advancements and challenges in human olfactory research. *Curr. Neuropharmacol.* **17,** 891–911 (2018).

127. Nagayama, S., Homma, R. & Imamura, F. Neuronal organization of olfactory bulb circuits. *Front. Neural Circuits* **8,** 1–19 (2014).

128. Shipley, M. T., Halloran, F. J. & de la Torre, J. Surprisingly rich projection from locus coeruleus to the olfactory bulb in the rat. *Brain Res.* **329,** 294–299 (1985).

129. Nai, Q., Dong, H.-W., Linster, C., *et al.* Activation of $\alpha 1$ and $\alpha 2$ noradrenergic receptors exert opposing effects on excitability of main olfactory bulb granule cells. *IBRO* **23,** 1–7 (2010).

130. Manella, L. C., Petersen, N. & Linster, C. Stimulation of the locus ceruleus modulates signal-to-noise ratio in the olfactory bulb. *J. Neurosci.* **37,** 11605–11615 (2017).

131. Escanilla, O., Alperin, S., Youssef, A., *et al.* Noradrenergic, but not cholinergic modulation of olfactory bulb during processing of near threshold concentration stimuli. *Behav. Neurosci.* **126,** 720–728 (2012).

132. Doucette, W., Milder, J. & Restrepo, D. Adrenergic modulation of olfactory bulb circuitry affects odor discrimination. *Learn. Mem.* **14,** 539–547 (2007).

133. Devore, S. & Linster, C. Noradrenergic and cholinergic modulation of olfactory bulb sensory processing. *Front. Behav. Neurosci.* **6,** 1–12 (2012).

134. Linster, C., Midroit, M., Forest, J., *et al.* Noradrenergic activity in the olfactory bulb is a key element for the stability of olfactory memory. *J. Neurosci.* **40,** 9260–9271 (2020).

135. Záborszky, L., Carlsen, J., Brashear, H. R., *et al.* Cholinergic and GABAergic afferents to the olfactory bulb in the rat with special emphasis on the projection neurons in the nucleus of the horizontal limb of the diagonal band. *J. Comp. Neurol.* **243,** 488–509 (1986).

136. Macrides, F., Davis, B. J., Youngs, W. M., *et al.* Cholinergic and catecholaminergic afferents to the olfactory bulb in the hamster: A neuroanatomical, biochemical, and histochemical investigation. *J. Comp. Neurol.* **203,** 495–514 (1981).

137. Hamamoto, M., Kiyokage, E., Sohn, J., *et al.* Structural basis for cholinergic regulation of neural circuits in the mouse olfactory bulb. *J. Comp. Neurol.* **525,** 574–591 (2017).

138. De Saint Jan, D. Target-1 specific control of olfactory bulb periglomerular cells by GABAergic and cholinergic basal forebrain inputs. *Elife* **11,** 1–27 (2022).

139. D'Souza, R. D. & Vijayaraghavan, S. Paying attention to smell: Cholinergic signaling in the olfactory bulb. *Front. Synaptic Neurosci.* **6,** 1–11 (2014).

140. Ross, J. M., Bendahmane, M. & Fletcher, M. L. Olfactory bulb muscarinic acetylcholine type 1 receptors are required for acquisition of olfactory fear learning. *Front. Behav. Neurosci.* **13,** 1–9 (2019).

141. Höglinger, G. U., Alvarez-Fischer, D., Arias-Carrión, O., *et al.* A new dopaminergic nigro-olfactory projection. *Acta Neuropathol.* **130,** 333–348 (2015).

142. Zhang, W., Sun, C., Shao, Y., *et al.* Partial depletion of dopaminergic neurons in the substantia nigra impairs olfaction and alters neural activity in the olfactory bulb. *Sci. Rep.* **9,** 1–13 (2019).

143. Fomin-Thunemann, N. & Garaschuk, O. Role of serotonin in modulating the development and function of adult-born neurons in the olfactory bulb. *Neural Regen. Res.* **17,** 1253–1254 (2022).

144. Fletcher, M. L. & Chen, W. R. Neural correlates of olfactory learning: Critical role of centrifugal neuromodulation. *Learn. Mem.* **17,** 561–570 (2010).

145. Suzuki, Y., Kiyokage, E., Sohn, J., *et al.* Structural basis for serotonergic regulation of neural circuits in the mouse olfactory bulb. *J. Comp. Neurol.* **523,** 262–280 (2015).

146. Brill, J., Shao, Z., Puche, A. C., *et al.* Serotonin increases synaptic activity in olfactory bulb glomeruli. *J. Neurophysiol.* **115,** 1208–1219 (2016).

147. Doty, R. L. Olfaction in Parkinson's disease and related disorders. *Neurobiol. Dis.* **46,** 527–552 (2012).

148. Marchetti, E., Dumuis, A., Bockaert, J., *et al.* Differential modulation of the 5-HT4 receptor agonists and antagonist on rat learning and memory. *Neuropharmacol.* **39,** 2017–2027 (2000).

149. Letty, S., Child, R., Dumuis, A., *et al.* 5-HT4 receptors improve social olfactory memory in the rat. *Neuropharmacol.* **36,** 681–687 (1997).

150. Morilzumi, T., Tsukatani, T, Sakashita, H, *et al.* Olfactory disturbance induced by deafferentiation of serotonergic fibers in the olfactory bulb. *Neuroscience* **61,** 733–738 (1994).

151. Slabik, D. & Garaschuk, O. Olfactory dysfunction as a common biomarker for neurodegenerative and neuropsychiatric disorders. *Neural Regen. Res.* **18,** 1029–1030 (2023).

152. Bekdash, R. A. The cholinergic system, the adrenergic system and the neuropathology of alzheimer's disease. *Int. J. Mol. Sci.* **22,** 1–18 (2021).

153. Doty, R. L. Olfactory dysfunction in neurodegenerative diseases: is there a common pathological substrate? *Lancet Neurol.* **16,** 478–488 (2017).

154. Doty, R. L., Shaman, P., Applebaum, S. L., *et al.* Smell identification ability: Changes with age. *Science* **226,** 1441–1443 (1984).

155. Hummel, T., Kobal, G., Gudziol, H., *et al.* Normative data for the "Sniffin' Sticks" including tests of odor identification, odor discrimination, and olfactory thresholds: An upgrade based on a group of more than 3,000 subjects. *Eur. Arch. Oto-Rhino-Laryngology* **264,** 237–243 (2007).

156. Devanand, D., Tabert, M., Cuasay, K, *et al.* Olfactory identification deficits and MCI in a multi-ethnic elderly community sample. *Neurobiol. Aging* **31,** 1593–1600 (2010).

157. Conti, M. Z., Vicini-Chilovi, B., Riva, M., *et al.* Odor identification deficit predicts clinical conversion from mild cognitive impairment to dementia due to alzheimer's disease. *Arch. Clin. Neuropsychol.* **28,** 391–399 (2013).

158. Murphy, C. Olfactory and other sensory impairments in Alzheimer disease. *Nat. Rev. Neurol.* **15,** 11–24 (2019).

159. Son, G., Jahanshahi, A., Yoo, S. J., *et al.* Olfactory neuropathology in Alzheimer's disease: a sign of ongoing neurodegeneration. *BMB Rep.* **54,** 295–304 (2021).

160. Murray, H. C., Dieriks, B. V., Swanson, M. E., *et al.* The unfolded protein response is activated in the olfactory system in Alzheimer's disease. *Acta Neuropathol. Commun.* **8,** 1–16 (2020).

161. Borenstein Graves, A., Bowen, J. D., Rajaram, L., *et al.* Impaired olfaction as a marker for cognitive decline: Interaction with apolipoprotein Eϵ4. *Neurology* **53,** 1480–1487 (1999).

162. Josefsson, M., Larsson, M., Nordin, S., *et al.* APOE-e4 effects on longitudinal decline in olfactory and non-olfactory cognitive abilities in middle-aged and old adults. *Sci. Rep.* **7,** 1–9 (2017).

163. Palmquist, E., Larsson, M., Olofsson, J. K., *et al.* A prospective study on risk factors for olfactory dysfunction in aging. *Journals Gerontol.: Med. Sci.* **75,** 603–610 (2020).

164. Son, G., Steinbusch, H. W., López-Iglesias, C., *et al.* Severe histomorphological alterations in post-mortem olfactory glomeruli in Alzheimer's disease. *Brain Pathol.* **32,** 1–16 (2022).

165. Sakakibara, Y., Hirota, Y., Ibaraki, K., *et al.* Widespread reduced density of noradrenergic locus coeruleus axons in the app knock-in mouse model of amyloid-β amyloidosis. *J. Alzheimer's Dis.* **82,** 1513–1530 (2021).

166. Horie, S., Kiyokage, E., Hayashi, S., *et al.* Structural basis for noradrenergic regulation of neural circuits in the mouse olfactory bulb. *J. Comp. Neurol.* **529,** 2189–2208 (2020).

167. Sobue, A., Komine, O., Hara, Y., *et al.* Microglial gene signature reveals loss of homeostatic microglia associated with neurodegeneration of Alzheimer's disease. *Acta Neuropathol. Commun.* **9,** 1–17 (2021).

168. Monasor, L. S., Müller, S. A., Colombo, A. V., *et al.* Fibrillar Aβ triggers microglial proteome alterations and dysfunction in alzheimer mouse models. *Elife* **9,** 1–33 (2020).

169. Cao, S., Fisher, D. W., Rodriguez, G., *et al.* Comparisons of neuroinflammation, microglial activation, and degeneration of the locus coeruleus-norepinephrine system in APP/PS1 and aging mice. *J. Neuroinflammation* **18,** 1–16 (2021).

170. Mitrano, D. A., Houle, S. E., Pearce, P., *et al.* Olfactory dysfunction in the 3xTg-AD model of Alzheimer's disease. *IBRO Neurosci. reports* **10,** 51–61 (2021).

171. Dan, X., Yang, B., McDevitt, R. A., *et al.* Loss of smelling is an early marker of aging and is associated with inflammation and DNA damage in C57BL/6J mice. *Aging Cell* **22,** 1–13 (2023).

172. Masuda, A., Kobayashi, Y., Kogo, N., *et al.* Cognitive deficits in single App knock-in mouse models. *Neurobiol. Learn. Mem.* **135,** 73–82 (2016).

173. Tzeng, W.-Y., Figarella, K. & Garaschuk, O. Olfactory impairment in men and mice related to aging and amyloid-induced pathology. *European Journal of Physiology* **473,** 805–821 (2021).

174. Oliveira-Pinto, A. V., Santos, R. M., Coutinho, R. A., *et al.* Sexual dimorphism in the human olfactory bulb: Females have more neurons and glial cells than males. *PLOS* **9,** 1–9 (2021).

175. Alexa F. Iannitelli, Michael A. Kelberman1, Daniel J. Lustberg1, Anu Korukonda1, Katharine E. McCann1, Bernard Mulvey2, Arielle Segal1, L. Cameron Liles1, Steven A. Sloan1, Joseph D. Dougherty2,3, D. W. The Neurotoxin DSP-4 Dysregulates the Locus Coeruleus-Norepinephrine System and Recapitulates Molecular and Behavioral Aspects of Prodromal Neurodegenerative Disease Alexa (2022).

176. Yin, X., Jones, N., Yang, J., *et al.* Delayed motor learning in a 16p11.2 deletion mouse model of autism is rescued by locus coeruleus activation. *Nat. Neurosci.* **24,** 646–657 (2021).

177. Kushikata, T., Hirota, K., Kotani, N., *et al.* Isoflurane increases norepinephrine release in the rat preoptic area and the posterior hypothalamus in vivo and in vitro: Relevance to thermoregulation during anesthesia. *Neuroscience* **131,** 79–86 (2005).

178. Liebe, T., Li, M., Colic, L., *et al.* Ketamine influences the locus coeruleus norepinephrine network, with a dependency on norepinephrine transporter genotype – a placebo controlled fMRI study. *NeuroImage Clin.* **20,** 715–723 (2018).

179. Iro, C. M., Hamati, R., El Mansari, M., *et al.* Repeated but not single administration of ketamine prolongs increases of the firing activity of norepinephrine and dopamine neurons. *Int. J. Neuropsychopharmacol.* **24,** 570–579 (2021).

180. Hara, K., Yanagihara, N., Minami, K., *et al.* Ketamine interacts with the noradrenaline transporter at a site partly overlapping the desipramine binding site. *Naunyn. Schmiedebergs. Arch. Pharmacol.* **358,** 328–333 (1998).

181. Zhao, Y. & Sun, L. Antidepressants modulate the in vitro inhibitory effects of propofol and ketamine on norepinephrine and serotonin transporter function. *J. Clin. Neurosci.* **15,** 1264–1269 (2008).

182. Galmozzi, A., Dominguez, E., Cravatt, B. F., *et al.* Noradrenergic neuromodulation in the olfactory bulb modulates odor habituation and spontaneous discrimination. *Methods Enzym.* **538,** 151–169 (2014).

183. Loopuijt, L. D. & Sebens, J. B. Loss of dopamine receptors in the olfactory bulb of patients with Alzheimer's disease. *Brain Res.* **529,** 239–244 (1990).

184. Simpson, J. Olfactory tubercle choline acetyltransferase activity in Alzheimer-type dementia, Down's syndrome and Huntington's disease. *J. Neurol. Neurosurg. Psychiatry* (1984).

185. Villar, P. S., Hu, R., Teitz, B., *et al.* Cholinergic modulation of distinct inhibitory domains in granule cells of the olfactory bulb. *bioRxiv* (2021).

186. Brunert, D., Tsuno, Y., Rothermel, M., *et al.* Cell-type-specific modulation of sensory responses in olfactory bulb circuits by serotonergic projections from the raphe nuclei. *J. Neurosci.* **36,** 6820–6835 (2016).

187. Petzold, G. C., Hagiwara, A. & Murthy, V. N. Serotonergic modulation of odor input to the mammalian olfactory bulb. *Nat. Neurosci.* **12,** 784–791 (2009).

188. Teng, T., Gaillard, A., Muzerelle, A., *et al.* Ephrina5 signaling is required for the distinctive targeting of raphe serotonin neurons in the forebrain. *eNeuro* **4,** 1–18 (2017).

189. Gamper, N. *Ion Channels: Methods and Protocols* ISBN: 9781627033503 (Springer, 2013).

190. Chiodo, L. A., Acheson, A. L., Zigmond, M. J., *et al.* Subtotal destruction of central noradrenergic projections increases the firing rate of locus coeruleus cells. *Brain Res.* **264,** 123–126 (1983).

191. Lerdkrai, C., Asavapanumas, N., Brawek, B., *et al.* Intracellular Ca^{2+} stores control in vivo neuronal hyperactivity in a mouse model of Alzheimer's disease. *PNAS* **115,** E1279–E1288 (2018).

192. Granados-Fuentes, D., Norris, A. J., Carrasquillo, Y., *et al.* I(A) channels encoded by Kv1.4 and Kv4.2 regulate neuronal firing in the suprachiasmatic nucleus and circadian rhythms in locomotor activity. *J. Neurosci.* **32,** 10045–10052 (2012).

193. Deng, X. H., Liu, X. Y., Wei, Y. H., *et al.* ErbB4 deficiency exacerbates olfactory dysfunction in an early-stage Alzheimer's disease mouse model. *Acta Pharmacol. Sin.* **0,** 1–16 (2024).

194. Li, S., Li, W., Wu, X., *et al.* Olfactory deficit is associated with mitral cell dysfunction in the olfactory bulb of P301S tau transgenic mice. *Brain Res. Bull.* **148,** 34–45 (2019).

195. Panzanelli, P., Perazzini, A. Z., Fritschy, J. M., *et al.* Heterogeneity of γ-aminobutyric acid type A receptors in mitral and tufted cells of the rat main olfactory bulb. *J. Comp. Neurol.* **484,** 121–131 (2005).

196. Angelo, K. & Margrie, T. W. Population diversity and function of hyperpolarization-activated current in olfactory bulb mitral cells. *Sci. Rep.* **1,** 1–11 (2011).

197. Angelo, K., Rancz, E. A., Pimentel, D., *et al.* A biophysical signature of network affiliation and sensory processing in mitral cells. **488,** 375–378 (2013).

198. Orona, E., Rainer, E. C. & Scott, J. W. Dendritic and axonal organization of mitral and tufted cells in the rat olfactory bulb. *J. Comp. Neurol.* **226,** 346–356 (1984).

199. Gorazd, B. S., Concepción, L., Tomás, L. F., *et al.* Axonopathy and transport deficits early in the pathogenesis of Alzheimer's disease. *Science* **307,** 1282–1288 (2005).

200. Wang, J. & Zhigang, H. NAD and axon degeneration. *Cell Adhes. Migr.* **3,** 77–87 (2009).

201. Anholt, R. R. H., Murphy, K., Mack, G., *et al.* Peripheral-type benzodiazepine receptors in the central receptors system: Localization to in the olfactory nerves. *Neuroscience* **4,** 593–603 (1984).

202. Sacher, C., Blume, T., Beyer, L., *et al.* Longitudinal PET monitoring of amyloidosis and microglial activation in a second-generation amyloid-β mouse model. *J. Nucl. Med.* **60,** 1787–1793 (2019).

203. Biechele, G., Franzmeier, N., Blume, T., *et al.* Glial activation is moderated by sex in response to amyloidosis but not to tau pathology in mouse models of neurodegenerative diseases. *J. Neuroinflammation* **17,** 1–10 (2020).

204. Gao, C., Jiang, J., Tan, Y., *et al.* Microglia in neurodegenerative diseases: mechanism and potential therapeutic targets. *Sig. Transduct. Target. Ther.* **8,** 1–37 (2023).

205. Lull, M. E. & Block, M. L. Microglial activation and chronic neurodegeneration. *Neurotherapeutics* **7,** 354–365 (2010).

206. Hayashi, Y., Otsuji, J., Oshima, E., *et al.* Microglia cause structural remodeling of noradrenergic axon in the trigeminal spinal subnucleus caudalis after infraorbital nerve injury in rats. *Brain, Behav. Immun. - Heal.* **30,** 1–8 (2023).

207. Ma, X., Li, X., Wang, W., *et al.* Phosphatidylserine, inflammation, and central nervous system diseases. *Front. Aging Neurosci.* **14,** 1–18 (2022).

208. Naeini, M. B., Bianconi, V., Pirro, M., *et al.* The role of phosphatidylserine recognition receptors in multiple biological functions. *Cell. Mol. Biol. Lett.* **25** (2020).

209. Aziz, M., Jacob, A., Matsuda, A., *et al.* Review: Milk fat globule-EGF factor 8 expression, function and plausible signal transduction in resolving inflammation. *Apoptosis* **16,** 1077–1086 (2011).

210. Hanayama, R., Tanaka, M., Miwa, K., *et al.* Identification of a factor that links apoptotic cells to phagocytes. *Nature* **417,** 182–187 (2002).

211. Davalos, D., Grutzendler, J., Yang, G., *et al.* ATP mediates rapid microglial response to local brain injury in vivo. *Nat. Neurosci.* **8,** 752–758 (2005).

212. Szepesi, Z., Manouchehrian, O., Bachiller, S., *et al.* Bidirectional microglia–neuron communication in health and disease. *Front. Cell. Neurosci.* **12,** 1–26 (2018).

213. Kong, Y., Ruan, L., Qian, L., *et al.* Norepinephrine promotes microglia to uptake and degrade amyloid β peptide through upregulation of mouse formyl peptide receptor 2 and induction of insulin-degrading enzyme. *J. Neurosci.* **30,** 11848–11857 (2010).

214. Liu, Y. U., Ying, Y., Li, Y., *et al.* Neuronal network activity controls microglial process surveillance in awake mice via norepinephrine signaling. *Nat. Neurosci.* **22,** 1771–1781 (2019).

215. Janitzky, K. Impaired phasic discharge of locus coeruleus neurons based on persistent high tonic discharge — A new hypothesis with potential implications for neurodegenerative diseases. *Front. Neurol.* **11,** 1–15 (2020).

216. Wang, H.-Y., Lee, D. H., D'Andrea, M. R., *et al.* β-amyloid1–42 binds to α7 nicotinic acetylcholine receptor with high affinity. *J. Biol. Chem.* **275,** 5626–5632 (2000).

217. Zhang, J., Zhu, Y., Zhan, G., *et al.* Extended wakefulness: Compromised metabolics in and degeneration of locus ceruleus neurons. *J. Neurosci.* **34,** 4418–4431 (2014).

218. Zamore, Z. & Veasey, S. C. Neural consequences of chronic sleep disruption. *Trends Neurosci.* **45,** 678–691 (2022).

219. Chou, M. C., Lee, H. C., Liu, Y. C., *et al.* Long-term high-fat diet consumption depletes glial cells and tyrosine hydroxylase–containing neurons in the brain of middle-aged rats. *Cells* **11,** 1–16 (2022).

220. Ross, S. B. & Stenfors, C. DSP4, a selective neurotoxin for the locus coeruleus noradrenergic system. A review of its mode of action. *Neurotox. Res.* **27,** 15–30 (2015).

221. Kang, S. S., Liu, X., Ahn, E. H., *et al.* Norepinephrine metabolite DOPEGAL activates AEP and pathological Tau aggregation in locus coeruleus. *J. Clin. Invest.* **130,** 422–437 (2020).

222. Kang, S. S., Meng, L., Zhang, X., *et al.* Tau modification by the norepinephrine metabolite DOPEGAL stimulates its pathology and propagation. *Nat. Struct. Mol. Biol.* **29,** 292–305 (2022).

223. Dahl, M. J., Mather, M., Werkle-Bergner, M., *et al.* Locus coeruleus integrity is related to tau burden and memory loss in autosomal-dominant Alzheimer's disease. *Neurobiol. Aging* **112,** 39–54 (2022).

224. Van Egroo, M., Riphagen, J. M., Ashton, N. J., *et al.* Ultra-high field imaging, plasma markers and autopsy data uncover a specific rostral locus coeruleus vulnerability to hyperphosphorylated Tau. *Mol. Psychiatry* **28,** 2412–2422 (2023).

225. Chan-Palay, V. & Asan, E. Quantitation of catecholamine neurons in the locus coeruleus in human brains of normal young and older adults and in depression. *J. Comp. Neurol.* **287,** 357–372 (1989).

226. German, D. C., Manaye, K. F., White, C. L., *et al.* Disease-specific patterns of locus coeruleus cell loss. *Ann. Neurol.* **32,** 667–676 (1992).

227. Wu, N., Rao, X., Gao, Y., *et al.* Amyloid-β deposition and olfactory dysfunction in an alzheimer's disease model. *J. Alzheimer's Dis.* **37,** 699–712 (2013).

228. Ziegler-Waldkirch, S., Friesen, M., Loreth, D., *et al.* Seed-induced Aβ deposition alters neuronal function and impairs olfaction in a mouse model of Alzheimer's disease. *Mol. Psychiatry* **27,** 4274–4284 (2022).

229. Yoo, S. J., Lee, J. H., Kim, S. Y., *et al.* Differential spatial expression of peripheral olfactory neuron-derived bace1 induces olfactory impairment by region-specific accumulation of β-amyloid oligomer. *Cell Death Dis.* **8,** e2977–12 (2017).

230. Ross, J. A., Reyes, B. A., Thomas, S. A., *et al.* Localization of endogenous amyloid-β to the coeruleo-cortical pathway: consequences of noradrenergic depletion. *Brain Struct. Funct.* **223,** 267–284 (2018).

231. Fairley, L. H., Lai, K. O., Wong, J. H., *et al.* Mitochondrial control of microglial phagocytosis by the translocator protein and hexokinase 2 in Alzheimer's disease. *PNAS* **120,** 1–12 (2023).

232. Zhang, H., Wang, H., Gao, F., *et al.* TSPO deficiency accelerates amyloid pathology and neuroinflammation by impairing microglial phagocytosis. *Neurobiol. Aging* **106,** 292–303 (2021).

233. Qiao, L., Fisher, E., McMurray, L., *et al.* Radiosynthesis of (R,S)-[18F]GE387: A potential PET radiotracer for imaging translocator protein 18 kDa (TSPO) with low binding sensitivity to the human gene polymorphism rs6971. *ChemMedChem* **14,** 982–993 (2019).

234. Cumming, P., Burgher, B., Patkar, O., *et al.* Sifting through the surfeit of neuroinflammation tracers. *J. Cereb. Blood Flow Metab.* **38,** 204–224 (2018).

235. Rossano, S. M., Johnson, A. S., Smith, A., *et al.* Microglia measured by TSPO PET are associated with Alzheimer's disease pathology and mediate key steps in a disease progression model. *Alzheimer's Dement.* **20,** 2397–2407 (2024).

236. Dani, M., Wood, M., Mizoguchi, R., *et al.* Microglial activation correlates in vivo with both tau and amyloid in Alzheimer's disease. *Brain* **141,** 2740–2754 (2018).

237. Parbo, P., Ismail, R., Sommerauer, M., *et al.* Does inflammation precede Tau aggregation in early Alzheimer's disease? A PET study. *Neurobiol. Dis.* **117,** 211–216 (2018).

238. Knezevic, D., Verhoeff, N. P. L., Hafizi, S., *et al.* Imaging microglial activation and amyloid burden in amnestic mild cognitive impairment. *J. Cereb. Blood Flow Metab.* **38,** 1885–1895 (2018).

239. Toppala, S., Ekblad, L. L., Tuisku, J., *et al.* Association of early β-amyloid accumulation and neuroinflammation measured with [11C]PBR28 in elderly individuals without dementia. *Neurology* **96,** E1608–E1619 (2021).

240. Gouilly, D., Saint-Aubert, L., Ribeiro, M. J., *et al.* Neuroinflammation PET imaging of the translocator protein (TSPO) in Alzheimer's disease: An update. *Eur. J. Neurosci.* **55,** 1322–1343 (2022).

241. Klein, J., Yan, X., Johnson, A., *et al.* Olfactory impairment is related to Tau pathology and neuroinflammation in Alzheimer's disease. *J. Alzheimer's Dis.* **80,** 1051–1065 (2021).

242. Owen, D. R., Narayan, N., Wells, L., *et al.* Pro-inflammatory activation of primary microglia and macrophages increases 18 kDa translocator protein expression in rodents but not humans. *J. Cereb. Blood Flow Metab.* **37,** 2679–2690 (2017).

243. Nutma, E., Fancy, N., Weinert, M., *et al.* Translocator protein is a marker of activated microglia in rodent models but not human neurodegenerative diseases. *Nat. Commun.* **14,** 1–25 (2023).

244. Woodward, M. R., Amrutkar, C. V., Shah, H. C., *et al.* Validation of olfactory deficit as a biomarker of Alzheimer disease. *Neurol. Clin. Pract.* **7,** 5–14 (2017).

245. Tu, L., Lv, X., Fan, Z., *et al.* Association of odor identification ability with amyloid-β and tau burden: A systematic review and meta-analysis. *Front. Neurosci.* **14,** 1–11 (2020).

246. Igeta, Y., Hemmi, I., Yuyama, K., *et al.* Odor identification score as an alternative method for early identification of amyloidogenesis in Alzheimer's disease. *Sci. Rep.* **14,** 1–14 (2024).

247. Gradinaru, V., Zhang, F., Ramakrishnan, C., *et al.* Molecular and cellular approaches for diversifying and extending optogenetics. *Cell* **141,** 154–165 (2010).

248. Lehrman, E., Wilton, D., Litvina, E., *et al.* CD47 protects synapses from excess microglia-mediated pruning during development. *Neuron* **100,** 120–134 (2018).

249. Brendel, M., Probst, F., Jaworska, A., *et al.* Glial activation and glucose metabolism in a transgenic amyloid mouse model: A triple-tracer PET study. *Journal of Nuclear Medicine* **57,** 954–960 (2016).

250. Deussing, M., Blume, T., Vomacka, L., *et al.* Coupling between physiological TSPO expression in brain and myocardium allows stabilization of late-phase cerebral [18F]GE180 PET quantification. *Neuroimage* **165,** 83–91 (2018).

251. Ma, Y., Hof, P. R., Grant, S. C., *et al.* A three-dimensional digital atlas database of the adult C57BL/6J mouse brain by magnetic resonance microscopy. *Neuroscience* **135,** 1203–1215 (2005).

252. Finze, A., Biechele, G., Rauchmann, B. S., *et al.* Individual regional associations between Aβ-, Tau- and neurodegeneration (ATN) with microglial activation in patients with primary and secondary tauopathies. *Mol. Psychiatry* **28,** 4438–4450 (2023).

253. Rauchmann, B. S., Brendel, M., Franzmeier, N., *et al.* Microglial activation and connectivity in Alzheimer disease and aging. *Ann. Neurol.* **92,** 768–781 (2022).

Contributions

Several people contributed valuable knowledge to the present study and performed parts of experiments. Theresa Niedermeier performed olfactory bulb window surgery and noradrenaline 2-photon in vivo measurements (Fig. 14b-e,h-j). Paul Feyen performed olfactory bulb window surgery, noradrenaline 2-photon in vivo measurements and analysed olfactory sensitivity tests (Fig. 13d,e and 14b,e). Felix Strübing performed olfactory bulb microglia sequencing and subsequent data analysis (Fig. 20). Johanna Gentz performed immunofluorescent staining and confocal imaging (Fig. 19). Yannik Tillmann performed microglia isolation and phagocytosis assay (Fig. 21). Katharina Ochs performed microglia isolation for sequencing (Fig. 20). Matthias Brendel, Karin Wind-Mark and Gloria Biechele performed small animal PET study and analysis (Fig. 25). Boris Rauchmann, Selim Guersel, Carolin Kurz and Meike Schweiger performed human odor identification tests (Fig. 31c). Robert Perneczky performed human PET study and analysis (Fig. 20a,b). Lars Paeger performed virus injections (Fig. 15a, 16a, 22c and 29a), project planning and supervision of the project.

Publications

Carolin Meyer, Theresa Niedermeier, Paul Feyen, et al., Noradrenergic axon loss drives olfactory dysfunction in Alzheimer's disease, Research Sqaure preprint (02 October 2024). https://doi.org/10.21203/rs.3.rs-4887136/v1
Manuscript under revision at Nature Communications

Luna Slemann*, Johannes Gnörich*, Selina Hummel*, Laura M. Bartos*, **Carolin Klaus**, et al., Neuronal and oligodendroglial but not astroglial tau translates to in vivo tau-PET signals in primary tauopathies, Acta Neuropathology 148 (2024)
https://doi.org/10.1007/s00401-024-02834-7
* contributed equally as first authors

Artem Zatcepin, [...], **Carolin Meyer**, et al., Regional desynchronization of microglial activity is associated with cognitive decline in Alzheimer's disease. Molecular Neurodegeneration 19, 64 (2024)
https://molecularneurodegeneration.biomedcentral.com/articles/
10.1186/s13024-024-00752-6

Johannes Gnörich, Mara Koehler, Karin Wind-Mark, **Carolin Klaus**, et al., Towards multicenter Aβ-amyloid PET imaging in mouse models: A triple scanner head-to-head comparison. NeuroImage 297, 15 (2024).
https://www.sciencedirect.com/science/article/pii/S1053811924002453

Anna Ballweg*, **Carolin Klaus***, Letizia Vogler*, et al., [18F]F-DED PET Imaging of Reactive Astrogliosis in Neurodegenerative Diseases: Preclinical Proof of Concept and First-in-human Data. Journal of Neuroinflammation 20, 1 (2023).
https://jneuroinflammation.biomedcentral.com/articles/10.1186/s12974-023-02749-2,
* contributed equally as first authors

Sonja Blumenstock, Fanfan Sun, **Carolin Klaus**, Petar Marinković, Carmelo Sgobio, Lars Paeger, Sabine Liebscher and Jochen Herms, Cortical Circuit Dysfunction in a Mouse Model of Alpha-synucleinopathy in vivo. Brain Communications 3, 4 (2021). https://doi.org/10.1093/braincomms/fcab273

Presentations and Poster

Talk to the public layman at "Tag der nervenstarken Forschung", organized by SyNergy. June 2024, Ludwig-Maximilians-University Munich, Germany. Das riecht nach Demenz

Oral presentation at AD/PD conference 2024 in Lisbon, Portugal. March 2024. Early locus coeruleus degeneration drives olfactory dysfunction in Alzheimer's disease

Poster presentation at SFN Neuroscience conference 2023 in Washington DC. Walter E. Convention Center, USA. November 2023, SyNergy travel grant for female scientists (1.000 €)

Acknowledgements

Es war einmal eine Expedition in die Tiefen der Wissenschaft, voller Herausforderungen und Entdeckungen. Wie jede große Reise lebte auch dieses Abenteuer von den großartigen Begleitern, deren Wissen und Rückhalt jede Etappe bereicherte.

Der Kapitän des Schiffs – Mein erster Dank gilt Jochen, meinem Chef und Kapitän dieser aufregenden Expedition. Danke, dass Du mir die Möglichkeit gegeben hast, meine Reise in Deinem Labor zu beginnen, und mir den Freiraum und die Unterstützung geboten hast, um meine eigene Route zu kartieren.

Der Navigator – Lars, du warst der unermüdliche Navigator dieses Abenteuers. Mit deinem Enthusiasmus hast Du stets neue Wege aufgezeigt, mich mit kreativen Ideen inspiriert und das Tempo hochgehalten, wenn ich mal an einer Weggabelung innegehalten habe. Während Du ungeduldig auf die Ergebnisse gewartet hast, hast Du es mir trotzdem ermöglicht, ruhig und fokussiert zu bleiben.

Der Investor – Prof. Dr. Martin Biel, mein Doktorvater. Vielen Dank, dass Sie Ihr Vertrauen in mich investiert haben und mir die Möglichkeit gaben, über die Fakultät für Chemie und Pharmazie diese Reise antreten zu können.

Die Crew – Theresa, Paul, Felix, Johanna, Jannik, Katharina und Jessica. Ihr wart die verlässliche Crew, die mit ihren Fertigkeiten und Ideen dafür gesorgt hat, dass unser gemeinsames Projekt zu einer großartigen Geschichte geworden ist.

Die Forscher des fremden Landes – Matthias, Boris und das Klinikteam. Ich danke Euch vielmals für Eure wertvollen Messungen und Daten. Ihr habt die Schätze gehoben, die ich niemals allein hätte bergen können.

Die Hüter der Schleuse – Ekrem und das Tierpfleger-Team. Ihr habt für die Versorgung unserer tierischen Begleiter gesorgt, sodass ich mich voll und ganz auf meine Expedition konzentrieren konnte.

Der innere Zirkel – Svenja, Johanna, Katharina und Katerina. Ihr habt das Labor zu einem Ort gemacht, an dem Arbeit sich oft wie ein Abenteuer mit Freunden anfühlte. Danke für die aufmunternden Worte, Tipps und all die kleinen Momente, die mir den Tag

erhellt haben.

Der Technomat – Benno, Du warst der Meister der Technik, der bei Kabelbrand immer sofort zur Stelle war.

Die AG – Ein großes Dankeschön an alle Mitglieder der AG Herms. Eure Gemeinschaft hat eine warme, positive Atmosphäre geschaffen, die mir stets Kraft gegeben hat.

Der Gefährte – Frank, Du warst der Fels in der Brandung. Du warst immer da, um meine Rechnungen zu prüfen, mir bei Latex zu helfen und mir zuzuhören, egal ob es um die Höhen oder die Tiefen meiner Arbeit ging. Danke, dass Du mich ertragen hast, wenn ich frustriert war, und dafür, dass ich abends bei Dir abschalten konnte.

Die schützenden Geister – Meiner Familie gebührt ein besonderer Dank. Ihr habt mich stets unterstützt und ermutigt, egal, wohin mich mein Weg führte. In allen Lebenslagen wart ihr da, habt mich aufgefangen und mich über Wasser gehalten.

Hier endet diese Etappe meiner Reise, doch das Abenteuer, das ich erleben durfte, bleibt in Erinnerung. Jeder von Euch hat mir geholfen, den Zielhafen zu erreichen, dafür danke ich Euch von ganzem Herzen.